

POLITECNICO DI TORINO

Corso di Laurea in Ingegneria Meccanica

Tesi di Laurea Magistrale

Nonlinear Vibration of Bladed Discs



Relatore

prof. Stefano ZUCCA

Dr. Loïc SALLES

Candidato

Stefano SCALVINI

matricola: 263403

APRILE 2021

Abstract

Over the years, finite element software has taken an increasingly important place in the engineering field and the aerospace sector is no exception: the verification of structural aspects with this software is now common practice. This is the background to the European research project EXPERTISE, which aims to develop tools and methodologies for the dynamic analysis of large-scale turbomachinery models, thus pioneering the virtual testing of the entire machine. This thesis project is aimed at demonstrating the potential of how finite element software can help in the design and verification of bladed discs, and how to estimate the level of vibrations due to forced response near resonance. The correct prediction of the dynamic behaviour of a bladed disk is of uttermost importance since it affects the performance of the entire aircraft engine, its reliability and maintenance as vibrations are the major cause for high cycle fatigue failure. A strongly nonlinear dynamic response can be observed during engine operation given the particular complex design of turbomachinery, thus representing a big challenge for the virtual analysis. When verifying a tuned bladed disc, the most used approach is to analyse only a single sector exploiting the cyclic symmetry hypothesis, thus reducing the computational cost. During this work modal analysis of tuned system has been carried out in the open-source software CalculiX to determine the prestressed modes and build the SAFE diagram, a widely used tool which helps to find resonances, thus indicating to the designer which of them should be checked. The results obtained in CalculiX have been compared to the one in the Rolls-Royce in-house software SC03 and ANSYS for validation. Then a reduced model based on free modes and FRF matrix has been built by extracting the mode shapes with CalculiX. The nonlinear forced response is computed using harmonic balance method. Today's computational power is not nearly enough to estimate the response of the whole model thus only a handful of degrees of freedom are retained in the reduced order model. The nonlinear forced response curve has been computed using the Imperial College in-house code FORSE. The proposed approach has been applied to a bladed-disk testcase provided by SAFRAN in the framework of the EXPERTISE project. The demonstrator consists of a disc with 24 shrouded blades. The nodes retained in the reduced order model nodes are selected at the interface between two blades, where the cause of the major nonlinearities is the friction due to contact. The ROM has been validated first comparing the mode shapes with the MAC then checking the estimated response. Finally, a sensitivity analysis of the characteristics most affecting the nonlinear behaviour, such as contact parameters, shroud geometry or the type of elements used, has been carried out. The obtained results validate the proposed approach and interesting nonlinear behaviours of the bladed-disc has been observed and deeply discussed.

Acknowledgements

First of all I want to thank Dr. Loïc Salles for taking me into his research group and giving me access to the VUTC facilities. I am also extremely grateful for his help and guide throughout the whole project.

Then I would like to thank Prof. Stefano Zucca, as my supervisor from Politecnico di Torino: he not only has always been supportive but made all of this possible.

Finally, I also want to thank Dr. Pourkiaee for his invaluable help in using Ansys in order to get result from NOVA, the software he is developing for PoliTO.

Last but not least, I would like to thank my entire family and everyone who during my studies has helped even with the simplest gestures.

Contents

List of Tables	v
List of Figures	vi
List of Acronyms	ix
1 Introduction	1
1.1 Thesis Outline	2
2 Bladed Discs	3
2.1 High Cycle Fatigue Problem	6
2.1.1 Static Analysis	7
2.1.2 Modal Analysis	8
2.1.3 Forced Response	11
2.1.4 Mistuning	17
2.1.5 Fatigue Diagrams	18
3 The Finite Element Method	20
3.1 Description of Motion	22
3.2 Stress and Strain	23
3.2.1 Green Strain Tensor	24
3.2.2 Stress Tensors	25
3.3 Isoparametric Element	26
3.3.1 Quadratic Triangular Element	27
3.4 Building the Campbell Diagram	31
4 Harmonic Balance Method	34
4.1 Duffing Oscillator	34
4.2 Multi-Degrees of Freedom Systems	36
5 Model Order Reduction	41
5.1 Component Mode Synthesis Methods	42
5.1.1 Modal Truncation	42

5.1.2	Guyan Reduction	43
5.1.3	Craig-Bampton Method	44
5.2	Hybrid Method	46
6	Free Vibrations of a Rotationally Periodic Structure	49
6.1	Tuned System Model	49
6.2	Eigenvalues and Eigenvectors	51
6.3	Travelling and Standing Wave	54
6.4	Equivalent Model	55
6.5	Frequency Veering	56
7	Nonlinear Forced Response of Bladed Disc	59
7.1	Problem Definition	59
7.2	Contact Model	62
7.3	Solution Technique	64
7.3.1	Continuation Algorithm	68
8	Numerical Analysis of a Bladed Disc	71
8.1	Model Properties	71
8.1.1	Boundary Conditions	73
8.2	Static Loading	73
8.3	Modal Analysis	74
8.3.1	SAFE Diagrams	76
8.3.2	Analysis Validation	77
8.4	Reduced Model	80
8.5	Forced Response	85
8.5.1	EO Selection	86
8.5.2	Engine Order 52	87
8.5.3	Comparison with NOVA	95
8.6	A Different Shroud Geometry	97
8.6.1	Modal Analysis	98
8.6.2	Forced Response	99
9	Conclusion	105
A	CalculiX Input Files	107
A.1	Modal Analysis	107
A.2	Reduced Order Model	108
A.2.1	Modeshapes	108
A.2.2	Static Correction	109

B Ansys Input Files	111
B.1 Modal Analysis	111
B.2 Reduced Order Model	112
Bibliography	115

List of Tables

2.1	Engine Order Excitation	13
8.1	Mesh Properties	73
8.2	Standard Titanium Properties	74
8.3	Reduced Model Properties	82
8.4	FORSE Setup	86
8.5	EO vs. ND	87
8.6	Mesh Comparison	97
8.7	MOR Comparison	100
8.8	FORSE Setup	101

List of Figures

2.1	Bladed Disc Periodic Structure, [1]	3
2.2	Fundamental Sector Representation	4
2.3	Turbomachinery Configuration	5
2.4	Blade Configuration [2]	5
2.5	Common Types of Friction Joints	6
2.6	HCF Design and Verification Process, [8]	7
2.7	Nodal Diameters Visualization	8
2.8	Orthogonal Modes for ND= 1	9
2.9	Fundamental sector of a simplified bladed disk, [4]	10
2.10	Complex Response, [13]	11
2.11	Campbell Diagram	12
2.12	Zig Zag Diagram, [15]	13
2.13	SAFE Diagram, [13]	14
2.14	Interference Diagram, [17]	14
2.15	SAFE Diagram Construction, [16]	15
2.16	Response to different Engine Orders, [13]	15
2.17	Generic Contact Model, [18]	16
2.18	Damper Mass Effects, [19]	16
2.19	Unstable Nonlinear Response	17
2.20	Mistuning Effect on Forced Response, [20]	18
2.21	Wöhler Diagram	19
2.22	Goodman-Haigh Diagram, [21]	19
3.1	Displacement and Deformation of the body [22]	22
3.2	Deformation in the Lagrangian description [22]	23
3.3	Quadratic Tetra Element Representation, [24]	27
3.4	Campbell diagram for a single mode shape	32
3.5	SAFE diagram of a single mode shape	32
4.1	Duffing Oscillator	35
4.2	AFT algorithm scheme, [1]	37
4.3	Continuation Algorithm: Rik's method, [31]	39
4.4	Stability of the oscillation	40
4.5	Gibbs phenomenon	40

6.1	1DOF Bladed Disc Model	49
6.2	Nodal Diameter Visualization	53
6.3	Eigenvector Rigid Rotation	54
6.4	Equivalent Model	56
6.5	2 DOFs per Sector Model	56
6.6	2 DOFs Equivalent Model	57
6.7	Frequency Veering	58
7.1	Friction Laws, [1]	63
7.2	Contact Element	63
7.3	AFT Block Diagram	67
7.4	Solution Branch, [44]	68
8.1	Analysis Outline	72
8.2	FE Model	73
8.3	Boundary Conditions	74
8.4	Static Displacements of the Cantiliver Blade	75
8.5	Static Displacements for Fixed Shroud	75
8.6	Frequency vs. ND @ $\Omega = 5000$ rpm	76
8.7	Mode Shape Comparison	76
8.8	Mode #1 (FW)	77
8.9	Mode #2 (1E)	77
8.10	Mode #3 (“Mixed”)	78
8.11	Mode #4 (“Mixed”)	78
8.12	Mode #5 (1F)	79
8.13	Fixed Shroud Frequencies Comparison	79
8.14	Cantilever Frequencies Comparison	80
8.15	Nonlinear Nodes	81
8.16	Comparison of the reduced models	82
8.17	MAC: complex mode shapes	83
8.18	MAC: comparison of $ND = 0$ mode shapes only	84
8.19	Linear Response for $EO = 23$	84
8.20	Linear Response for $EO = 23$: CS on nonlinear node set only	85
8.21	Force to z	86
8.22	EO 52 Forced Response	87
8.23	EO 52 Forced Response with 10 N of preload	88
8.24	Steady-state Response at 1 st peak	89
8.25	Choice of the Harmonics	90
8.26	Modes Retained	91
8.27	Preload Analysis	92
8.28	Excitation Level ($N_0 = 100$ N)	92
8.29	F_0 alternative directions	93
8.30	Excitation Direction ($N_0 = 100$ N)	93
8.31	k_n and k_t Effect on the Response	94

8.32	Damping Effect on the Response	94
8.33	Comparison of Response ($EO = 23$)	95
8.34	Comparison of Response ($EO = 45$)	96
8.35	Comparison of Response ($EO = 52$)	96
8.36	Geometry Comparison	97
8.37	Cantilever Configuration: Natural Frequencies Comparison	98
8.38	Cantilever Configuration: Natural Frequencies vs. ND	99
8.39	Fixed Configuration: Natural Frequencies Comparison	99
8.40	Modified shroud modelling	100
8.41	Gap Element Normal Force	101
8.42	Modified Shroud Forced Response	102
8.43	Clearance Effect on the Response	103
8.44	Forced Response Comparison	104

List of Acronyms

AFT Alternating Frequency Time scheme.

BC Boundary Condition.

CMS Component Mode Synthesis.

CS Cyclic Symmetry.

DOF Degree of Freedom.

EO Engine Order.

FEM Finite Element Method.

FFT Fast Fourier Transform.

FOD Foreign object damage.

FRF Frequency Response Function.

HBM Harmonic Balance Method.

HCF High Cycle Fatigue.

IBPA Inter-Blade Phase Angle.

MAC Modal Assurance Criterion.

MOR Model Order Reduction.

ND Nodal Diameter.

ODE Ordinary Differential Equation.

Chapter 1

Introduction

Over the years, great progress has been made in the field of structural dynamics: assemblies, in order to comply with increasingly stringent standards in terms of energy efficiency, are moving in a direction of decreasing mass but gaining stiffness. This has made it more difficult to estimate their nonlinear behaviour both because of the new complex materials that have been developed, as composites, and because of the presence of friction contact. Given the high costs involved in experimental testing of components, the need for increasingly accurate software, able to predict the behaviour of the structure, has increased exponentially. The use of these new methodologies has lowered the cost and time required to develop new components: being able to verify the goodness of the design directly during the earlier stages of the development has greatly reduced the number of iterations required, as well as the number of prototypes to be produced for final verification.

EXPERTISE¹, acronym of “models, EXPeriments and high PERformance computing for Turbine mechanical integrity and Structural dynamics in Europe”, is a European multidisciplinary research activity focussed on the development of advanced tools for the dynamics analysis of large scale models of turbine components and it is an Innovative Training Network in the frame of the “MARIE SKŁODOWSKA-CURIE” actions of Horizon 2020. The goal is to pave the way towards the virtual testing of the entire machine by addressing some of the current challenges in the field of nonlinear structural dynamics of turbo-machines on the way to a fully validated nonlinear dynamic model of turbo-machinery components.

This project focused on the problem of high cyclic fatigue in bladed discs: in particular, the analyses necessary to verify the design were carried out using the finite element codes CalculiX and FORSE. Checking the nonlinear vibrations response is now common practice in the aerospace industry, as these are the cause of most component fatigue failures.

¹[EXPERTISE website](#)

1.1 Thesis Outline

In this thesis, in addition to the discussion of the analyses carried out, the context within which they are conducted is also presented, starting with why they are necessary and ending with the presentation of the results. In particular, the thesis has been divided as follows:

- Chapter 2 first introduces the bladed discs and then the problem they face with high cyclic fatigue: why this phenomenon is so studied and how it is addressed.
- Chapter 3 introduces the finite element method, showing how it is possible to discretize a generic body into a finite number of degrees of freedom in order to study its static and dynamic behaviour. Eventually it also shows how to construct a Campbell and a SAFE diagram, both widely used when it comes to check the resonances.
- Chapter 4 presents the harmonic balance method, used to compute the steady state response to an harmonic excitation: the strength of this frequency based method, compared to a time integration scheme, is The speed and ease with which the response is computed. However, as it determines a huge increase in the number of degrees of freedom, when dealing with big assemblies a reduced model is preferred. Thus, in Chapter 5, first a description of what a reduced model is and why it is convenient is provided, then different model order reduction techniques are presented.
- In Chapter 6, a simplified model of a bladed disc is studied in order to highlight the main characteristics of its dynamic behaviour. Meanwhile Chapter 7 illustrate how the discretized bladed disc is analysed: which boundary conditions are applied, how the contact between adjacent shrouds is modelled and finally the solution technique, used to compute the nonlinear response, is presented.
- Chapter 8 contains the numerical analyses of a bladed disc provided by SAFRAN: a complete description from the construction of the mesh to the nonlinear forced response is provided. The static and modal analyses have been carried out in *CalculiX*, a free finite element code, and the results have been verified with *SC03*, the Rolls-Royce proprietary software, and *Ansys*. Instead, the nonlinear response analysis has been run in *FORSE*, a software developed by Imperial College. A sensitivity study has been carried, investigating how different parameters, such as contact stiffness, shroud geometry and others, affect the final response.

Chapter 2

Bladed Discs

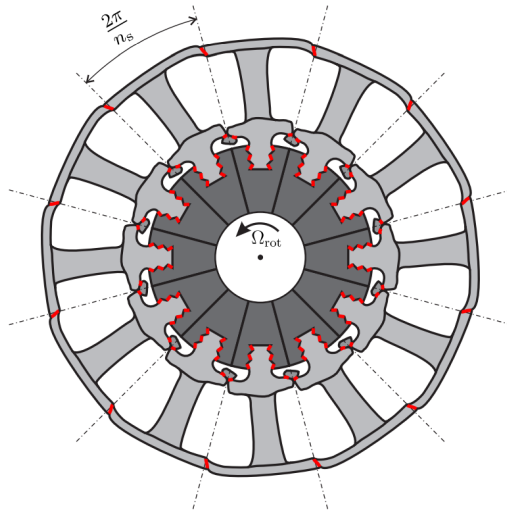


Figure 2.1: Bladed Disc Periodic Structure, [1]

The bladed disc is the fundamental unit of steam and gas turbines, whose applications are many: they range from aeronautical and marine propulsion to industrial applications such as oil&gas and power generation. Each blade is designed to be identical: therefore the constitution of a bladed disc can be described as a periodic structure, as shown in Figure 2.1, where the bladed disc can be divided into n_s identical sectors. Two main components of the sector, represented in Figure 2.2, can be identified: the blade and the disc.

However, the bladed disc is not the only type of turbomachine components: in fact there is also the so-called *blisk or integrally bladed rotor (IBR)* where the blades and the disc of a rotor form a single assembly. Obviously, there are pros and cons to using one instead of the other: the main advantage of the blisk is the elimination of the connecting parts, such as screws and bolts, between the blades and the disc, thus

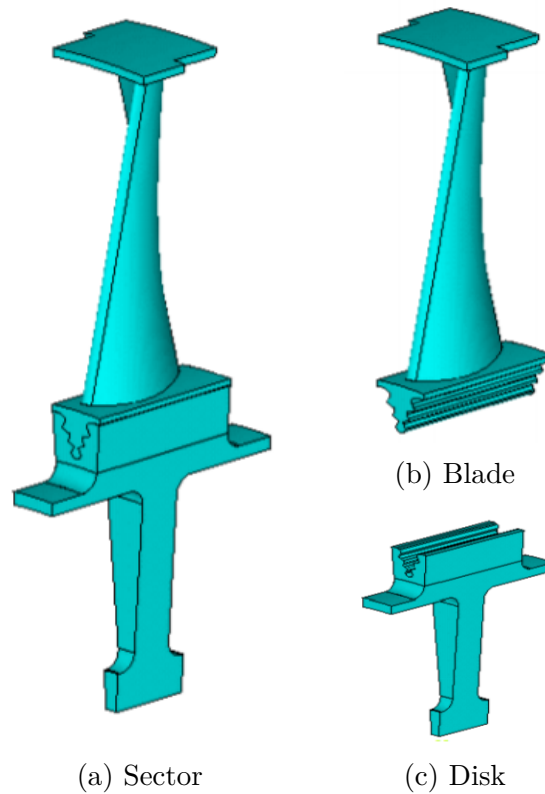


Figure 2.2: Fundamental Sector Representation

decreasing the weight, while at the same time increasing the aerodynamic efficiency. Instead the main problem is represented by the maintenance: in case of extensive damage, it is required, in the blisk rotor, to replace the whole assembly, at costs significantly higher than the partial repair of a conventional rotor. Moreover the absence of connecting parts means also the loss of mechanical damping generated by them.

Moreover the bladed disc comes in two configurations based on the type of blade used: a cantilever one and a shrouded one. The advantage of the latter is the addition of stiffness, which increases the natural frequencies, but it also introduces damping due to friction in the relative sliding between adjacent shrouds, which determine a nonlinear contact behaviour.

A good mechanical design is of *extreme importance* as the bladed discs are heavily stressed during operations. In addition to static stress sources such as thermal loads, fluid pressures and centrifugal loads, dynamic stresses are present as well: these vibrations are induced by additional dynamic loads primarily of aero-elastic nature.

Therefore a persistently high dynamic load coupled with static stresses can damage the disc causing cracks induced by the **high cycle fatigue phenomenon**. Hence why it is necessary to estimate dynamic stresses and verify the strength of

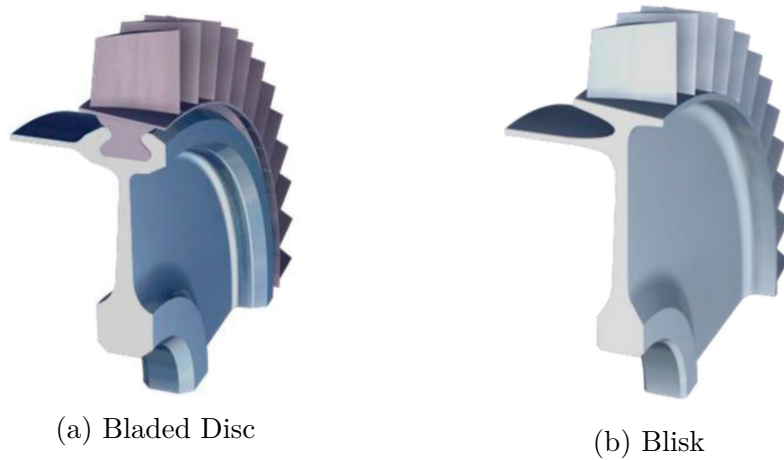


Figure 2.3: Turbomachinery Configuration

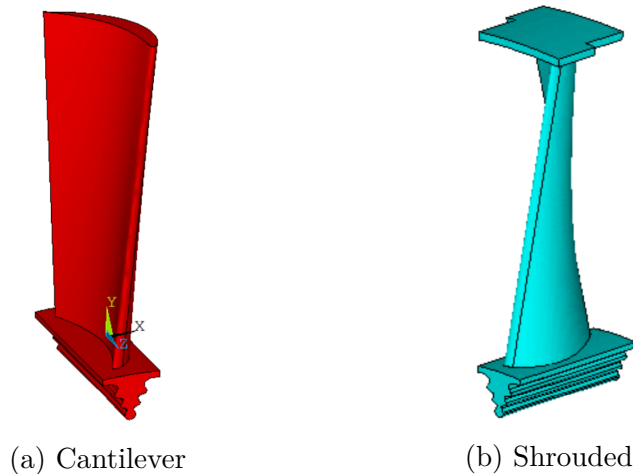


Figure 2.4: Blade Configuration [2]

the structure by performing a forced response analysis over the operating speed range. As previously said, the main vibration mechanisms are of aeroelastic nature: the bladed disc is mainly excited due to the non-stationary flow and flutter, a self-excited phenomenon caused by aerodynamic damping. [3]

Dealing with the forced response of such structures is not trivial: in fact their behaviour is highly nonlinear. In addition to geometric nonlinearities, the presence of multiple contact surfaces, see Figure 2.5, requires to take into account the friction damping, due to slip phenomena at those interfaces, in order to compute the forced response and predict accurately the stress level. [4]

Moreover The complexity of the analysis can further increase if thermal loads, causing creep phenomena [5], mistuning [6] and the coupling between different stages

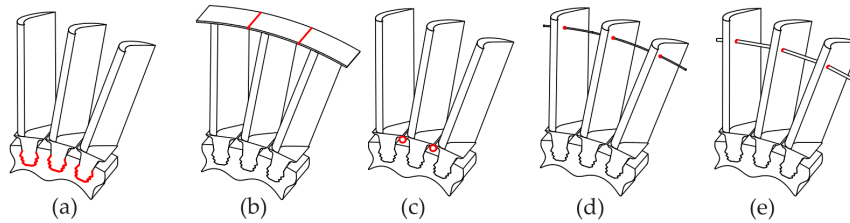


Figure 2.5: Common types of friction joints: (a) roots joints, (b) tip shrouds, (c) underplatform dampers, (d) damper wires, (e) damper pins [1]

of the gas turbine [7] are considered.

2.1 High Cycle Fatigue Problem

This section focuses on the procedure for checking the resistance of the bladed disc to the HCF as the High Cycle Fatigue is the largest single cause of component failures in aircraft gas turbine engines: since this problem affects all engine sections and a wide range of materials, it causes a significant economic impact.[8]

Although design criteria and prediction approaches have continuously improved, the constant increase in engine performance has resulted in the reduction of the weight and the rise of temperature, stresses and stage loading: therefore not only HCF occurrences have persisted but the percentage of failures caused by this phenomenon has increased.

The reason why it is so dangerous and problematic from the economic point of view of the manufacturer is that if the blade is not designed to be resonance proof, its HCF life of 10^7 cycles can be reached in minutes or hours during start-up operations. It may be useful to note here that the entire high cyclic fatigue life consists of up to the initiation of the crack as, once initiated, the crack propagates very rapidly in the material following the Low Cyclic Fatigue mechanisms. [9]

The current approach to evaluate HCF capability is shown in the flow chart of Figure 2.6: the method is highly empirical and it does not address complicating factors such as the interaction between different damage modes, foreign object damage and fretting.

Nowadays, engine manufacturers mainly mitigate HCF risks by:

- Avoiding dangerous resonance in the operating range but as it is impossible to remove all the resonances, generally the first modes are the ones to be avoided as they are also more dangerous.
- Accepting resonance in the operating range and estimating its associated response level early in the design process in order to keep it under the dangerous level.

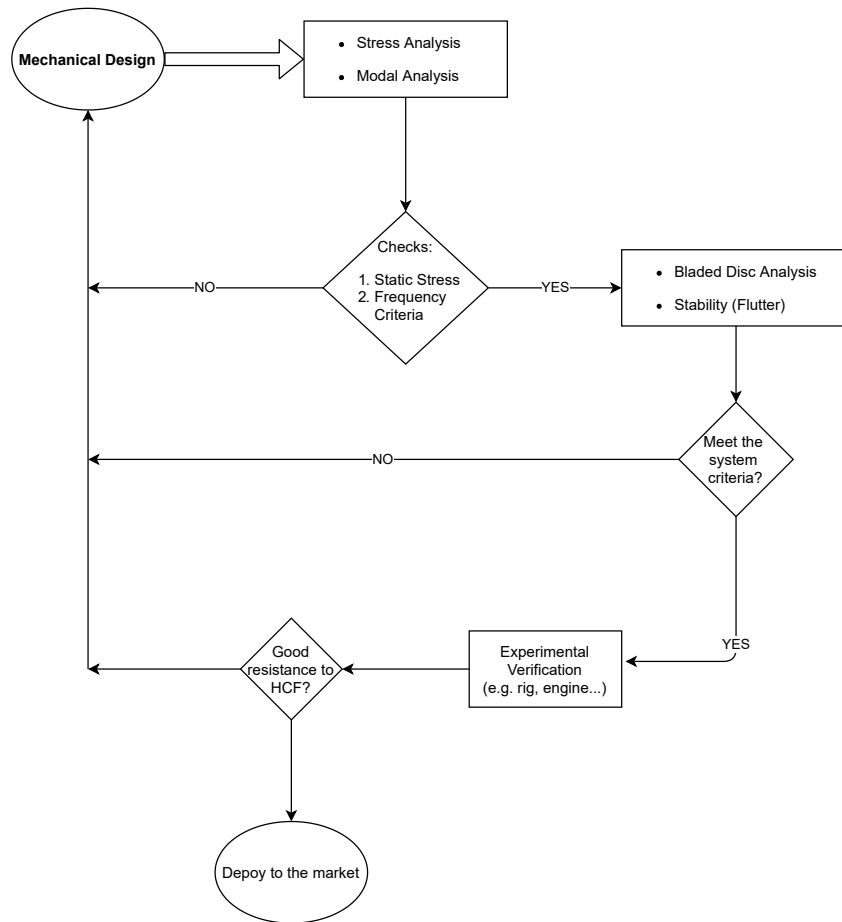


Figure 2.6: HCF Design and Verification Process, [8]

2.1.1 Static Analysis

First and foremost a static analysis is carried on: estimating static loads due to the rotational speed, the temperature and the steady aerodynamic forces is very important in order to evaluate the ability of the material to accept extra dynamic stresses. Other benefits are also a greater tolerance to FOD and longer a life.

In the ideal case of a tuned assembly, bladed disks can be studied as cyclic symmetric structures: in fact this class of periodic structures is formed by a finite number N of identical substructures, each one constituted by J degrees of freedom. This property is exploited using cylindrical coordinates and allows to reduce the computational cost by modelling only one sector made up by the blade and the disc.

Therefore is sufficient to solve the problem

$$\mathbf{F} = [\mathbf{K}]\mathbf{x} \quad (2.1)$$

for a single fundamental sector, while constraining the lateral faces so that the

displacements are equal in order to guarantee the structure continuity. The solution required can be nonlinear, in case of large displacements, or linear. If the former the stiffness matrix is updated considering two additional contribution: one coming from the structure deformation the other from the force field evolution (spin softening). [10]

2.1.2 Modal Analysis

Being circular, discs experience vibratory modes characterized by having *nodal diameters*, i.e. diameters where displacements are zero, and *nodal circle patterns*: these modes may be fixed relative to the disk or may travel in the same or opposite direction to that of the rotor speed. [3]

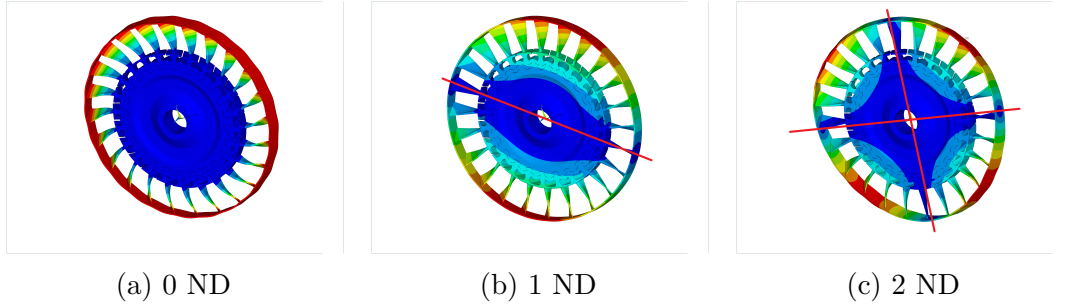


Figure 2.7: Nodal Diameters Visualization

This behaviour can be highlighted by looking at the eigenproblem of the entire assembly

$$[M]\ddot{\mathbf{x}} + [K]\mathbf{x} = \mathbf{0} \quad (2.2)$$

that, indeed, presents a particular characteristic: the mass and stiffness matrices are block circulant as the structure is **rotationally periodic**.

The generic eigenvector ϕ can be partitioned in a convenient way so that the J degrees of freedom of the first substructure are followed by the J degrees of freedom of the second substructure, and so on.

$$\phi = \left\{ \phi^{(1)} \quad \phi^{(2)} \quad \dots \quad \phi^{(N-1)} \quad \phi^{(N)} \right\}^T$$

However, all the possible mode shapes ϕ of a cyclic symmetric structure fall into three classes, depending on the relative motion between the sectors: [11]

1. The sectors have the same mode shape of its neighbours, if using a cyclic coordinate system, and vibrates in phase with them

$$\phi_i^{(n)} = \phi_i^{(n+1)}$$

where ϕ_i^n is the i -th eigenvector of the n -th sector.

2. The sectors have the same mode shape of its neighbours but vibrate in opposition of phase with them

$$\phi_i^{(n)} = -\phi_i^{(n+1)}$$

this class exists only if the number of sector N is even.

3. All the other possible mode shapes.

Focusing on the 3rd case, since the structure is cyclic symmetric, after a rotation of $\alpha = 2\pi/N$ of ϕ_i a new valid eigenvector

$$\hat{\phi}_i = \left\{ \phi^{(N)} \quad \phi^{(1)} \quad \dots \quad \phi^{(N-2)} \quad \phi^{(N-1)} \right\}^T$$

with the same eigenvalue is obtained. However, the new eigenvector is not orthogonal to the previous one: therefore to obtain $\hat{\phi}_i$ there has to be an eigenvector ϕ'_i orthogonal to ϕ_i with which it shares the same eigenvalue. This means that there is a rotational relationship between eigenvectors of adjacent sectors

$$\begin{Bmatrix} \hat{\phi}_i \\ \hat{\phi}'_i \end{Bmatrix} = [R]_\alpha \begin{Bmatrix} \phi_i \\ \phi'_i \end{Bmatrix} \quad (2.3)$$

That is also why the eigenproblem is considered to have a *double multiplicity*, i.e. for each natural frequency an orthogonal pair of eigenvectors is found.

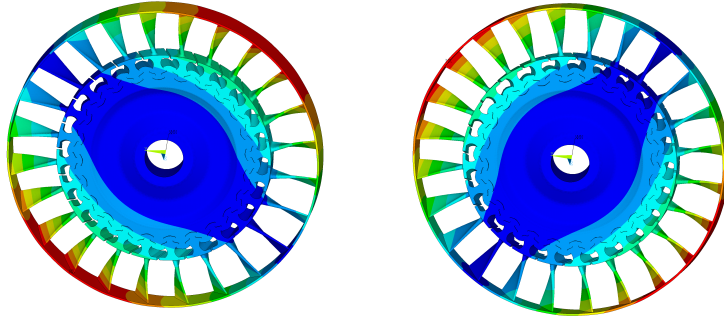


Figure 2.8: Orthogonal Modes for ND= 1

This also means that any linear combination of these eigenvectors is still a valid eigenvector of the system: therefore a complex mode shape can be defined

$$\Theta_i = \phi_i + i\phi'_i$$

as well as its conjugate Θ'_i .

Thus, by applying subsequent shifts of α -s to the base comprising ϕ_i and ϕ'_i , it is possible to obtain the full set of eigenvectors of the assembly.

Regardless of the type, the kinematics characterizing mode shapes is identified by the phase angle between adjacent vibrating sectors. This angle is called inter-blade phase angle (IBPA)

$$\varphi = h \cdot \alpha \quad \rightarrow \quad 0 < \varphi < \pi \quad (2.4)$$

where $0 < k < \text{int}[N/2]$ is the number of nodal diameters.

Cyclic Symmetry

In both analyses, the cyclic symmetry hypothesis allows to reduce the problem from the entire assembly of NJ degrees of freedom to the fundamental sector made of J DOFs only.

While for the static case the boundary conditions are pretty straightforward, for the dynamic analysis the assumption that the lateral faces have the same displacements does not apply any more and the continuity of the structure is obtained by allowing a *constant phase angle*, the IBPA, between each sector. [10]

Both a real [12] and a complex-value [13] based methods are possible: they both use the cyclic symmetry theory to correlate any physical quantities of the assemblies to a corresponding quantity in cyclic coordinates of the fundamental sector.

Both transformations yield a problem dependant on the harmonic index k , equivalent to the nodal diameters, in the sense that the resulting mass and stiffness matrices are k -dependant therefore the modal analysis has to be computed for each nodal diameter k .

Moreover, the problem can be further reduced by exploiting the cyclic symmetry to constrain one of the sides

$$\mathbf{q}_H = \mathbf{q}_L e^{i\varphi} \quad (2.5)$$

where \mathbf{q}_H and \mathbf{q}_L are the interface DOFs of the fundamental sector sides as shown in Figure 2.9.

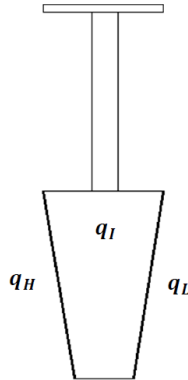


Figure 2.9: Fundamental sector of a simplified bladed disk, [4]

The mode shapes characterized by $k = 0$ and $k = N/2$ correspond to standing waves, whose eigenvectors are real in both approaches and their multiplicity is one being of the 1st and 2nd type respectively.

While for the other indexes the eigenvectors obtained with the two approaches are different, they are still linked by a linear relationship and the two methods are equivalent. The advantage of using a complex notation is being able to describe the travelling wave concept as well as the phase, i.e. the imaginary part, between the response of the different sectors as shown in Figure 2.10

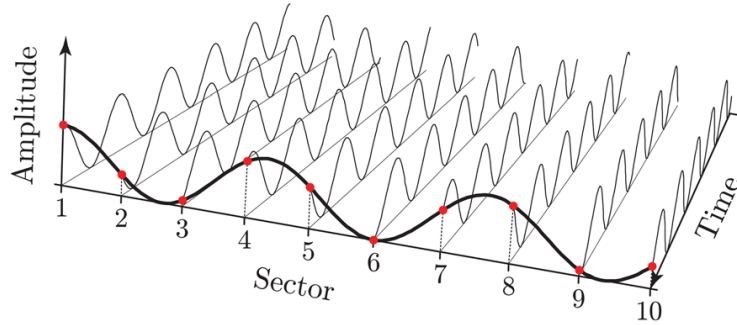


Figure 2.10: Complex Response, [13]

In particular the mode shapes with $0 < k < N/2$ rotate clockwise and those with $k > N/2$ rotate counter-clockwise.

In summary assuming a sector size of J dofs, a real-valued cyclic symmetry approach leads, in the worst case, to one eigenvalue problem of size J and $(N - 1)/2$ eigenvalue problems of size $2J$; a complex approach leads to N eigenvalue problems of size J ; while the full analysis leads to a single, but very costly, eigenvalue problem of size NJ . [12]

2.1.3 Forced Response

The sources of excitation in the engine are numerous and most of them are periodic: effectively, blades excitations are mainly due to non uniformity of the upstream pressure field, but other aerodynamic and mechanical excitations are present as well. [10]

So, when rotating, the blades see a *fluctuating pressure field* at a frequency connected to the rotational speed, this periodicity can be exploited by dividing the periodic force into its *harmonic component*. Given the symmetry of the assembly, each sector is excited by the same harmonic force, but with a phase lag.

Campbell Diagram

Once the mode shapes have been computed, the next step of the analysis is to check that the natural frequencies of the blades are not excited within the operating range.

A tool commonly used for this purpose is the **Campbell** diagram, see Figure 2.11 for an example: the bladed disc natural frequencies, in red, are plotted as a function of the rotational speed while the straight dashed lines corresponds to the multiple harmonic excitations. The crossing between the excitation and the natural frequencies allows to identify resonances.

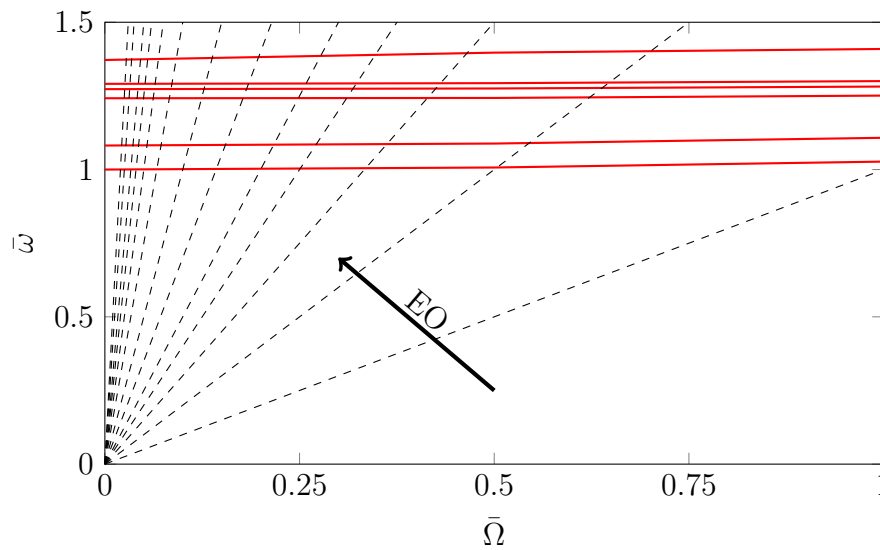


Figure 2.11: Campbell Diagram

Usually lower order modes are the most dangerous ones as a higher modal mass is involved leading to more severe damage. As it is not possible to exclude every crossings, the more dangerous modes are accurately verified (forced response study, engine testing, etc.).

In literature, e.g. [14], it is possible to find multiple studies about the natural frequency variation of the blade with respect to the rotational speed.

Engine Order Excitation

As the excitation is divided into multiple harmonics component, whose frequency base is the rotational speed Ω : the **engine order** parameter EO is introduced to identify the harmonic of the excitation. Each harmonic component excites the sector at a frequency equal to $EO \cdot \Omega$, but it can be shown that for a given mode family each it is not true that every engine order can excite any nodal diameter

associated frequency: instead each engine order excites only certain frequencies as shown in Table 2.1

Excited ND	Engine Order
0	mN
1	$1+mN$
2	$2+mN$
...	...
$N-2$	$N-2+mN$
$N-1$	$N-1+mN$

Table 2.1: Engine Order Excitation

The relationship between the nodal diameter and the engine order that can excite is represented in the so-called Zig Zag Diagram, an example is shown in Figure 2.12

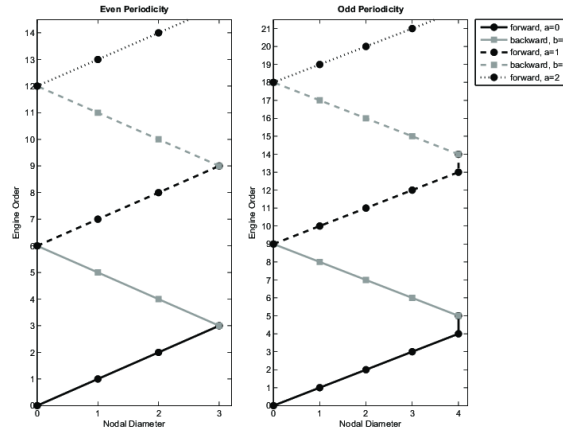


Figure 2.12: Zig Zag Diagram, [15]

SAFE Diagram

This tool, introduced by Singh et al. [16], helps predict the reliability of blading: compared to the widely used Campbell diagram, it is much more informative. In evaluating interferences, the SAFE diagram compares not only the frequencies of exciting harmonics with natural frequencies of blades, but also the shape of these harmonics with the normal mode shapes of a completely bladed disc including packeted blading. [16]

To better identify the dangerous modes, there is a need to eliminate the points of the Campbell Diagram which are of no concern in the evaluation of reliability and explaining why these points are of no concern to designers.

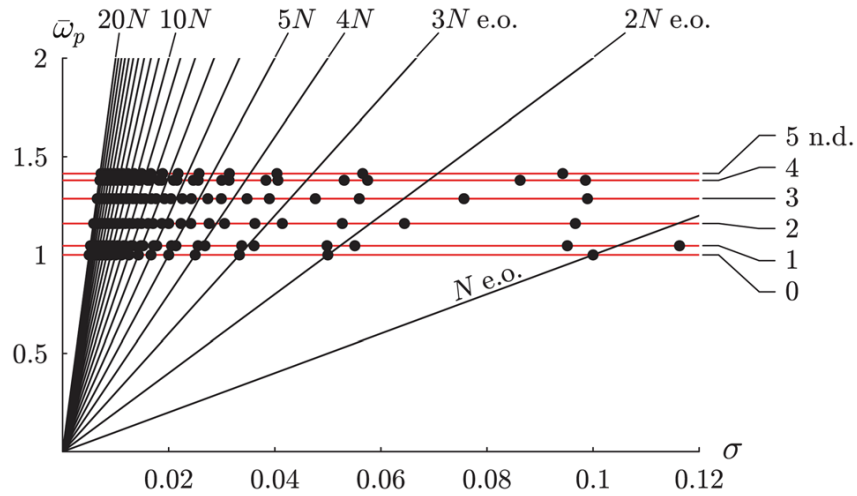


Figure 2.13: SAFE Diagram, [13]

In fact, the conclusion reached is that if SAFE diagram shows resonance then Campbell diagram will also show resonance. On the other hand if SAFE diagram shows no possible resonance, Campbell diagram might show resonance. [17] Therefore, the diagram proves to be of great help in identifying sources of resonance and in finding solutions if such conditions occur in the operating range.

As for its construction, the SAFE Diagram is built by combining the *interference diagram*, which is a Zig Zag diagram in which the natural frequencies corresponding to each nodal diameter are also shown, with the Campbell Diagram.

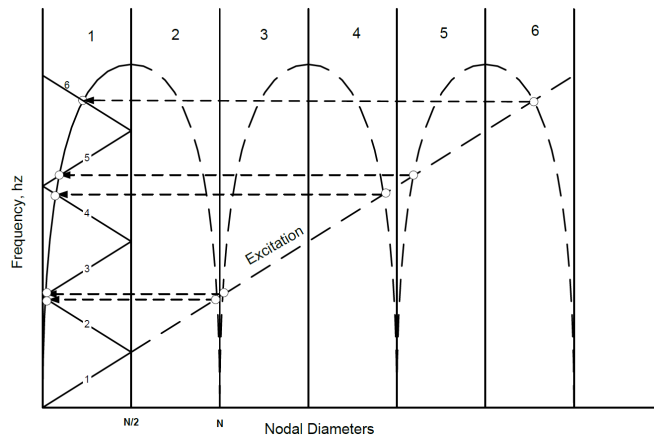


Figure 2.14: Interference Diagram, [17]

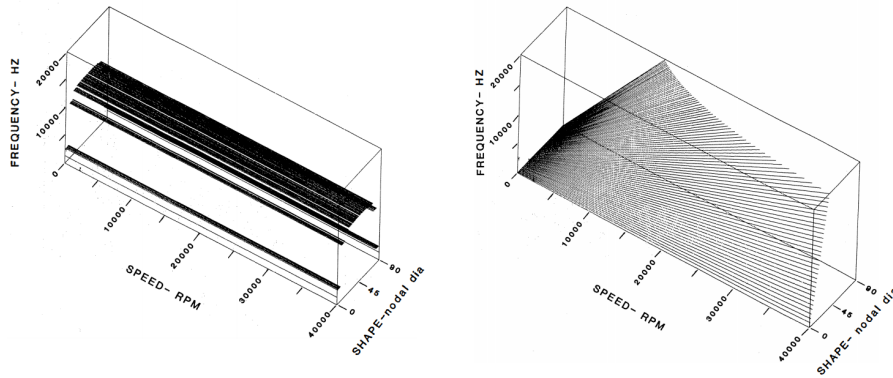


Figure 2.15: SAFE Diagram Construction, [16]

Frequency Response Function

The dangerous mode responses have to be verified: an obvious way is to use the FRF to estimate the response level.

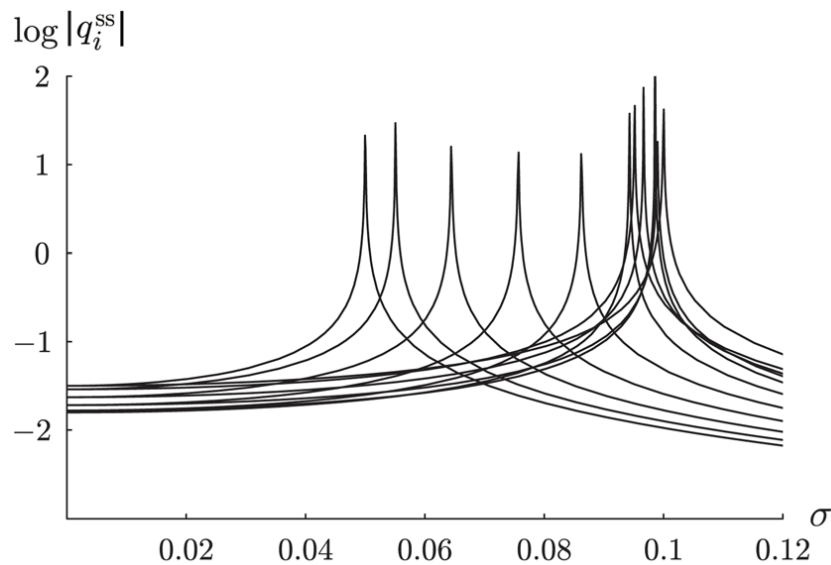


Figure 2.16: Response to different Engine Orders, [13]

In order to accurately predict the response level, damping must be introduced. The main sources are:

- Mechanical damping is due to the fact that the material is never perfectly linear: some energy is always dissipated, even under the yield stress. Another source of mechanical damping comes from friction such as the junctions behaviours at the structure parts interface.

- Aeroelastic damping: in fact, when the bladed disk vibrates, it generates unsteady pressures. These unsteady pressures can either excite the structure (flutter) or damp it.

Moreover contact has to be modelled, usually with *Coulomb's law*, in order to capture possible nonlinearities generated by the slip of adjacent sectors, mainly occurring in the shroud, if presents, in the blades connected by underplatform dampers or in the firtree.

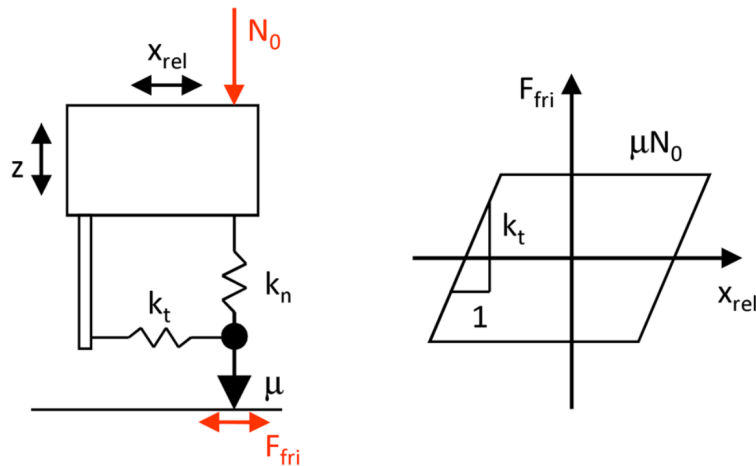


Figure 2.17: Generic Contact Model, [18]

In fact, the presence of a damper greatly influences the forced response of the bladed disc: Figure 2.18 shows how the mass of the damper affects both the amplitude and the position of the response peak.

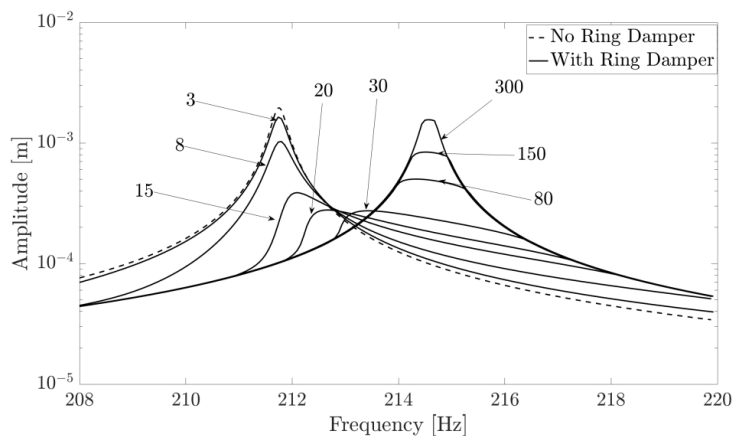


Figure 2.18: Damper Mass Effects, [19]

In addition, the presence of intermittent contacts can lead to an unstable response: where several excitation levels can be detected at one rotational speed.

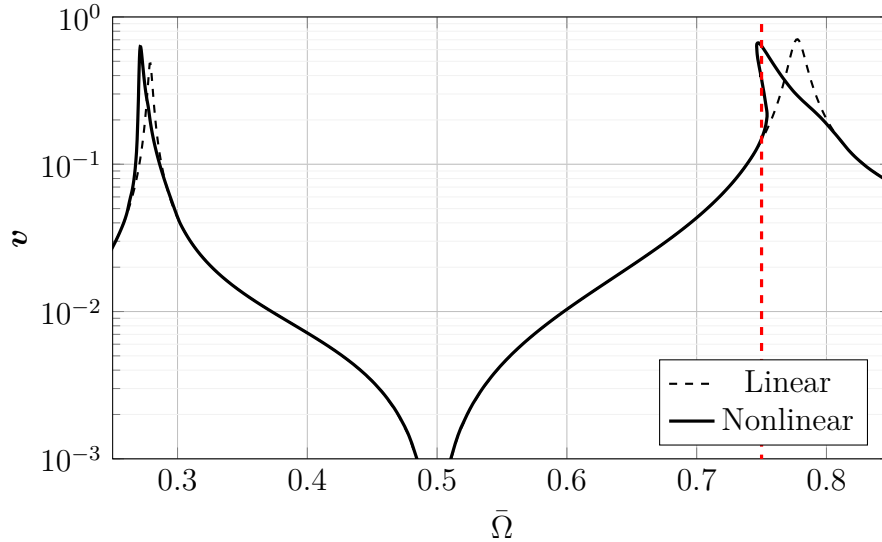


Figure 2.19: Unstable Nonlinear Response

The final numerical prediction of the resonance stresses depends significantly on the reliable estimation of excitation forces as well as the trustworthy damping values, which are often unknown parameters in the design process. Therefore, the HCF design is based principally on the determination of the allowable amplitude of alternating stresses with respect to the computed FE mean stresses.

2.1.4 Mistuning

In reality disk assemblies are not perfectly tuned: in fact there are many sources of *variability* such as manufacturing tolerances, mounting clearances, material characteristics dispersion, etc.

Each blade dynamic behaviour is different from the others and the *frequency scatter* can reach 1 – 2% standard deviations: this scatter is called **mistuning** and it is sufficient to *break* the structure symmetry, crowding the Campbell diagram with close frequencies. [10]

In cyclic symmetry, the travelling wave on the bladed disk assured a good circulation and distribution of the vibration energy on each sector of the bladed disk. In the mistuned case, each blade response is different from the others and there is no constant phase angle between the sectors: the energy can localise on only few sectors, generating important responses on few blades.

The blade mistuning is clearly the dominant parameter: in fact looking at the number of blades on a rotor, it was observed that the larger the number of blades,

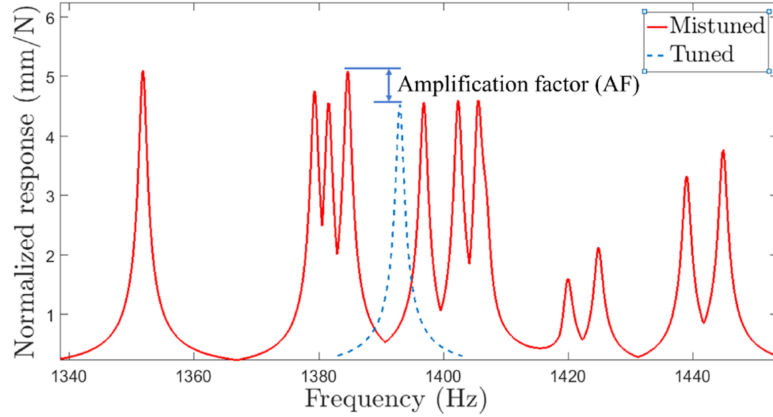


Figure 2.20: Mistuning Effect on Forced Response, [20]

the greater the influence of mistuning. [3]

The main approaches to the study of mistuning are either statistical or involve the addition of a perturbation to the mass and stiffness matrices.

2.1.5 Fatigue Diagrams

Ultimately, all of the foregoing analysis and verification testing results in an assessment of HCF margin for the component. The principal approach used to assess vibration stress margin is the modified **Goodman diagram**. The basic attraction of this approach is that allowable vibratory stress can be simply represented as a function of mean or steady stress. The fundamental tenant is that operation within the allowable region will not result in HCF failure. This life is based on the expected range where an endurance limit is approximated. The diagrams are derived from stress vs. cycles (S-N) data, after “S-N” curves for fixed mean stresses or fixed stress ratios are generated out to the desired life. [8]

Since the computed mean static stresses σ_m and the alternating ones σ_a are within the elastic range, a common life prediction tool is the Stress-Life method developed by **Wöhler**, indicated by “ σ -N” or “S-N” acronyms, where an endurance limit σ_e is determined.

It is important to note that the modal analysis does not return the absolute magnitude of the response but only its distribution: therefore stresses are normalized by the FE software.

The dynamic stress assessment is performed using a **Goodman-Haigh diagram**: on the x-axis the static stresses are reported, while on y-axis the dynamic ones.

Multiple failure hypotheses led to a variety of possible curves that estimate the maximum allowable couple of static and dynamic stresses. For each element of the structural model, the couple static and dynamic stresses are plotted in the diagram. When all the elements are located, the objective is to determine the multiplying

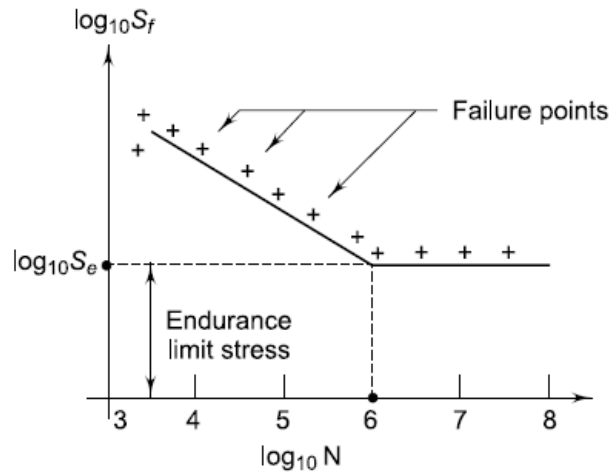


Figure 2.21: Wöhler Diagram

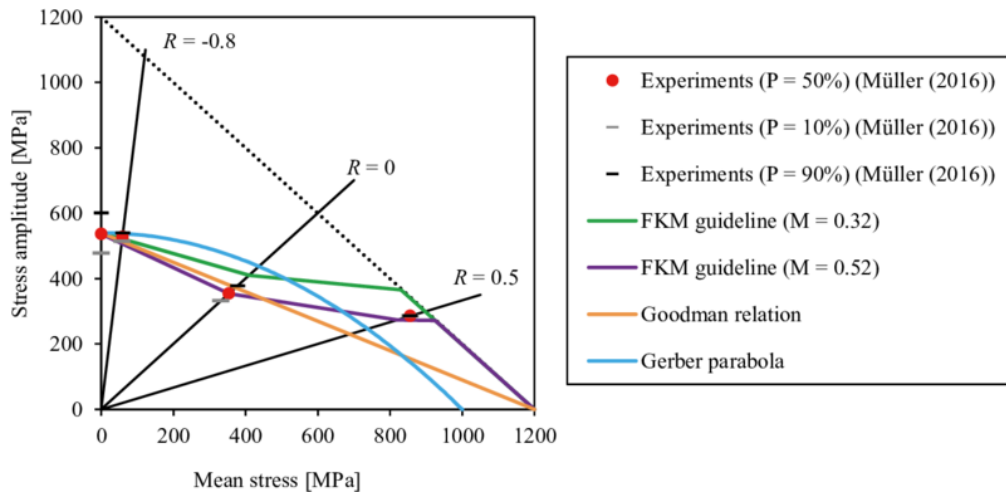


Figure 2.22: Goodman-Haigh Diagram, [21]

factor, α , applicable to dynamic stresses such as the worst couple of stress is on the modified Goodman curve and all the others are lower this curve. The following approach must be performed for each mode suspected to be excited in the operating range.

Finally the S-N method predicts the number of cycles to crack initiation for the constant load history. For real operation conditions of the machine, the loading acting on the analysed component can vary in the time domain. For these signals, the Palmgren-Miner **linear damage** hypothesis can be applied, which accounts different stress amplitudes. The latter are then ordered in blocks of stress/strain cycles, each having a constant amplitude.

Chapter 3

The Finite Element Method

With the spread of computers in the resolution of engineering problems, it has become necessary to develop numerical methods suitable for solving such problems: in fact the solution of the extended integral on a finite domain of the partial derivative equations is neither easy to find nor such formulation has general validity. What these numerical methods do is to discretize the problem and reducing it to an algebraic system of equations. The most commonly used ones are the finite differences and the finite elements: in particular the latter is the more widespread of the two thanks to its incredible flexibility, as it can be adopted for simpler domains as well as irregular ones. [22] In this chapter an introduction to its structural dynamic application, in particular for the geometrically nonlinear case, will be provided.

The basic working principle of the finite element method is the discretization of the domain by means of various elements such as beams, shells and bricks: in literature it is possible to find a library of the available elements, their formulation as well as the cases to which they are best suited.

It is therefore possible to determine what are the general steps of the finite element analysis:

1. Identify a *functional* containing all the information of the problem. There are generally two approaches:
 - Energetic Approach based on Lagrange's equation;
 - Method of Weighted Residuals, Galerkin's being one of the most popular.
2. Divide the whole domain into geometrically simple subdomains, called finite elements;
3. Careful choice of the *shape functions*, i.e. the functions approximating the unknown variables over each subdomain. Usually they are a linear combination of algebraic polynomials where the degree depends on the number of nodes of the element used;

4. Evaluate each subdomain properties and equations in order to assemble the global matrices governing the system;
5. Applying the *boundary conditions*. If fixed, it means suppressing all the rows and columns linked to the constrained degrees of freedom;
6. Solve the system with iterative or direct methods;
7. Evaluate additional unknowns, in structural analysis this means computing strains and stresses.

Before highlighting the main features of this method it is important to first understand what a nonlinear behaviour is and what may causes the system to behave this way. A nonlinear system is one in which a change in the output is not proportional to the change in the input: this means that the *superposition principle is no longer valid* for such a system. This consequence is quite important as it means the the loading history affect the response. A simple example is a quadratic relationship or any other polynomial of degree higher than one.

Generally speaking it is possible to affirm that linearity is only an idealization of the actual behaviour of any system [23] and, in reality, bladed discs always deviate from the ideal case even if there are many instances where the linearised system returns a good approximation leading to a reduction of computational cost. However, in some case the designer is forced to take nonlinearities into account: an example is the design of high performance components that need to be both lightweight and stiff.

The main cause of nonlinearity in a system are:

- Geometric nonlinearity, e.g. nonlinear strain-displacement relations;
- Material nonlinear behaviour such as hysteresis in rubber-like materials;
- Contact nonlinearities.

In this chapter geometric nonlinearities are considered in the formulation: this type of analysis is said to be a **large displacement** one. It becomes necessary when the structure's displacements are so large that the original stiffness matrix of the system does not represent the structure and the effect of the new deformed configuration have to be taken into account.

Note that a large displacement analysis can still lead to small strain, meaning that the material remains elastic and consequently that the structure returns to its original configuration when the loading is removed.

3.1 Description of Motion

Consider a deformable body to which a system of forces is applied: this causes the body to move and deform. Now call C_0 the initial configuration and \mathbf{X} the position, referred to a rectangular Cartesian system X_1, X_2, X_3 , occupied by the particle X , belonging to the body. Due to the external loading, the body moves and deforms, as shown in Figure 3.1, finding itself in the new configuration C . Moreover, after a displacement \mathbf{u} , the particle now occupies the position \mathbf{x} . The initial configuration

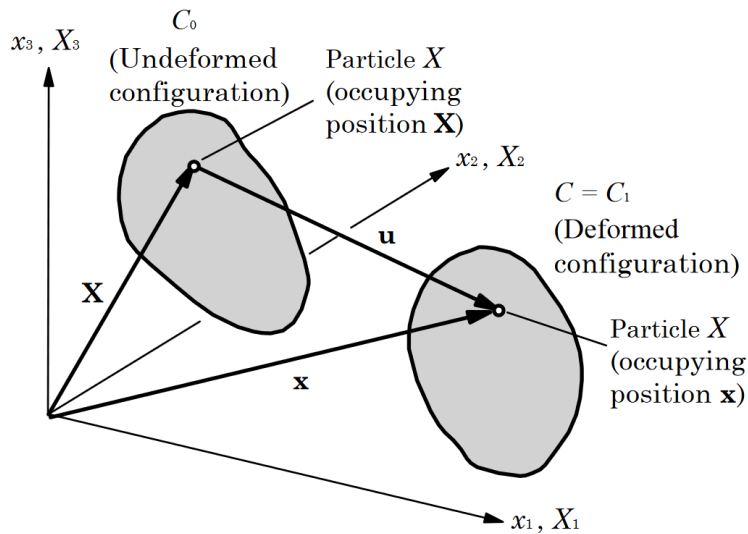


Figure 3.1: Displacement and Deformation of the body [22]

is described in the *material coordinates system* (X_1, X_2, X_3) , while the deformed configuration is defined with respect to a new coordinates system called *spatial coordinates*, (x_1, x_2, x_3) .

There are therefore two possible description of the motion:

- A first approach, the *Lagrangian description*, follows the motion of the body over time and it is referred to a reference configuration, usually the **undeformed** one C_0 . Thus the spatial coordinates are expressed as a function of the material ones

$$\mathbf{x} = \mathbf{x}(\mathbf{X}, t)$$

This approach is typically used in structural mechanics problems where the body is subject to deformation. [24]

- The other approach is the *Eulerian description*, where the attention is focused on the space portion \mathbf{x} and not on the particle X . This means that the motion

is referred to the current **deformed** configuration C

$$\mathbf{X} = \mathbf{X}(\mathbf{x}, t)$$

This approach is not suited to structural mechanics since most of the time the deformed configuration is unknown. Instead it is preferred when treating with fluid mechanics problems as the volume remains unchanged making it easier to determine the changes in the fluid velocities, pressure, density and so on. [22]

From now on a Lagrangian description will be followed.

3.2 Stress and Strain

In order to define the deformation of a continuum, two adjacent points P and Q are studied. The distance between these points is infinitesimal

$$d\mathbf{X} = \mathbf{X}_Q - \mathbf{X}_P$$

and after the deformation becomes

$$d\mathbf{x} = \mathbf{x}_Q - \mathbf{x}_P$$

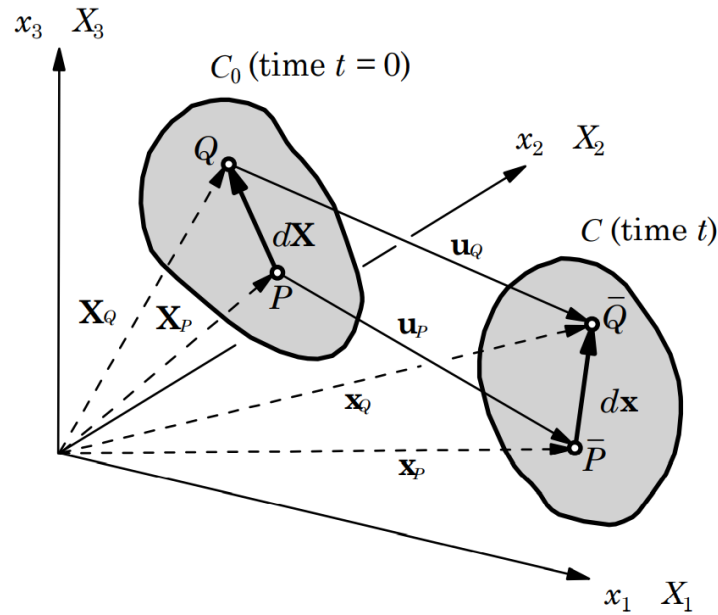


Figure 3.2: Deformation in the Lagrangian description [22]

Meanwhile the displacement for each point can be written as

$$\mathbf{u} = \mathbf{x} - \mathbf{X} \tag{3.1}$$

From these informations, it is now possible to compute the *deformation gradient tensor*, which expresses the relationship between the distance before and after the deformation

$$d\mathbf{x} = \mathbf{F} \cdot d\mathbf{X} = d\mathbf{X} \cdot \mathbf{F}^T \quad (3.2)$$

where

$$\begin{aligned} \mathbf{F} &= \left[\frac{\partial \mathbf{x}}{\partial \mathbf{X}} \right]^T \equiv (\nabla_0 \mathbf{x})^T \\ &= \mathbf{I} + \left[\frac{\partial \mathbf{u}}{\partial \mathbf{X}} \right]^T = \mathbf{I} + (\nabla_0 \mathbf{u})^T \end{aligned} \quad (3.3)$$

with ∇_0 indicating the gradient with respect to \mathbf{X} .

3.2.1 Green Strain Tensor

Now there is a need to define a measurement of the body deformation: to do this, once again, the distance between the two points P and Q before and after applying the load is taken as a reference.

To compute it, first, the following quantities need to be introduced

$$(d\mathbf{S})^2 = d\mathbf{X} \cdot d\mathbf{X} \quad (3.4)$$

$$\begin{aligned} (d\mathbf{s})^2 &= d\mathbf{x} \cdot d\mathbf{x} = (\mathbf{F} \cdot d\mathbf{X}) \cdot (\mathbf{F} \cdot d\mathbf{X}) = d\mathbf{X} (\mathbf{F}^T \cdot \mathbf{F}) d\mathbf{X} \\ &= d\mathbf{X} \cdot \mathbf{C} \cdot d\mathbf{X} \end{aligned} \quad (3.5)$$

where \mathbf{C} is the right *Cauchy-Green deformation tensor*.

Finally it is possible to define the deformation of the body from the difference of the square distances as

$$(d\mathbf{s})^2 - (d\mathbf{S})^2 = 2 d\mathbf{X} \cdot \mathbf{E} \cdot d\mathbf{X} \quad (3.6)$$

where the \mathbf{E} is the **Green-Lagrange strain tensor**. It can also be expressed as

$$\begin{aligned} \mathbf{E} &= \frac{1}{2} (\mathbf{F}^T \cdot \mathbf{F} - \mathbf{I}) \\ &= \frac{1}{2} [(\nabla_0 \mathbf{u})^T + (\nabla_0 \mathbf{u}) + (\nabla_0 \mathbf{u})^T \cdot (\nabla_0 \mathbf{u})] \\ &= \begin{bmatrix} \varepsilon_{11} & \varepsilon_{12} & \varepsilon_{13} \\ \varepsilon_{21} & \varepsilon_{22} & \varepsilon_{23} \\ \varepsilon_{31} & \varepsilon_{32} & \varepsilon_{33} \end{bmatrix} \end{aligned} \quad (3.7)$$

Note that the Green strain tensor can predict rigid body motion: the change in squared length is zero **if and only if** $\mathbf{E} = 0$, i.e. the body moves rigidly.

An important property of this tensor is its symmetry: in fact its generic component is [22]

$$\varepsilon_{ij} = \frac{1}{2} \left(\frac{\partial \mathbf{u}_i}{\partial \mathbf{X}_j} + \frac{\partial \mathbf{u}_j}{\partial \mathbf{X}_i} + \frac{\partial \mathbf{u}_k}{\partial \mathbf{X}_i} \frac{\partial \mathbf{u}_k}{\partial \mathbf{X}_j} \right) \quad (3.8)$$

expanding each component

$$\begin{aligned} \varepsilon_{11} &= \frac{\partial u_1}{\partial X_1} + \frac{1}{2} \left[\left(\frac{\partial u_1}{\partial X_1} \right)^2 + \left(\frac{\partial u_2}{\partial X_1} \right)^2 + \left(\frac{\partial u_3}{\partial X_1} \right)^2 \right] \\ \varepsilon_{22} &= \frac{\partial u_2}{\partial X_2} + \frac{1}{2} \left[\left(\frac{\partial u_1}{\partial X_2} \right)^2 + \left(\frac{\partial u_2}{\partial X_2} \right)^2 + \left(\frac{\partial u_3}{\partial X_2} \right)^2 \right] \\ \varepsilon_{33} &= \frac{\partial u_3}{\partial X_3} + \frac{1}{2} \left[\left(\frac{\partial u_1}{\partial X_3} \right)^2 + \left(\frac{\partial u_2}{\partial X_3} \right)^2 + \left(\frac{\partial u_3}{\partial X_3} \right)^2 \right] \\ \varepsilon_{12} &= \frac{1}{2} \left(\frac{\partial u_1}{\partial X_2} + \frac{\partial u_2}{\partial X_1} + \frac{\partial u_1}{\partial X_1} \frac{\partial u_1}{\partial X_2} + \frac{\partial u_2}{\partial X_1} \frac{\partial u_2}{\partial X_2} + \frac{\partial u_3}{\partial X_1} \frac{\partial u_3}{\partial X_2} \right) \\ \varepsilon_{13} &= \frac{1}{2} \left(\frac{\partial u_1}{\partial X_3} + \frac{\partial u_3}{\partial X_1} + \frac{\partial u_1}{\partial X_1} \frac{\partial u_1}{\partial X_3} + \frac{\partial u_2}{\partial X_1} \frac{\partial u_2}{\partial X_3} + \frac{\partial u_3}{\partial X_1} \frac{\partial u_3}{\partial X_3} \right) \\ \varepsilon_{23} &= \frac{1}{2} \left(\frac{\partial u_2}{\partial X_3} + \frac{\partial u_3}{\partial X_2} + \frac{\partial u_1}{\partial X_2} \frac{\partial u_1}{\partial X_3} + \frac{\partial u_2}{\partial X_2} \frac{\partial u_2}{\partial X_3} + \frac{\partial u_3}{\partial X_2} \frac{\partial u_3}{\partial X_3} \right) \end{aligned}$$

3.2.2 Stress Tensors

Having defined the strain tensor, now the next step is the individuation of the stress one: as equations of equilibrium are derived it is possible to introduce multiple stress measurements.

The first stress to be introduced is the *true stress* or *Cauchy stress* tensor, i.e. the stress of the deformed configuration. Calling $d\mathbf{f}(\hat{\mathbf{n}})$ the force acting in the infinitesimal area $\hat{\mathbf{n}}da = d\mathbf{a}$ of the deformed configuration at position \mathbf{x} , the stress vector is defined as

$$\mathbf{t}(\hat{\mathbf{n}}) = \frac{d\mathbf{f}}{da} \quad (3.9)$$

The Cauchy stress tensor is then determined as the force per unit deformed area

$$d\mathbf{f} = da \cdot \boldsymbol{\sigma} \quad \implies \quad \mathbf{t} = \boldsymbol{\sigma} \cdot \hat{\mathbf{n}} \quad (3.10)$$

As the deformed configuration is unknown, reason why it is useful to adopt the Lagrangian description, a new stress \mathbf{P} is introduced to relate the force with the undeformed area $d\mathbf{A}$

$$d\mathbf{f} = d\mathbf{A} \cdot \mathbf{P} \quad (3.11)$$

where $d\mathbf{A} = dA \cdot \hat{\mathbf{N}}$ and $\hat{\mathbf{N}}$ is the unit normal to the undeformed area. Moreover, \mathbf{P} is called the *first Piola-Kirchhoff stress tensor* and it is not symmetric.

Referring to equation (3.2) it is possible to express the distance of the points in the reference configuration as

$$d\mathbf{X} = \mathbf{F}^{-1} d\mathbf{x}$$

and in a very similar fashion, the force $d\mathbf{f}$, acting on the deformed area, can be transformed into the one acting on the undeformed area $d\mathbf{A}$

$$d\mathbf{F} = \mathbf{F}^{-1} \cdot d\mathbf{f} = \mathbf{F}^{-1} (d\mathbf{A} \cdot \mathbf{P}) = d\mathbf{A} \cdot \mathbf{P} \cdot \mathbf{F}^{-T} \equiv d\mathbf{A} \cdot \mathbf{S} \quad (3.12)$$

which allows to obtain the *second Piola-Kirchhoff stress tensor* \mathbf{S} : this is the tensor used in the Lagrangian formulation of geometrically nonlinear analysis. Thus, the second Piola-Kirchhoff stress tensor gives the transformed current force per unit undeformed area. Note also that this tensor is symmetric whenever the Cauchy one is. [22]

Here, it might be useful to summarize the relationship between the tensors obtained so far:

$$\mathbf{P} = J\mathbf{F}^{-1} \cdot \boldsymbol{\sigma} = \mathbf{S} \cdot \mathbf{F}^T \quad (3.13)$$

$$\mathbf{S} = J\mathbf{F}^{-1} \boldsymbol{\sigma} \mathbf{F}^{-T} \quad (3.14)$$

where J is the determinant of \mathbf{F} .

On an end note it may be worth to mention that many FEM codes use the Piola-Kirchhoff tensors internally, but then return the Cauchy true stress as the formers are projected into the latter, e.g. [see 25, p. 101]

3.3 Isoparametric Element

When any domain is divided into several smaller elements, the latter can take on the most disparate shapes to adequately discretize the geometry of the former. Therefore, in order to treat in a univocal and simple way the various elements of complex and different shapes, a reference element must be introduced, having a simpler shape, defined in a system of natural and adimensional coordinates. In this way a biunivocal relationship is established between the cartesian system (x, y, z) and the natural one (ξ, η, ζ) , with $-1 \leq \xi, \eta, \zeta \leq 1$: thus, the element in the physical system is described by the projection of the reference element in the cartesian coordinate system from the natural one

$$x = \sum_{i=1}^n n_i(\xi, \eta, \zeta) x_i \quad y = \sum_{i=1}^n n_i(\xi, \eta, \zeta) y_i \quad z = \sum_{i=1}^n n_i(\xi, \eta, \zeta) z_i \quad (3.15)$$

where x_i, y_i, z_i are the cartesian coordinates of the n nodes of the element. Instead, the *shape functions*, defined in the natural system, are labelled as n_i . These are as many as the number of nodes of the element.

Before diving into the description of the quadratic tetra element, it is good to underline the properties that the shape functions must satisfy: [23]

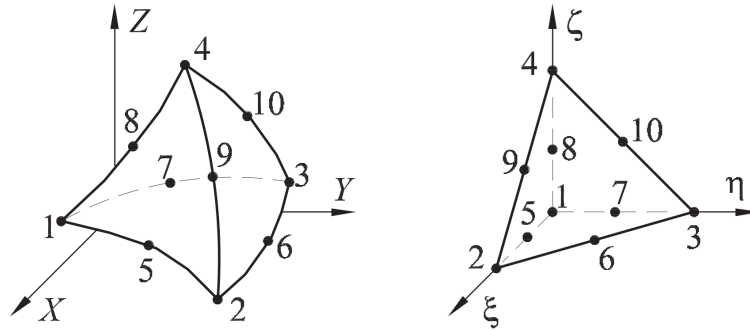


Figure 3.3: Quadratic Tetra Element Representation, [24]

- Be a continuous and isotropic function as the material itself is continuous and isotropic, i.e. not dependent on the reference frame;
- Be differentiable with respect to the spatial coordinate up to the required order so that both strains and stresses can be computed;
- Able to describe the rigid motion, leading to a vanishing elastic potential energy;
- Describe a constant strain field if the overall deformation of the element dictates so;
- Determine a deformed shape of each element that matches the shape of the neighbouring elements.

If the first four conditions are met then the shape functions are said to be *complete*, if the last requirement is satisfied the shape functions are *compatible*. If a shape function is both complete and compatible then it is said to be **conform**.

3.3.1 Quadratic Triangular Element

Similarly to what has been done for coordinates, displacements can also be expressed starting from nodal ones: this approach is called *displacement based formulation*.

$$u = \sum_{i=1}^m n_i(\xi, \eta, \zeta) u_i \quad v = \sum_{i=1}^m n_i(\xi, \eta, \zeta) v_i \quad w = \sum_{i=1}^m n_i(\xi, \eta, \zeta) w_i \quad (3.16)$$

Note that the shape functions are not necessarily the same of equation (3.15): in fact the index of the sum is m instead of n . However, for an isoparametric element, the two coincides and therefore the shape functions are the same too.

The equations are usually expressed in matrix form

$$\mathbf{u} = [n] \mathbf{q} \quad (3.17)$$

where \mathbf{q} is the vector of nodal displacements and $[n]$ the matrix containing the shape functions.

The choice of the shape functions, used for interpolation, falls on polynomials defined in the natural system: this is an hypothesis as it constraints the possibility of displacements distribution. For the quadratic tetra element the followings are used [24]

$$\begin{aligned} n_1 &= (1 - \xi - \eta - \zeta) [2(1 - \xi - \eta - \zeta) - 1] \\ n_2 &= \xi(2\xi - 1) \\ n_3 &= \eta(2\eta - 1) \\ n_4 &= \zeta(2\zeta - 1) \\ n_5 &= 4\xi(1 - \xi - \eta - \zeta) \\ n_6 &= 4\xi\eta \\ n_7 &= 4\eta(1 - \xi - \eta - \zeta) \\ n_8 &= 4\zeta(1 - \xi - \eta - \zeta) \\ n_9 &= 4\xi\zeta \\ n_{10} &= 4\eta\zeta \end{aligned}$$

Thus the shape functions matrix is assembled as

$$[n] = \begin{bmatrix} n_1 & 0 & 0 & \dots & n_i & 0 & 0 & \dots & n_{10} & 0 & 0 \\ 0 & n_1 & 0 & \dots & 0 & n_i & 0 & \dots & 0 & n_{10} & 0 \\ 0 & 0 & n_1 & \dots & 0 & 0 & n_i & \dots & 0 & 0 & n_{10} \end{bmatrix}$$

Having determined the displacements, it is possible to compute the strains

$$[\varepsilon] = [\partial] \mathbf{u} \implies [\varepsilon] = [\partial] [n] \mathbf{q} \quad (3.18)$$

where $[B] = [\partial] [n]$ is the strain matrix, whose components for the i -th shape function of the quadratic tetra element look like

$$[B_i] = \begin{bmatrix} \partial n_i / \partial x & 0 & 0 \\ 0 & \partial n_i / \partial y & 0 \\ 0 & 0 & \partial n_i / \partial z \\ \partial n_i / \partial y & \partial n_i / \partial x & 0 \\ 0 & \partial n_i / \partial z & \partial n_i / \partial y \\ \partial n_i / \partial z & 0 & \partial n_i / \partial x \end{bmatrix} \quad (3.19)$$

However, equation (3.19) poses the problem of how to differentiate with respect to the physics coordinate the shape functions defined in natural ones. This is done

by computing the so called *Jacobian matrix*

$$[J] = \begin{bmatrix} \frac{\partial x}{\partial \xi} & \frac{\partial y}{\partial \xi} & \frac{\partial z}{\partial \xi} \\ \frac{\partial x}{\partial \eta} & \frac{\partial y}{\partial \eta} & \frac{\partial z}{\partial \eta} \\ \frac{\partial x}{\partial \zeta} & \frac{\partial y}{\partial \zeta} & \frac{\partial z}{\partial \zeta} \end{bmatrix} \quad (3.20)$$

that allows to compute the derivative of the shape functions with respect to the spatial coordinates

$$\begin{Bmatrix} \frac{\partial n_i}{\partial x} \\ \frac{\partial n_i}{\partial y} \\ \frac{\partial n_i}{\partial z} \end{Bmatrix} = [J]^{-1} \begin{Bmatrix} \frac{\partial n_i}{\partial \xi} \\ \frac{\partial n_i}{\partial \eta} \\ \frac{\partial n_i}{\partial \zeta} \end{Bmatrix} \quad (3.21)$$

As for the components of the Jacobian, they are easily computed as

$$\begin{aligned} \frac{\partial x}{\partial \xi} &= \sum_{i=1}^n \frac{\partial n_i}{\partial \xi} x_i & \frac{\partial y}{\partial \xi} &= \sum_{i=1}^n \frac{\partial n_i}{\partial \xi} y_i & \frac{\partial z}{\partial \xi} &= \sum_{i=1}^n \frac{\partial n_i}{\partial \xi} z_i \\ \frac{\partial x}{\partial \eta} &= \sum_{i=1}^n \frac{\partial n_i}{\partial \eta} x_i & \frac{\partial y}{\partial \eta} &= \sum_{i=1}^n \frac{\partial n_i}{\partial \eta} y_i & \frac{\partial z}{\partial \eta} &= \sum_{i=1}^n \frac{\partial n_i}{\partial \eta} z_i \\ \frac{\partial x}{\partial \zeta} &= \sum_{i=1}^n \frac{\partial n_i}{\partial \zeta} x_i & \frac{\partial y}{\partial \zeta} &= \sum_{i=1}^n \frac{\partial n_i}{\partial \zeta} y_i & \frac{\partial z}{\partial \zeta} &= \sum_{i=1}^n \frac{\partial n_i}{\partial \zeta} z_i \end{aligned}$$

But perhaps what is even more important is the fact that the Jacobian allows the passage from one system to the other

$$dV = dx dy dz = \det(J) d\xi d\eta d\zeta \quad (3.22)$$

and that its determinant can give an important indication on the distortion of the element in the physical reference frame, reason why is often used as a *quality check* parameter of the mesh.

The next step is the computation of the stiffness and mass matrices as well as the excitation: the procedure treated follows the variational approach based on the Lagrange equation.

$$\frac{d}{dt} \left(\frac{\partial \mathcal{L}}{\partial \dot{\mathbf{q}}} \right) - \frac{\partial \mathcal{L}}{\partial \mathbf{q}} = \mathcal{Q} \quad (3.23)$$

where \mathcal{L} is the difference between the kinetic and potential energy, while \mathcal{Q} are the generalized forces acting on the system. Expressing the kinetic energy as

$$\mathcal{T} = \frac{1}{2} \int_V \dot{\mathbf{u}}^T \rho \dot{\mathbf{u}} dV$$

then, referring to equation (3.17), the kinetic energy can be written also as

$$\mathcal{T} = \frac{1}{2} \dot{\mathbf{q}}^T \left[\int_V [n]^T \rho [n] dV \right] \dot{\mathbf{q}} \quad (3.24)$$

with $\dot{\mathbf{q}}$ outside of the integral as the nodal displacements do not depend on the reference frame chosen.

The generalized forces acting on the system are the external ones, in this case only volume forces are taken into account:

$$\mathcal{Q} = \int_V [n]^T \{f\}_V(x, y, z, t) dV \quad (3.25)$$

Meanwhile, with the elastic energy

$$d\mathcal{U} = \int_V \{\sigma\}^T d\{\varepsilon\}$$

pre-stresses and pre-strains are taken into account through the material constitutive law:

$$\{\varepsilon\} = [B] \mathbf{q} \quad (3.26)$$

$$\{\sigma\} = [E] (\{\varepsilon\} - \{\varepsilon\}_0) + \{\sigma_0\} \quad (3.27)$$

where $[E]$ is the linear elastic matrix, containing material properties.

By substituting them in the expression of the infinitesimal potential energy the following is obtained:

$$d\mathcal{U} = \{\sigma_0\}^T \{\varepsilon\} + \frac{1}{2} \{\varepsilon\}^T [E] \{\varepsilon\} - \{\varepsilon_0\}^T [E] \{\varepsilon\} \quad (3.28)$$

which allows to express the potential energy in the system

$$\begin{aligned} \mathcal{U} &= \int_V d\mathcal{U} dV \\ &= \int_V \{\sigma_0\}^T \{\varepsilon\} dV + \frac{1}{2} \int_V \{\varepsilon\}^T [E] \{\varepsilon\} dV - \int_V \{\varepsilon_0\}^T [E] \{\varepsilon\} dV \end{aligned}$$

Moreover it is possible to link it to the nodal displacements, as done for the kinetic energy and the generalized forces

$$\mathcal{U} = \left[\int_V \{\sigma_0\}^T [B] dV \right] \mathbf{q} + \frac{1}{2} \mathbf{q}^T \left[\int_V [n]^T [E] [n] dV \right] \mathbf{q} - \left[\int_V \{\varepsilon_0\}^T [E] [B] dV \right] \mathbf{q} \quad (3.29)$$

Finally, by computing the differentiation with respect to the nodal values, as per equation (3.23), the following matrices are obtained:

$$\mathbf{K} = \int_V [n]^T [E] [n] dV = \int_{-1}^1 \int_{-1}^1 \int_{-1}^1 [n]^T [E] [n] d\xi d\eta d\zeta \quad (3.30)$$

$$\mathbf{M} = \int_V [n]^T \rho [n] dV = \int_{-1}^1 \int_{-1}^1 \int_{-1}^1 [n]^T \rho [n] d\xi d\eta d\zeta \quad (3.31)$$

$$\mathbf{f} = \int_V [n]^T \{f\}_V dV + \int_V \{\varepsilon_0\}^T [E] [B] dV - \int_V \{\sigma_0\}^T [B] dV \quad (3.32)$$

Note that the damping matrix has been neglected as its introduction heavily depends on the assumptions made on how the system is damped. A simple, but popular, hypothesis is to have a damping matrix obtained by linear combination of mass and stiffness matrices.

Moreover, the integral is not computed analytically as it would prove both difficult and not useful when trying to extend such formulation to a variety of elements: therefore a numerical integration scheme, such as *Gauss' quadrature method*, is used

$$\mathbf{K} = \sum_{i=1}^{m_i} \sum_{j=1}^{m_j} \sum_{k=1}^{m_k} \psi_i \psi_j \psi_k [B]_{ijk}^T [E]_{ijk} [B]_{ijk} \quad (3.33)$$

This shows even further how important the determinant of the Jacobian is: in fact, if equal to zero, it will lead to a *singular* stiffness matrix.

Finally stress and strains are computed thanks to material constitutive law, already expressed by equation (3.26) and (3.27).

3.4 Building the Campbell Diagram

Having understood how the matrices and vectors of the physical problem are created from the mesh of the geometric model, it is fair to ask what analyses have to be carried out and subsequently how the Campbell diagram is to be constructed.

First of all, a static analysis is carried out to assess the average stress level acting on the structure.

$$\mathbf{K}\mathbf{x} = \mathbf{F}$$

Usually the most significant load, albeit not the only one, is the centrifugal load: the force per unit of volume can be defined as [25]

$$f_V = \rho\Omega^2$$

where Ω is the rotational speed and ρ is the material density.

The eigenproblem is obtained by formulating a perturbation problem, i.e. the physical properties are updated following the results of the previous static step, thus taking into account the rotational speed effect on the modal analysis.

$$\mathbf{K}\phi = \lambda\mathbf{M}\phi \quad (3.34)$$

where $\lambda = \omega^2$ is the eigenvalue and ϕ is the eigenvector.

Strategies for solving the eigenproblem can be found in the literature: in fact, methods are used to avoid the inversion of large matrices because of the high computational cost that this operation would require. [see 26, 27]

So by repeating the same procedure for multiple speeds in the operating range, it is possible to construct the Campbell diagram: in fact it will be sufficient to associate each eigenvalue with the speed of the centrifugal load and then connect the eigenvalues corresponding to the same mode shape.

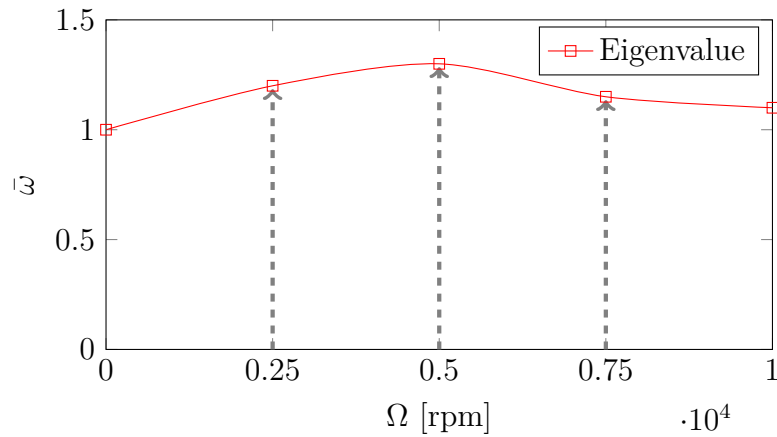


Figure 3.4: Campbell diagram for a single mode shape

Given the properties of a cyclic symmetric structure, the Campbell Diagram will look like the one shown in Figure 2.11. Moreover, it is possible to identify and show the true resonances in the so called SAFE diagram, by remembering the relationship between ND and EO highlighted in Table 2.1.

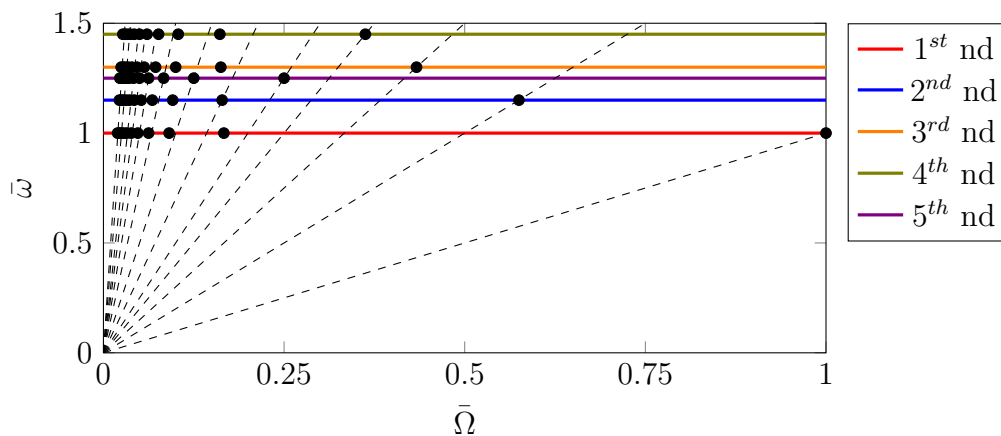


Figure 3.5: SAFE diagram of a single mode shape

In this chapter we have first seen how a continuous body can be discretized into a *finite* number of degrees of freedom: the physical properties of the body are obtained by choosing *shape functions* that approximate the distribution of unknown quantities in the subdomains into which the body has been divided. In addition, it has also been shown how the constitutive laws of the material are declined in the finite element model, thus allowing to compute strains and stresses.

An example has been provided in order to show how the finite element method is applied and how the mass and stiffness matrices of a quadratic triangular element are computed.

Finally, the procedure followed to reproduce the diagrams necessary to determine the dynamic behaviour of the bladed disc was also shown: in fact by performing the prestressed modal analysis it is possible to identify the resonances, i.e. the potential causes of HCF failure. Therefore, in the following chapters, the problem of how the forced response of the system can be studied will be addressed.

Chapter 4

Harmonic Balance Method

The harmonic balance is a widely used method to compute the steady-state response of nonlinear differential equations: instead of computing the time domain steady-state response, the harmonic balance technique is a frequency domain method. Its applications extend to many engineering fields such as: fluid-dynamics, structures, electrical circuits and dynamics of mechanical systems. This method allows to compute the periodic solution and, for this reason, it is well suited to solve differential equations with periodic time dependence such as the dynamic problem of rotating machinery.

The core concept is to provide a formulation of the approximate periodic solution in the form of a truncated Fourier series and carry on the study of the oscillation in the frequency domain where the unknowns are the Fourier coefficients. The number of unknowns depends linearly on both the number of the harmonics chosen and the number of degrees of freedom of the studied system. In order to get the value of the coefficients the equations are transformed into an algebraic set and then multiple solutions techniques can be applied.

In this chapter an overview of the harmonic balance method will be provided: starting by the simple example of the duffing oscillator, with only one dof, before showing its application to a multi-degrees of freedom system.

4.1 Duffing Oscillator

A simple case of nonlinear mechanical system is the Duffing oscillator: a one degree of freedom system where the nonlinearities are induced by a cubic spring.

The equation of motion for the system represented in Figure 4.1 is

$$m\ddot{x} + c\dot{x} + kx + \gamma x^3 = P \cos(\Omega t) \quad (4.1)$$

whereas the goal is to find the periodic solution

$$x(t) = x(t + T) \quad \text{where } T = \frac{2\pi}{\Omega}$$

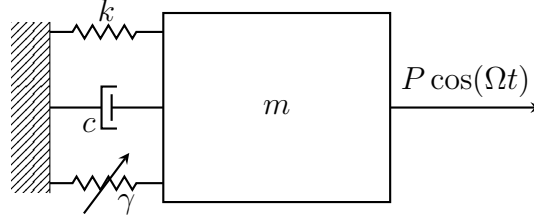


Figure 4.1: Duffing Oscillator

The harmonic balance method consist of approximating the periodic solution with a Fourier series

$$x \approx x_h(t) = \tilde{x}_0 + \sum_{i=1}^{\infty} \tilde{x}_{c,i} \cos(\Omega t) + \tilde{x}_{s,i} \sin(\Omega t) \quad (4.2)$$

and then make an assumption on the number of harmonics that should be retained to approximate the solution, which in this particular case is only the 1st harmonic

$$\begin{aligned} x_h &= \tilde{x}_c \cos(\Omega t) + \tilde{x}_s \sin(\Omega t) \\ \dot{x}_h &= -\Omega \tilde{x}_c \sin(\Omega t) + \Omega \tilde{x}_s \cos(\Omega t) \\ \ddot{x}_h &= -\Omega^2 \tilde{x}_c \cos(\Omega t) - \Omega^2 \tilde{x}_s \sin(\Omega t) \end{aligned} \quad (4.3)$$

By expanding the cubic term, it is possible to notice the surge of other harmonic components, as shown in [28]

$$\begin{aligned} x_h^3 &= (\tilde{x}_c \cos(\Omega t) + \tilde{x}_s \sin(\Omega t))^3 \\ &= \dots = \\ &= \frac{3}{4}(\tilde{x}_c^3 + \tilde{x}_c \tilde{x}_s^2) \cos(\Omega t) + \frac{3}{4}(\tilde{x}_s^3 + \tilde{x}_s \tilde{x}_c^2) \sin(\Omega t) + \dots \end{aligned}$$

but having decided to approximate the response using only the first harmonic, these new components have to be neglected in the new system equation of motion

$$\begin{aligned} &\left[(k - \Omega^2 m) \tilde{x}_c + c \Omega \tilde{x}_s + \frac{3}{4} \gamma (\tilde{x}_c^3 + \tilde{x}_c \tilde{x}_s^2) - P \right] \cos(\Omega t) + \\ &+ \left[(k - \Omega^2 m) \tilde{x}_s + c \Omega \tilde{x}_c + \frac{3}{4} \gamma (\tilde{x}_s^3 + \tilde{x}_s \tilde{x}_c^2) \right] \sin(\Omega t) = 0 \end{aligned} \quad (4.4)$$

Balancing the cosine and sine coefficients separately, as the solution has to be verified $\forall t$, a new set of algebraic equation is obtained

$$\begin{cases} (k - \Omega^2 m) \tilde{x}_c + c \Omega \tilde{x}_s + \frac{3}{4} \gamma (\tilde{x}_c^3 + \tilde{x}_c \tilde{x}_s^2) - P = 0 \\ (k - \Omega^2 m) \tilde{x}_s + c \Omega \tilde{x}_c + \frac{3}{4} \gamma (\tilde{x}_s^3 + \tilde{x}_s \tilde{x}_c^2) = 0 \end{cases} \quad (4.5)$$

This simple example is helpful because it shows where the nonlinearities lie and how they affect the system: although the forcing is exciting the system at the frequency Ω , new harmonic components are generated by that, thus determining the nonlinearities in the response. Multiple of the forcing frequency are called *super-harmonic*, while denominators are called *sub-harmonic*.

Moreover it is important to note that as the *superposition principle is no longer valid*, studying the dynamic uncoupled by the static solution may yield a bad approximation as the initial condition in the nonlinear case may heavily affect the solution.

4.2 Multi-Degrees of Freedom Systems

The harmonic balance method it is not limited to SDOF model only: in fact it can be generalized to MDOF model as well. [1, 28] The generic equation of motion of such system can be written as

$$\mathbf{M}\ddot{\mathbf{x}}(t) + \mathbf{C}\dot{\mathbf{x}}(t) + \mathbf{K}\mathbf{x}(t) = \mathbf{f}_{ext}(t) - \mathbf{f}_{nl}(\dot{\mathbf{x}}(t), \mathbf{x}(t), t) \quad (4.6)$$

The vector \mathbf{f}_{ext} and \mathbf{f}_{nl} represent the external and nonlinear forces respectively; \mathbf{M} and \mathbf{K} are the mass and stiffness matrices, the former is symmetric and definite positive while the latter is only semi-definite positive as it takes into account rigid body motion too.

Since the periodic solution is being sought, it is possible to write it as a Fourier series.

$$\mathbf{x}_h(t) = \tilde{\mathbf{x}}_0 + \sum_{k=0}^{\infty} \tilde{\mathbf{x}}_{c,k} \cos(\Omega t) + \tilde{\mathbf{x}}_{s,k} \sin(\Omega t) = \Re \left\{ \sum_{k=0}^{\infty} \tilde{\mathbf{x}}_k e^{ik\Omega t} \right\},$$

A further assumption is made on the number of harmonics retained: in [1] a general overview on the common practices for harmonics choice can be found, while Grolet et al. [29] have proposed a method where the harmonics are selected or neglected based on their predicted associated energy. It is important to note that, even considering an infinite number of harmonics, the periodic solution $\mathbf{x}_h(t)$ is only an approximation of the exact solution $\mathbf{x}(t)$.

$$\begin{aligned} \mathbf{x}_h &= \Re \left\{ \sum_{k=0}^H \tilde{\mathbf{x}}_k e^{ik\Omega t} \right\} \\ \dot{\mathbf{x}}_h &= \Re \left\{ \sum_{k=0}^H ik\Omega \tilde{\mathbf{x}}_k e^{ik\Omega t} \right\} \\ \ddot{\mathbf{x}}_h &= \Re \left\{ \sum_{k=0}^H -(k\Omega)^2 \tilde{\mathbf{x}}_k e^{ik\Omega t} \right\} \end{aligned} \quad (4.7)$$

By substituting them in the equation of motion (4.6), the following is obtained

$$\Re \left\{ \sum_{k=0}^H \left([\mathbf{K} - (k\Omega)^2 \mathbf{M} + ik\Omega \mathbf{C}] \tilde{\mathbf{x}}_k + \tilde{\mathbf{f}}_{nl,k} - \tilde{\mathbf{f}}_k \right) e^{ik\Omega t} \right\} = \mathbf{r} \quad (4.8)$$

where \mathbf{r} is the residue, i.e. the error associated to the approximated solution. Often the dynamic equilibrium of the forces is indicated by

$$\mathbf{R}_k = [\mathbf{K} - (k\Omega)^2 \mathbf{M} + ik\Omega \mathbf{C}] \tilde{\mathbf{x}}_k + \tilde{\mathbf{f}}_{nl,k} - \tilde{\mathbf{f}}_k \quad (4.9)$$

Moreover the external forces contribution is computed as

$$\mathbf{f}_{ext} = \Re \left\{ \sum_{k=0}^H \tilde{\mathbf{f}}_k e^{ik\Omega t} \right\} \quad (4.10)$$

while the nonlinear forces coefficients represent the true challenge: the formal definition is

$$\frac{1}{\pi} \int_0^{2\pi} \mathbf{f}_{nl}(\mathbf{x}, \dot{\mathbf{x}}) e^{-ik\Omega t} d\Omega t = \begin{cases} 2\mathbf{f}_{nl,0} \\ \mathbf{f}_{nl,k} \quad k = 1, \dots, H \end{cases} \quad (4.11)$$

but given the huge variety of possibilities, the so called Alternating-Frequency-Time (AFT) scheme is used for determining those coefficients, where the Fast Fourier Transform algorithm is used to compute the discrete Fourier transform.

$$\tilde{\mathbf{f}}_{nl,k} = FFT[\mathbf{f}_{nl}(iFFT[\mathbf{x}_k], iFFT[ik\Omega \mathbf{x}_k])] \quad (4.12)$$

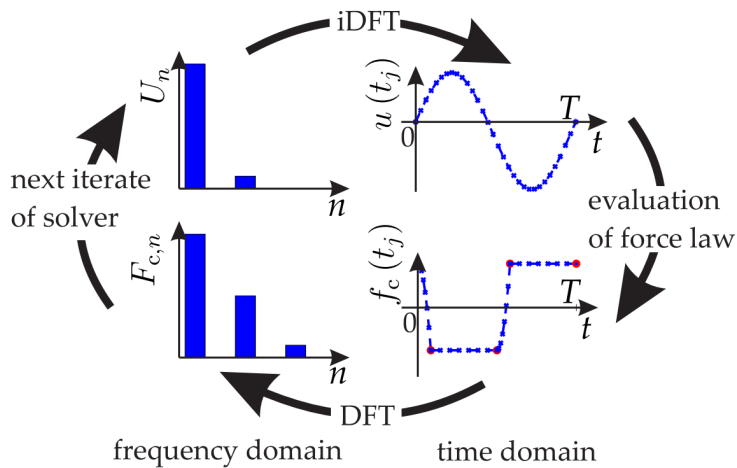


Figure 4.2: AFT algorithm scheme, [1]

The FFT allows to convert the signal from the time domain to the frequency domain, while the iFFT (inverse Fast Fourier Transform) does the opposite. The number of samples per period is determined according to the Nyquist-Shannon theorem: the number of points used must be large enough to solve the highest harmonics, guaranteeing the convergence of HBM.

The next step now is to find a way to solve the equation (4.8): naturally the goal is to have a null error. The weighted residual method can be used here

$$\int_0^T \mathbf{r}(\mathbf{x}_h, \dot{\mathbf{x}}_h) \psi_k dt = 0 \quad k = 0, 1, \dots, H$$

and if the weighted function is selected from one of the functions used to approximate the solution, then the method is of the Galerkin type. In particular the choice falls on the function $\psi_k = e^{-ik\Omega t}$, thus obtaining

$$\begin{aligned} \int_0^T \mathbf{r}(\mathbf{x}_h, \dot{\mathbf{x}}_h) e^{-ik\Omega t} dt &= 0 \\ \int_0^T \Re \left\{ \sum_{l=0}^H \mathbf{R}_l e^{il\Omega t} \right\} e^{-ik\Omega t} dt &= 0 \\ \int_0^{2\pi} \Re \left\{ \sum_{l=0}^H \mathbf{R}_l e^{il\tau} \right\} e^{-ik\tau} d\tau &= 0 \end{aligned}$$

this integral yields nonzero values only when $l = k$, thus the residue is null only if the dynamic equilibrium is verified

$$\mathbf{R}_k = 0 \quad (4.13)$$

which translates to the following new set of equations

$$\begin{cases} \mathbf{R}_0(\tilde{\mathbf{x}}_0, \dots, \tilde{\mathbf{x}}_H) = 0 \\ \dots \\ \mathbf{R}_H(\tilde{\mathbf{x}}_0, \dots, \tilde{\mathbf{x}}_H) = 0 \end{cases}$$

This set of $H + 1$ complex equations can be transformed into an algebraic one of $2H + 1$ real equations, obtained by using the sine and cosine notation instead of the complex numbers. This means that in order to find the periodic solution of a system made up by N -dofs, a set of equations containing $N \cdot (2H + 1)$ unknowns has to be solved. For this very reason a reduced order model, instead of the full one, is used.

A common technique to solve equation (4.13) is the Newton-Raphson method: the idea is to perform a linearisation of the residual using a Taylor series at step $\mathbf{x}^{(j)}$ to compute the next step $\mathbf{x}^{(j+1)}$, iterating until $\|\mathbf{R}\| \leq \text{err}$ [28]

$$\begin{cases} \mathbf{x}^{(j+1)} = \mathbf{x}^{(j)} - \frac{\partial \mathbf{R}}{\partial \mathbf{x}} \Big|_{\mathbf{x}^{(j)}} \mathbf{R}(\mathbf{x}^{(j)}) & \text{iteration step} \\ \mathbf{R}(\mathbf{x}^{(j+1)}) \approx \mathbf{R}(\mathbf{x}^{(j)}) + \frac{\partial \mathbf{R}}{\partial \mathbf{x}} \Big|_{\mathbf{x}^{(j)}} (\mathbf{x}^{(j+1)} - \mathbf{x}^{(j)}) = \mathbf{0} & \text{residual linearisation} \end{cases} \quad (4.14)$$

However, when studying the response over a frequency range, this method always causes difficulty in convergence at resonance frequency points or even fail at turning points and bifurcation points. In order to enhance the stability of the nonlinear solver, it is of interest to trace the loci of the solutions by introducing a continuation parameter λ . [30]

$$\mathbf{R}(\lambda, \mathbf{x}) = 0$$

A predictor-corrector technique is used with the variation of parameter λ : first a prediction of the response at the next frequency is performed to speed up the iterative convergence, usually such estimation is based on the gradient computed at the current converged point. Then a second step is performed iteratively until the desired accuracy is obtained.

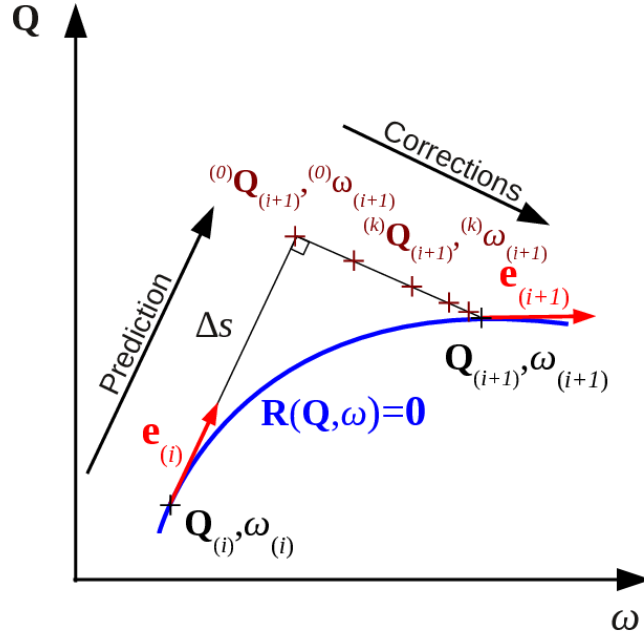


Figure 4.3: Continuation Algorithm: Rik's method, [31]

The main features of this method is the computational efficiency as it avoids the time-consuming computation of the physical transient and it usually requires a low number of harmonics to capture the behaviour accurately. Moreover it allows to compute unstable oscillations. Meanwhile the main limitations are certainly the fact that its application is limited to periodic solutions, as well as the Gibbs phenomenon, see Figure 4.5, near discontinuities such as impacts and stick-slip transition: the cause is intrinsic to the choice of using a finite number of harmonic functions to approximate the response.

In summary, the Harmonic Balance is an efficient numerical method for the computation of periodic solutions of nonlinear ODEs: it yields, similarly to Galerkin's

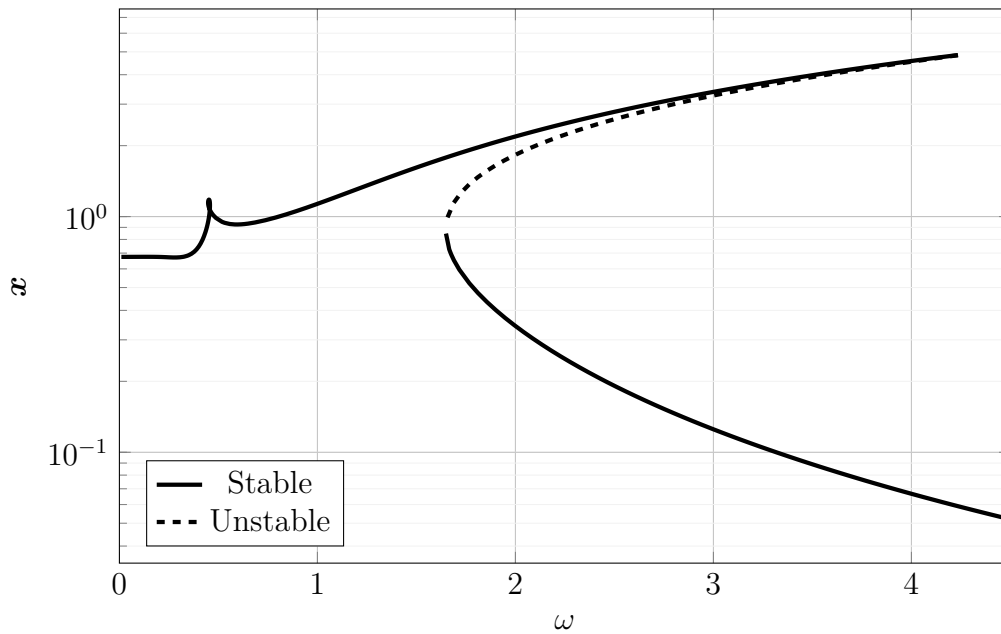


Figure 4.4: Stability of the oscillation

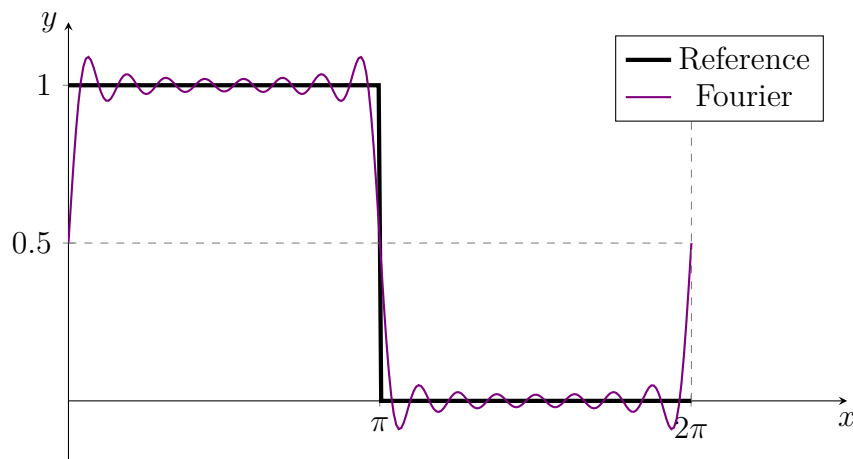


Figure 4.5: Gibbs phenomenon

method, an algebraic equation system in the frequency domain. However, due to the expansion of the problem into several harmonic components, the number of degrees of freedom increases considerably, which is why a reduced order model is preferred to complex models. Therefore, in the next chapter an overview of the most common model order reduction techniques will be given.

Chapter 5

Model Order Reduction

With time and the spread of finite element analysis, the size of models has kept growing, but at the same time the computing power and efficiency of software has also increased. However, interest has also increasingly shifted to nonlinear problems, for example the continuous optimisation of structures and weight reduction in the aerospace industry has required the use of a formulation that includes geometric nonlinearities.

When dealing with a non-linear problem, though, the computational cost of analysing the whole structure is simply too high: for this reason, a reduced order model is used, i.e. one with fewer degrees of freedom, which is nevertheless accurate enough to faithfully represent the behaviour of the structure. By reducing the dofs, the size of the set of equations that need to be solved is decreased so that a good compromise between accuracy and time efficiency is reached. In literature many Model Order Reduction (MOR) techniques, for linear mechanical system, have been introduced: two common approaches are either to estimate the frequency response function matrix or, as in the so called component mode synthesis (CMS) methods, to introduce an expression for the eliminated DOFs through retained DOFs, usually using mode shapes obtained with specific boundary conditions. [32]

In this project, the need for a reduced order model is mostly due to the use of the harmonic balance method: in fact, given a problem made up by N degrees of freedom, the size of the forced response problem with the HBM is

$$\begin{cases} 2H \cdot N & \text{if harminc 0 is not used} \\ [2(H - 1) + 1] \cdot N & \text{if harminc 0 is used} \end{cases}$$

where H is the number of harmonics used. As a coarse model of turbine sector can easily have more than 10^5 DOFs and may require even more than 5 harmonics, it is pretty easy to understand that there is a whole order of magnitude between a modal analysis and a forced response, with the latter being an iterative intensive process, as shown in Figure 4.2 & 4.3.

5.1 Component Mode Synthesis Methods

Given a dynamic problem of the type

$$\mathbf{M}\ddot{\mathbf{x}} + \mathbf{C}\dot{\mathbf{x}} + \mathbf{K}\mathbf{x} = \mathbf{f} \quad (5.1)$$

where \mathbf{M} is the mass matrix, \mathbf{C} the damping matrix, \mathbf{K} the stiffness matrix and \mathbf{f} is the external force vector.

The steps of a generic CMS method to build the reduced order model are:

1. Introduce a subspace \mathbf{V}
2. Apply the modal transformation $\mathbf{x} = \mathbf{V}\mathbf{q}$
3. Pre-multiply the governing equation by \mathbf{V}^T , the transpose of subspace \mathbf{V} , obtaining the following expressions

$$\begin{aligned} \mathbf{V}^T \mathbf{M} \mathbf{V} \ddot{\mathbf{q}} + \mathbf{V}^T \mathbf{C} \mathbf{V} \dot{\mathbf{q}} + \mathbf{V}^T \mathbf{K} \mathbf{V} \mathbf{q} &= \mathbf{V}^T \mathbf{f} \\ \mathbf{M}^* \ddot{\mathbf{q}} + \mathbf{C}^* \dot{\mathbf{q}} + \mathbf{K}^* \mathbf{q} &= \mathbf{f}^* \end{aligned} \quad (5.2)$$

It is evident how critical the choice of the subspace \mathbf{V} is: in fact it must be able to properly describe the dynamic behaviour of the model, while having a limited size in order to reduce the computational cost of the problem.

5.1.1 Modal Truncation

One of the simplest reduction techniques is certainly the modal truncation: it consists in describing the response of a **linear system** as the *linear superposition* of its mode shapes. Those are obtained by the eigenvalue problem

$$(\mathbf{K} - \omega_i^2 \mathbf{M})\boldsymbol{\phi}_i = \mathbf{0} \quad (5.3)$$

where ω_i is the i -th eigenvalue and $\boldsymbol{\phi}_i$ is the corresponding i -th eigenvector. It is then possible to build the matrix $\boldsymbol{\Phi}$, where each i -th column corresponds to the i -th eigenvector $\boldsymbol{\phi}_i$.

Then a change in the system of coordinates is performed, passing from the spatial to the modal ones

$$\mathbf{x} = \boldsymbol{\Phi}\mathbf{q} \quad (5.4)$$

This means selecting the eigenvector matrix $\boldsymbol{\Phi}$ as the subspace \mathbf{V} which lead to the following description of the dynamic behaviour of the system

$$\boldsymbol{\Phi}^T \mathbf{M} \boldsymbol{\Phi} \ddot{\mathbf{q}} + \boldsymbol{\Phi}^T \mathbf{C} \boldsymbol{\Phi} \dot{\mathbf{q}} + \boldsymbol{\Phi}^T \mathbf{K} \boldsymbol{\Phi} \mathbf{q} = \boldsymbol{\Phi}^T \mathbf{f} \quad (5.5)$$

Now it is important to remember two fundamental properties:

- The eigenvectors are \mathbf{M} -orthogonal and \mathbf{K} -orthogonal;
- The solution of the eigenproblem is not unique, meaning that the mode shape, corresponding to a specific natural frequency, act as a basis of a space made up by all the possible eigenvectors for said frequency.

This is helpful as it allows to simplify equation (5.5): in fact by normalising the eigenvector with respect to the mass matrix and by assuming a proportional damping, as the Rayleigh one $\mathbf{C} = \alpha\mathbf{M} + \beta\mathbf{K}$, the new matrices become

$$\begin{cases} \Phi^T \mathbf{M} \Phi = \mathbf{I} \\ \Phi^T \mathbf{K} \Phi = \Lambda^2 = \text{diag}(\omega_1^2, \dots, \omega_N^2) \\ \Phi^T \mathbf{C} \Phi = 2 \cdot \text{diag}(\zeta\omega) \end{cases} \quad (5.6)$$

obtaining a simplified dynamic equation

$$\mathbf{I}\ddot{\mathbf{q}} + 2 \cdot \text{diag}(\zeta\omega) \dot{\mathbf{q}} + \Lambda^2 \mathbf{q} = \Phi^T \mathbf{f} \quad (5.7)$$

Now a set of N independent ordinary differential equations has been obtained, meaning that the size of the problem is still the same. To reduce the latter, the subspace \mathbf{V} is truncated to include only the first $m < N$ mode shapes

$$\mathbf{V} = [\phi_1, \dots, \phi_m] \quad (5.8)$$

This type of reduction is not convenient for the dynamic analysis of nonlinear system as it relies on a linear combination of the mode shapes, and it is not particularly efficient as it may require to retain too many master DOFs.

5.1.2 Guyan Reduction

The Guyan reduction is based on the assumption that the slave generalized displacements \mathbf{q}_s can be computed directly from master displacements \mathbf{q}_m . [23] In order to link the two DOFs it introduces two important hypothesis:

- Negation of the forces applied to slave DOFs;
- Assumption of a static deflection as the relationship between \mathbf{q}_s and \mathbf{q}_m , i.e. neglecting inertia forces and damping.

Before operating the reduction, divide the dynamic system separating the master DOFs \mathbf{q}_m from the slaves \mathbf{q}_s

$$\begin{bmatrix} \mathbf{M}_{11} & \mathbf{M}_{12} \\ \mathbf{M}_{21} & \mathbf{M}_{22} \end{bmatrix} \begin{Bmatrix} \ddot{\mathbf{q}}_m \\ \ddot{\mathbf{q}}_s \end{Bmatrix} + \begin{bmatrix} \mathbf{C}_{11} & \mathbf{C}_{12} \\ \mathbf{C}_{21} & \mathbf{C}_{22} \end{bmatrix} \begin{Bmatrix} \dot{\mathbf{q}}_m \\ \dot{\mathbf{q}}_s \end{Bmatrix} + \begin{bmatrix} \mathbf{K}_{11} & \mathbf{K}_{12} \\ \mathbf{K}_{21} & \mathbf{K}_{22} \end{bmatrix} \begin{Bmatrix} \mathbf{q}_m \\ \mathbf{q}_s \end{Bmatrix} = \begin{Bmatrix} \mathbf{f}_m \\ \mathbf{f}_s \end{Bmatrix} \quad (5.9)$$

From the second hypothesis introduced we can express the relationships between master and slave DOFs as

$$\mathbf{K}_{21}\mathbf{q}_m + \mathbf{K}_{22}\mathbf{q}_s = \mathbf{0} \quad \Rightarrow \quad \mathbf{q}_s = -\mathbf{K}_{22}^{-1} \cdot \mathbf{K}_{21}\mathbf{q}_m \quad (5.10)$$

Thus, the transformation matrix corresponding to this condensation can be built as

$$\mathbf{V} = \begin{bmatrix} \mathbf{I} \\ -\mathbf{K}_{22}^{-1} \cdot \mathbf{K}_{21} \end{bmatrix} \quad (5.11)$$

The main takeaways from this condensation techniques are: [33]

- The inertia contribution from slave DOFs is not entirely neglected. It can be seen by stating the condensed mass matrix

$$\mathbf{M}_{cond} = \mathbf{M}_{11} - \mathbf{M}_{12}\mathbf{K}_{22}^{-1}\mathbf{K}_{21} - (\mathbf{M}_{12}\mathbf{K}_{22}^{-1}\mathbf{K}_{21})^T + \mathbf{K}_{12}\mathbf{K}_{22}^{-1}\mathbf{M}_{22}\mathbf{K}_{22}^{-1}\mathbf{K}_{21}$$

- Eigenvalues of the reduced system are always higher than those of the original system;
- It is not a particular expensive technique as it requires the inversion of the \mathbf{K}_{22} matrix only;
- The quality of the eigenvalue approximation decreases as the mode number increases.

5.1.3 Craig-Bampton Method

The Craig-Bampton methodology is a widely used technique in the aerospace industry, particularly where two or more subsystems are connected. [34] It re-characterizes large finite element models into a set of relatively small matrices containing mass, stiffness and mode shape information, consisting of all boundary modes expressed in physical coordinates and a truncated set of elastic modes expressed in modal coordinates. [35]

Since the method requires the use of boundary and interior points, it is convenient to partition the nodes in boundary nodes, identified with subscript B , and independent elastic ones, indicated by subscript L

$$\mathbf{x} = \begin{Bmatrix} \mathbf{x}_B \\ \mathbf{x}_L \end{Bmatrix} \quad (5.12)$$

thus obtaining the following dynamic equation

$$\begin{bmatrix} \mathbf{M}_{BB} & \mathbf{M}_{BL} \\ \mathbf{M}_{LB} & \mathbf{M}_{LL} \end{bmatrix} \begin{Bmatrix} \ddot{\mathbf{x}}_B \\ \ddot{\mathbf{x}}_L \end{Bmatrix} + \begin{bmatrix} \mathbf{C}_{BB} & \mathbf{C}_{BL} \\ \mathbf{C}_{LB} & \mathbf{C}_{LL} \end{bmatrix} \begin{Bmatrix} \dot{\mathbf{x}}_B \\ \dot{\mathbf{x}}_L \end{Bmatrix} + \begin{bmatrix} \mathbf{K}_{BB} & \mathbf{K}_{BL} \\ \mathbf{K}_{LB} & \mathbf{K}_{LL} \end{bmatrix} \begin{Bmatrix} \mathbf{x}_B \\ \mathbf{x}_L \end{Bmatrix} = \begin{Bmatrix} \mathbf{f}_B \\ \mathbf{f}_L \end{Bmatrix} \quad (5.13)$$

The first step of this reduction technique is to transform the set of independent elastic nodes from the physical coordinates \mathbf{x}_L to the modal coordinates \mathbf{Q}_L . Then the set is truncated into a smaller one \mathbf{q}_m : in this way it is possible to reduce the size of the problem making it lighter from a computational perspective.

Therefore it is possible to summarise the relationship between the new set of hybrid coordinates and the physical ones as

$$\begin{Bmatrix} \mathbf{x}_B \\ \mathbf{x}_L \end{Bmatrix} = \begin{bmatrix} \mathbf{B} & \mathbf{\Phi} \end{bmatrix} \begin{Bmatrix} \mathbf{x}_B \\ \mathbf{q}_m \end{Bmatrix} \quad \text{where} \quad \text{size}(\mathbf{q}_m) < \text{size}(\mathbf{x}_L) \quad (5.14)$$

Behind the matrices \mathbf{B} and $\mathbf{\Phi}$ lies the actual reduction technique: the vectors in \mathbf{B} are usually referred to as the **Boundary Node Functions** and the vectors in $\mathbf{\Phi} \in \mathfrak{R}^{N \times m}$ are usually referred to as the **Fixed Base Mode Shapes**.

First let start from computing the constraint modes: the matrix can be partitioned as follows

$$\mathbf{B} = \begin{bmatrix} \mathbf{I}_{BB} \\ \mathbf{\Psi}_B \end{bmatrix} \in \mathfrak{R}^{N \times B} \quad \text{where} \quad \begin{cases} \mathbf{I}_{BB} \in \mathfrak{R}^{B \times B} \\ \mathbf{\Psi}_B \in \mathfrak{R}^{L \times B} \end{cases} \quad (5.15)$$

$\mathbf{\Psi}_B$ is the transformation matrix relating *rigid body displacements* at the interface \mathbf{x}_B to physical displacements of the elastic degrees of freedom \mathbf{x}_L [35], while \mathbf{I} is simply the identity matrix. To determine the former, a static deformation of the structure is induced by successive unit deflections of each boundary DOF with the remaining ones of the set held fixed, meanwhile all the internal DOFs are force-free [34]

$$\begin{bmatrix} \mathbf{K}_{BB} & \mathbf{K}_{BL} \\ \mathbf{K}_{LB} & \mathbf{K}_{LL} \end{bmatrix} \begin{bmatrix} \mathbf{I}_{BB} \\ \mathbf{u}_L \end{bmatrix} = \begin{bmatrix} \mathbf{R}_{BB} \\ \mathbf{0}_{LB} \end{bmatrix} \quad (5.16)$$

Then the transformation matrix is obtained by computing the lower row

$$\mathbf{u}_L = -\mathbf{K}_{LL}^{-1} \mathbf{K}_{LB} \mathbf{I}_{BB} = \mathbf{\Psi}_B \mathbf{I}_{BB} \quad (5.17)$$

Now the normal modes have to be computed: again it is convenient to partition the transformation matrix

$$\mathbf{\Phi} = \begin{bmatrix} \mathbf{0} \\ \mathbf{\Phi}_L \end{bmatrix} \in \mathfrak{R}^{N \times m} \quad \text{where} \quad \begin{cases} \mathbf{0} \in \mathfrak{R}^{B \times m} \\ \mathbf{\Phi}_L \in \mathfrak{R}^{L \times m} \end{cases} \quad (5.18)$$

Computing the matrix $\mathbf{\Phi}_L$ is fairly easy as it corresponds to the mode shapes obtained by a modal analysis in which all the boundary DOFs are fixed, i.e. solving the following eigenproblem

$$\left[\mathbf{K}_{LL} - \omega^2 \mathbf{M}_{LL} \right] \mathbf{\Phi}_L = \mathbf{0} \quad (5.19)$$

Note that the two matrices $\mathbf{\Psi}_B$ and $\mathbf{\Phi}_L$ are linearly independent.

To summarize, the subspace used in the Craig-Bampton reduction is

$$\mathbf{V}_{CB} = \begin{bmatrix} \mathbf{I}_{BB} & \mathbf{0} \\ \boldsymbol{\Psi}_B & \boldsymbol{\Phi}_L \end{bmatrix} = \begin{bmatrix} \mathbf{I}_{BB} & \mathbf{0} \\ \boldsymbol{\Psi}_B & \boldsymbol{\Phi}_L \end{bmatrix} \in \mathfrak{R}^{N \times (B+m)} \quad (5.20)$$

and the reduced matrices are simply obtained as

$$\begin{aligned} \mathbf{M}_{CB} &= \mathbf{V}_{CB}^T \mathbf{M} \mathbf{V}_{CB} \\ \mathbf{K}_{CB} &= \mathbf{V}_{CB}^T \mathbf{K} \mathbf{V}_{CB} \end{aligned} \quad (5.21)$$

whose size is equal to $(B + m) \times (B + m)$.

Bladh et al. [36] show the application of the Craig-Bampton technique to the nonlinear analysis of a bladed disk, while Battiato et al. [7] have proposed to use this method to study multi-staged bladed discs: in literature it is also possible to find methods directly derived from the Craig-Bampton one, e.g. [37].

5.2 Hybrid Method

Petrov [32] has proposed a highly accurate and computationally efficient method for reduced modelling of jointed structures in the frequency domain analysis of nonlinear steady-state forced response. Therefore this method is particularly suited to work together with the harmonic balance method and for this very reason is used in **FORSE**, the in-house software developed by Imperial College for nonlinear forced response analyses.

The nonlinear dynamic problem to solve is

$$\mathbf{M}\ddot{\mathbf{x}}(t) + \mathbf{C}\dot{\mathbf{x}}(t) + \mathbf{K}\mathbf{x}(t) + \mathbf{f}(\dot{\mathbf{x}}(t), \mathbf{x}(t)) = \mathbf{p}(t) \quad (5.22)$$

where $\mathbf{f}(\dot{\mathbf{x}}(t), \mathbf{x}(t))$ is the vector of the nonlinear forces at the contact interfaces and $\mathbf{p}(t)$ is a vector of periodic external excitation force.

The steady-state solution is represented by a truncated Fourier series, see Chapter 4 for the explanation of the HBM

$$\mathbf{x}(t) \approx \mathbf{x}_h(t) = \tilde{\mathbf{Q}}_0 + \sum_{j=1}^H \tilde{\mathbf{Q}}_j^{(c)} \cos(m_j \omega t) + \tilde{\mathbf{Q}}_j^{(s)} \sin(m_j \omega t) \quad (5.23)$$

where m_j is the j -th harmonic coefficient.

The idea of this technique is to keep only the nonlinear DOFs, where the nonlinear forces act, while reducing all the linear DOFs. This reduction is done by using the FRF matrix [32]

$$\tilde{\mathbf{Q}}_j = \tilde{\mathbf{Q}}_j^{(c)} + i\tilde{\mathbf{Q}}_j^{(s)} = \mathbf{A}(m_j \omega)(\mathbf{P}_j - \mathbf{F}_j(\tilde{\mathbf{Q}}_j)) \quad (5.24)$$

where $\mathbf{A} = [\mathbf{K} - \omega^2 \mathbf{M} + i\omega \mathbf{C}]$ is the FRF matrix, while $\mathbf{P}_j = \mathbf{P}_j^{(c)} + i\mathbf{P}_j^{(s)}$ and $\mathbf{F}_j(\tilde{\mathbf{Q}}_j) = \mathbf{F}_j^{(c)} + i\mathbf{F}_j^{(s)}$ are respectively the complex vectors of the external and nonlinear forces.

The partition of the nodes in nonlinear and linear, for the j -th harmonic, is written as

$$\begin{Bmatrix} \tilde{\mathbf{Q}}^l \\ \tilde{\mathbf{Q}}^n \end{Bmatrix} = \begin{bmatrix} \mathbf{A}_{ll} & \mathbf{A}_{ln} \\ \mathbf{A}_{nl} & \mathbf{A}_{nn} \end{bmatrix} \begin{Bmatrix} \mathbf{P}^l \\ \mathbf{P}^n - \mathbf{F}(\tilde{\mathbf{Q}}^n) \end{Bmatrix} \quad (5.25)$$

from which the nonlinear DOFs equation can be retrieved

$$\tilde{\mathbf{Q}}^n = \mathbf{A}_{nl}(\omega) \mathbf{P}^l + \mathbf{A}_{nn}(\omega) \mathbf{P}^n - \mathbf{A}_{nn}(\omega) \mathbf{F}(\tilde{\mathbf{Q}}^n) \quad (5.26)$$

The method is based on the idea of the building the FRF matrix by computing its exact values at a certain frequency and providing its high-accuracy estimation in a wide frequency range close to this frequency

$$\mathbf{A} = \mathbf{A}_0 + \tilde{\mathbf{A}}(\omega) \quad (5.27)$$

where \mathbf{A}_0 allows to capture the local elastic properties while $\tilde{\mathbf{A}}(\omega)$ describes the FRF matrix variation over the frequency range. The former is computed at a specific frequency ω_0 far enough from any natural frequency of the system, if the structure has no possible rigid body motion then a null frequency can be chosen

$$[(1 + i\eta)\mathbf{K} - \omega_0^2 \mathbf{M}] \begin{Bmatrix} \mathbf{A}_{ln}^0 \\ \mathbf{A}_{nn}^0 \end{Bmatrix} = \mathbf{I} \quad (5.28)$$

where η is the modal damping factor.

The frequency dependent contribution is obtained so that \mathbf{A} is equal to \mathbf{A}_0 if $\omega = \omega_0$

$$\tilde{\mathbf{A}}(\omega) = \mathbf{A} - \mathbf{A}_0 \quad (5.29)$$

and since a generic FRF matrix can be estimated knowing the mode shapes as

$$\text{FRF} \approx \sum_{j=1}^{N_m} \frac{\phi_j \phi_j^T}{(1 + i\eta_j)\omega_j^2 - \omega^2}$$

the frequency dependent is computed as

$$\begin{aligned} \tilde{\mathbf{A}}(\omega) &= \sum_{j=1}^N \frac{\phi_j \phi_j^T}{(1 + i\eta_j)\omega_j^2 - \omega^2} - \sum_{j=1}^N \frac{\phi_j \phi_j^T}{(1 + i\eta_j)\omega_j^2 - \omega_0^2} \\ &\approx (\omega^2 - \omega_0^2) \sum_{j=1}^{N_m} \frac{\phi_j \phi_j^T}{[(1 + i\eta_j)\omega_j^2 - \omega^2][(1 + i\eta_j)\omega_j^2 - \omega_0^2]} \end{aligned} \quad (5.30)$$

with $\tilde{\mathbf{A}}(\omega)$ estimation limited only to the first N_m modes.

The new formulation of the FRF matrix is then used to compute the harmonics coefficient of the nonlinear DOFs

$$\tilde{\mathbf{Q}}^n = \tilde{\mathbf{Q}}_0 + \hat{\mathbf{Q}}_n(\omega) - [\mathbf{A}_{nn}^0 + \tilde{\mathbf{A}}_{nn}(\omega)] \mathbf{F}(\tilde{\mathbf{Q}}) \quad (5.31)$$

where

$$\tilde{\mathbf{Q}}_0 = \mathbf{A}_{nl}^0 \mathbf{P}^l + \mathbf{A}_{nn}^0 \mathbf{P}^n \quad (5.32)$$

$$\hat{\mathbf{Q}}_n(\omega) = \tilde{\mathbf{A}}_{nl} \mathbf{P}^l + \tilde{\mathbf{A}}_{nn}(\omega) \mathbf{P}^n \quad (5.33)$$

Moreover $\hat{\mathbf{Q}}_n(\omega)$ can be expressed as

$$\hat{\mathbf{Q}}_n(\omega) = \sum_{j=1}^{N_m} \frac{(\omega^2 - \omega_0^2) \mathbf{c}_j}{[(1 + i\eta_j)\omega_j^2 - \omega^2] [(1 + i\eta_j)\omega_j^2 - \omega_0^2]} \phi_j^n \quad (5.34)$$

where

$$\mathbf{c}_j = \begin{Bmatrix} \phi_j^l \\ \phi_j^n \end{Bmatrix}^H \begin{Bmatrix} \mathbf{P}_j^l \\ \mathbf{P}_j^n \end{Bmatrix} \quad (5.35)$$

is the modal excitation force of the j -th mode. Both $\tilde{\mathbf{Q}}_0$ and the modal forces \mathbf{c}_j can be calculated only once, independently, and beforehand of the nonlinear forced response analysis. As a result, the analysis will involve solving the nonlinear equation where explicitly only nonlinear DOFs are included. [32]

Chapter 6

Free Vibrations of a Rotationally Periodic Structure

Here a simplified approach to the dynamics of bladed discs is presented by studying simplified discrete models of *cyclically periodic structures*. These, however, give important indications on the behaviour of the disc and on the boundary conditions that need to be applied in the finite element method.

6.1 Tuned System Model

Assuming that all sectors are equal, the cyclic symmetry of the turbomachinery can be exploited: a simplified model with one degree of freedom for the fundamental sector of a bladed disc is reported in Figure 6.1. [38]

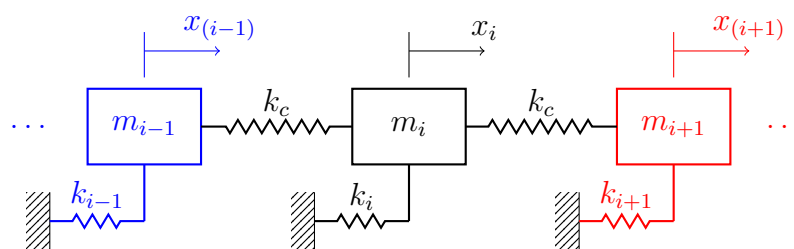


Figure 6.1: 1DOF Bladed Disc Model

The model presented considers only one mode of vibration per blade. This is a rough approximation: in fact, when studying the dynamics of bladed discs, given their high lightness, the disc can not be modelled as infinitely rigid but its elasticity must be studied.

Modal mass and stiffness of each blade, linked rigidly to the disc, are represented by m and k , respectively. These quantities are expressed as

$$\begin{aligned} m_i &= m_b + \delta m_i \quad i = 1, 2, \dots, n_s \\ k_i &= k_b + \delta k_i \quad i = 1, 2, \dots, n_s \end{aligned}$$

For a mistuned system, $\delta m_i \neq 0$ and $\delta k_i \neq 0$ [38], but in case of a tuned system the following simplification can be made

$$m_i = m_b \quad k_i = k_b$$

The structural coupling between adjacent sectors due to the disk flexibility is represented by a spring with stiffness k_c . Despite the many approximation, such as the rigid disc or the absence of the blade coupling due to the shroud, from this simple model it is still possible to capture the basic behaviour of a more complex structure such as that of bladed discs and some general observations can be made.

The governing system of differential equations for each i -th sector is represented by

$$m_i \ddot{x}_i + k_i x_i + k_c(x_i - x_{i+1}) + k_c(x_i - x_{i-1}) = 0 \quad (6.1)$$

It is important to observe that, due to the rotational periodicity, $i + 1 = 1$ when $i = n_s$ and $i - 1 = n_s$ when $i = 1$.

From the governing equation of the fundamental sector it is possible to build the system of the entire bladed disc as

$$[M] \ddot{\mathbf{x}} + [K] \mathbf{x} = \mathbf{0} \quad (6.2)$$

where the mass matrix is a block diagonal one

$$[M] = \begin{bmatrix} m_b & 0 & \dots & & 0 \\ 0 & m_b & \ddots & & \\ & \ddots & \ddots & 0 & \\ \vdots & & 0 & m_b & 0 & \vdots \\ & & & 0 & \ddots & \ddots \\ & & & & \ddots & m_b & 0 \\ 0 & & \dots & & 0 & m_b \end{bmatrix}$$

and the stiffness matrix is a block circulant one

$$[K] = \begin{bmatrix} k_b + 2k_c & -k_c & 0 & \dots & & 0 & -k_c \\ -k_c & k_b + 2k_c & -k_c & & & 0 & 0 \\ & \ddots & \ddots & \ddots & & & \\ \vdots & & -k_c & k_b + 2k_c & -k_c & & \vdots \\ & & & \ddots & \ddots & \ddots & \\ 0 & 0 & & & -k_c & k_b + 2k_c & -k_c \\ -k_c & 0 & \dots & 0 & -k_c & k_b + 2k_c \end{bmatrix}$$

6.2 Eigenvalues and Eigenvectors

The determinant of the eigenproblem

$$[K] \phi = \omega^2 [M] \phi \quad (6.3)$$

due to the properties of circulant block matrices [see 13] yields the following result: [38]

$$\begin{cases} k_b - \omega^2 m_b \prod_{l=1}^{\frac{n_s-1}{2}} (k_b - \omega^2 m_b + 2k_c (1 - \cos(l\theta))^2) & n_s \text{ odd} \\ k_b - \omega^2 m_b \left[\prod_{l=1}^{\frac{n_s-2}{2}} (k_b - \omega^2 m_b + 2k_c (1 - \cos(l\theta))^2) \right] (k_b - \omega^2 m_b + 4k_c) & n_s \text{ even} \end{cases}$$

This means that there are $(n_s - 1)/2$ and $(n_s - 2)/2$ repeated frequencies for n_s odd and even respectively. It can be shown that the corresponding eigenvectors are

$$\phi_l = \frac{1}{\sqrt{n_s m_b}} \left[1 \quad e^{j\theta l} \quad e^{j2\theta l} \quad \dots \quad e^{j(n_s-1)\theta l} \right]^T \quad (6.4)$$

where

$$l = 0, 1, 2, \dots, n_s - 1 \quad j = \sqrt{-1}$$

The angle

$$\theta = \frac{2\pi}{n_s}$$

is the *intermass phase angle* [38] and it corresponds to the angle swept by each sector of the bladed disc, but it also, as will be explained later, affects the *phase shift* of the response between adjacent sectors.

Usually the eigenvectors are scaled so that:

$$\Phi^H [M] \Phi = \mathbf{I} \quad \Phi^H [K] \Phi = \Lambda^2$$

where

$$\Lambda^2 = \begin{bmatrix} \omega_1^2 & & & & \\ & \omega_2^2 & & & \\ & & \ddots & & \\ & & & \omega_{n_s-1}^2 & \\ & & & & \omega_{n_s}^2 \end{bmatrix}$$

$$\Phi = [\phi_1 \quad \phi_2 \quad \dots \quad \phi_{n_s-1} \quad \phi_{n_s}]$$

and Φ^H is the complex conjugate of Φ .

Since the number of pairs of equal natural frequencies is $(n_s - 1)/2$ and $(n_s - 2)/2$ for n_s odd and even, it means that the number of unrepeated frequencies is 1 and 2 for odd and even number of blades:

- for odd n_s the unique frequency corresponds to the 0 degree phase shift
- for even n_s the two unrepeated eigenvalues represent the 0 and 180 degrees phase angle modes

For the pairs of equal eigenvalues, the eigenvectors obtained are not unique as well: in fact the linear combination of two independent eigenvectors ϕ_l and ϕ_{n_s-l} , corresponding to the value ω_l , is still an eigenvector since

$$k(\alpha\phi_l + \beta\phi_{n_s-l}) = \omega_l^2 m(\alpha\phi_l + \beta\phi_{n_s-l})$$

Therefore, the expression for the generic eigenvector is:

$$\begin{aligned} \alpha\phi_l + \beta\phi_{n_s-l} &= \frac{\alpha}{\sqrt{n_s m_b}} \begin{bmatrix} 1 \\ e^{jl\theta} \\ \vdots \\ e^{j(n_s-1)l\theta} \end{bmatrix} + \frac{\beta}{\sqrt{n_s m_b}} \begin{bmatrix} 1 \\ e^{-jl\theta} \\ \vdots \\ e^{-j(n_s-1)l\theta} \end{bmatrix} \\ &= \frac{\alpha + \beta}{\sqrt{n_s m_b}} \begin{bmatrix} 1 \\ \cos(l\theta) \\ \vdots \\ \cos((n_s - 1)l\theta) \end{bmatrix} + j \frac{\alpha - \beta}{\sqrt{n_s m_b}} \begin{bmatrix} 0 \\ \sin(l\theta) \\ \vdots \\ \sin((n_s - 1)l\theta) \end{bmatrix} \end{aligned}$$

This lead us to describe the pair of independent eigenvectors for a repeated natural frequencies in terms of their trigonometric component

$$\begin{bmatrix} 1 \\ \cos(l\theta) \\ \vdots \\ \cos((n_s - 1)l\theta) \end{bmatrix} \quad \text{and} \quad \begin{bmatrix} 0 \\ \sin(l\theta) \\ \vdots \\ \sin((n_s - 1)l\theta) \end{bmatrix}$$

with $l = \begin{cases} l = 1, 2, \dots, \frac{n_s - 1}{2} & \text{for odd } n_s \\ l = 1, 2, \dots, \frac{n_s}{2} - 1 & \text{for even } n_s \end{cases}$

which highlights one of the most important properties: the eigenvectors are *orthogonal*

$$\begin{bmatrix} 1 & \cos(l\theta) & \dots & \cos((n_s - 1)l\theta) \end{bmatrix} \begin{bmatrix} 0 \\ \sin(l\theta) \\ \vdots \\ \sin((n_s - 1)l\theta) \end{bmatrix} = 0$$

All the equations are dependent on the parameter l , called **harmonic index**, which has a physical meaning: in fact it stands for the number of sign changes in the displacements of the masses in the model. This parameter coincides with the **nodal**

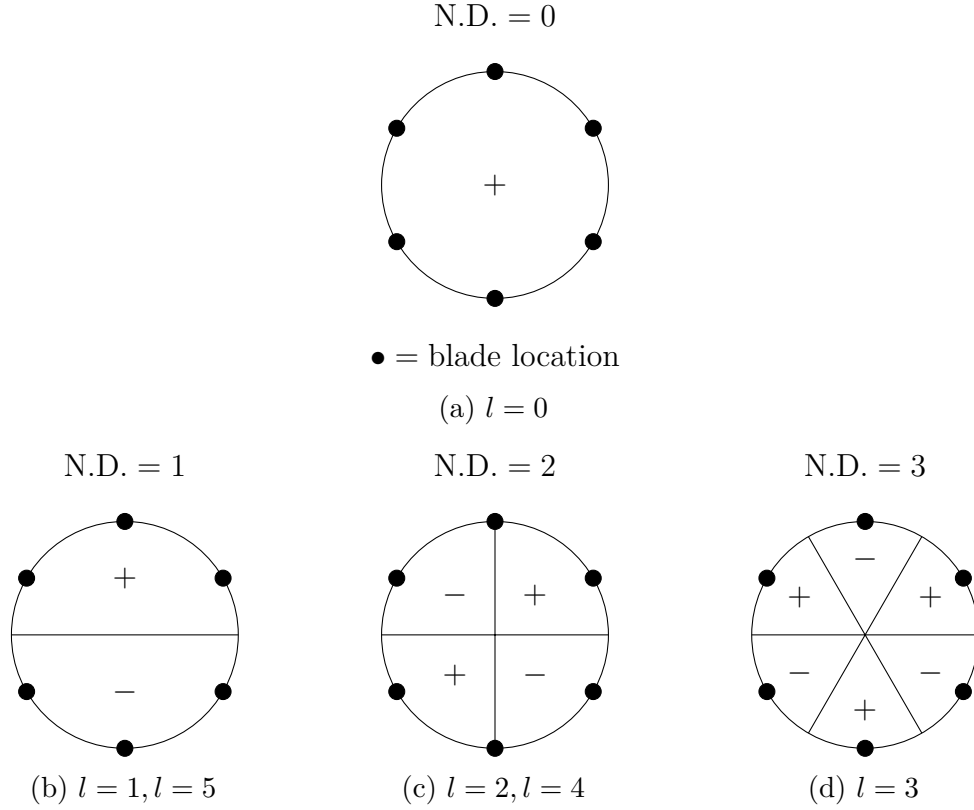


Figure 6.2: Nodal Diameter Visualization, 6 blade configuration

diameters number introduced for circular disc vibration. It is useful to remember that the nodal diameters range from 0 to $(n_s - 1)/2$ or $n_s/2 - 1$, depending whether the number of sectors is odd or even.

Another important result is the fact that the generic eigenvectors ϕ_l and ϕ_{n_s-l} can be described only by their first term corresponding to the first sector eigenvector $\phi_l^{(1)}$ and $\phi_{n_s-l}^{(1)}$. In fact the complex relationship between the generic n -th sector and the first one is

$$\phi_l^{(n)} = \phi_l^{(1)} \cdot e^{j(n-1)l\theta} \quad \phi_{n_s-l}^{(n)} = \phi_{n_s-l}^{(1)} \cdot e^{-j(n-1)l\theta} \quad (6.5)$$

In this case each sector has only one degree of freedom, but this applies to multi-degree of freedoms systems too.

Following this observation, if we use the real coordinates to express the relationship between the eigenvectors

$$\begin{Bmatrix} \phi_l^{(n)} \\ \phi_{n_s-l}^{(n)} \end{Bmatrix} = \begin{bmatrix} \mathbf{I} \cos(l\theta) & \mathbf{I} \sin(l\theta) \\ -\mathbf{I} \sin(l\theta) & \mathbf{I} \cos(l\theta) \end{bmatrix} \begin{Bmatrix} \phi_l^{(1)} \\ \phi_{n_s-l}^{(1)} \end{Bmatrix} \quad (6.6)$$

and focusing on the first line

$$\phi_l^{(n)} = \phi_l^{(1)} \cos(l\theta) + \phi_{n_s-l}^{(1)} \sin(l\theta)$$

we can note that, since $\phi_l^{(1)}$ and $\phi_{n_s-l}^{(1)}$ are orthogonal, this corresponds to obtaining $\phi_l^{(n)}$ from a rigid rotation of $\phi_l^{(1)}$.

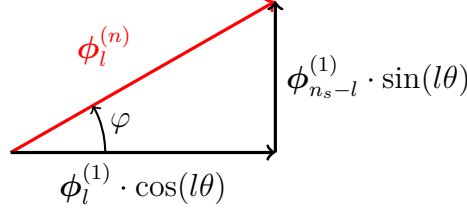


Figure 6.3: Eigenvector Rigid Rotation

The angle of the rigid rotation is

$$\varphi = l\theta = l \frac{2\pi}{n_s} \quad (6.7)$$

which is the phase shift between consecutive eigenvectors and it is called **interblade phase angle**. This means that the eigenvectors of the first sector form an orthogonal base of the space containing all the eigenvectors of the bladed disc: therefore it is possible to describe the entire structure with an equivalent model of a single sector, see 6.4.

Finally it is important to observe that the symmetry of the structure is respected from eigenvectors relationship: i.e. when making a complete rotation the equation (6.5) returns an identity since $e^{jk\varphi} = 1$ for $l = n_s$, $\varphi = 2\pi$ and $n = n_s + 1$.

6.3 Travelling and Standing Wave

The free vibration response of each modal vector

$$\mathbf{x}(t) = \frac{\alpha}{\sqrt{n_s m_b}} \begin{bmatrix} 1 \\ e^{jl\theta} \\ \vdots \\ e^{j(n_s-1)l\theta} \end{bmatrix} e^{j\omega t}$$

can be seen as a *travelling wave* where the phase of sinusoidal vibration of each blade changes by a constant value between each adjacent blade. The wave is said to be travelling forward if clockwise and backward if anticlockwise.

The combination of a forward and a backward wave generates a standing wave

$$\mathbf{x}(t) = \frac{\alpha}{\sqrt{n_s m_b}} \begin{bmatrix} 1 \\ e^{jl\theta} \\ \vdots \\ e^{j(n_s-1)l\theta} \end{bmatrix} e^{j\omega t} + \frac{\beta}{\sqrt{n_s m_b}} \begin{bmatrix} 1 \\ e^{-jl\theta} \\ \vdots \\ e^{-j(n_s-1)l\theta} \end{bmatrix} e^{j\omega t} \quad (6.8)$$

and as shown in [38], if α and β are chosen so that they are complex conjugates

$$\alpha = |\alpha|e^{j\psi} \quad \beta = \alpha^* = |\alpha|e^{-j\psi}$$

and substituting them in (6.8), it is possible to write it as

$$\mathbf{x}(t) = \frac{2|\alpha|}{\sqrt{n_s m_b}} \begin{bmatrix} \cos(\psi) \\ \cos(l\theta + \psi) \\ \vdots \\ \cos((n_s - 1)l\theta + \psi) \end{bmatrix} \cos\left(\omega t + \frac{\pi}{4}\right)$$

meaning that each blade vibrates with the same frequency albeit with different amplitude.

6.4 Equivalent Model

It is convenient now to exploit the symmetric property of both the structure and its modeshape, creating an equivalent model *for each nodal diameter l with only one degree of freedom*.

The relationship between displacements of consecutive sectors can be retrieved from (6.4) and expressed as

$$x_{i+1} = x_i e^{jl\theta} \quad x_{i-1} = x_i e^{-jl\theta} \quad (6.9)$$

therefore by substituting it in (6.1)

$$m_b \ddot{x}_i + (k_b + 2k_c)x_i - k_c x_i e^{jl\theta} - k_c x_i e^{-jl\theta} = 0 \quad (6.10)$$

which lead to [38]

$$m_b \ddot{x}_i + \left[k_b + 4k_c \sin^2\left(\frac{l\theta}{2}\right) \right] x_i = 0 \quad \rightarrow \quad \omega_l = \sqrt{\frac{k_b + 4k_c \sin^2\left(\frac{l\theta}{2}\right)}{m_b}}$$

where $l = 0, 1, 2, \dots, n_s - 1$. This is an extremely important result and it is valid for the analysis of bladed disc as well, meaning that only one sector instead of the full structure can be analysed.

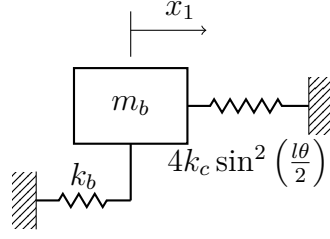


Figure 6.4: Equivalent Model

6.5 Frequency Veering

The **veering phenomenon** consists of natural frequencies coming closer and then veering away from each other as the nodal diameter varies; it is exhibited by tuned bladed discs and periodic structure.

To catch this phenomenon the disk contribution to the modal behaviour has to be considered: in fact, given the high lightness of the structure, the disc can not be modelled as infinitely rigid but its elasticity must be taken in consideration.

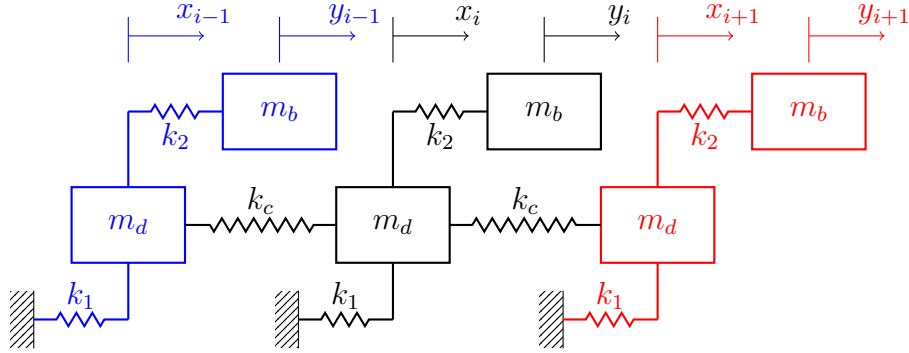


Figure 6.5: 2 DOFs per Sector Model

The equations of motion of the system, depicted in Figure 6.5, are

$$\begin{cases} m_d \ddot{x}_i + k_d x_i + k_b (x_i - y_i) + k_c (x_i - x_{i-1}) + k_c (x_i - x_{i+1}) = 0 \\ m_b \ddot{y}_i + k_b (y_i - x_i) = 0 \end{cases} \quad (6.11)$$

whose matrix form is

$$\begin{bmatrix} m_d & 0 \\ 0 & m_b \end{bmatrix} \ddot{\mathbf{z}}_i + \begin{bmatrix} k_d + k_b + 2k_c & -k_b \\ -k_b & k_b \end{bmatrix} \mathbf{z}_i - \begin{bmatrix} k_c & 0 \\ 0 & 0 \end{bmatrix} \mathbf{z}_{i-1} - \begin{bmatrix} k_c & 0 \\ 0 & 0 \end{bmatrix} \mathbf{z}_{i+1} = \mathbf{0}$$

where

$$\mathbf{z} = [x_1 \quad y_1 \quad x_2 \cdots y_{n_s-1} \quad x_{n_s} \quad y_{n_s}]^T; \quad i = 1, 2, \dots, n_s$$

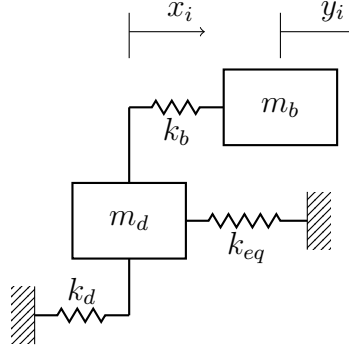


Figure 6.6: 2 DOFs Equivalent Model

Again it is convenient to reduce the size of the problem to an equivalent model consisting of a single sector, as shown in Figure 6.6. In order to do so, it is important to remind that

$$x_{i+1} = x_i e^{j l \theta} \quad x_{i-1} = x_i e^{-j l \theta}$$

is still valid and by substituting it in (6.11), the following is obtained

$$m_d \ddot{x}_i + (k_d + k_{eq} + k_b) x_i - k_b y_i = 0 \quad (6.12)$$

where

$$k_{eq} = 4k_c \sin^2 \left(\frac{l\theta}{2} \right)$$

The determinant of the new eigenproblem is [38]

$$\det(\mathbf{K}_s - \omega^2 \mathbf{M}_s) = m_b m_d \omega^4 - [(k_d + k_{eq} + k_b) m_b + k_b m_d] \omega^2 + (k_d + k_{eq}) k_b = 0 \quad (6.13)$$

where

$$\mathbf{M}_s = \begin{bmatrix} m_d & 0 \\ 0 & m_b \end{bmatrix} \quad \mathbf{K}_s = \begin{bmatrix} k_d + k_b + 4k_c \sin^2 \left(\frac{l\theta}{2} \right) & -k_b \\ -k_b & k_b \end{bmatrix}$$

By comparing the natural frequencies obtained from the determinant (6.13) with the one computed considering the blade and the disc alone

$$\omega_b = \sqrt{\frac{k_b}{m_b}} \quad \omega_d = \sqrt{\frac{k_d + 4k_c \sin^2 \left(\frac{l\theta}{2} \right)}{m_d}}$$

it is possible to highlight the frequency veering phenomenon, see Figure 6.7. At lower nodal diameters the lower frequencies are close to those of the disc alone, while the higher are close to the ones of the blade. At nodal diameter $l = 2$ the frequency difference of the bladed disc is at its minimum. After that the frequencies veer away from each other and from then on the higher and lower frequencies become closer to those of the disc and blade alone respectively, opposite to the previous situation.

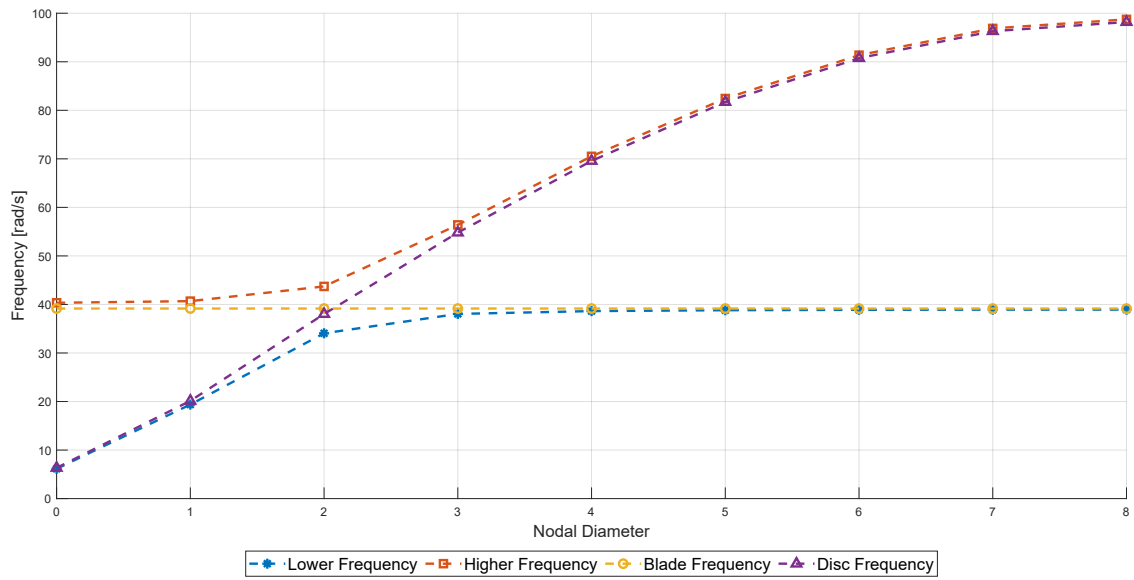


Figure 6.7: Natural Frequencies of the 2 DOFs Tuned System

Chapter 7

Nonlinear Forced Response of Bladed Disc

The aim of this chapter is to illustrate how a bladed disc is analysed using the finite element method first, to compute a static or a modal analysis, and then with harmonic balance in order to compute the forced response to the resonant engine order excitation.

In fact is now common practice to reduce the model from the full assembly to a single sector as it improves the computation efficiency without losing in accuracy: the coupling of the sectors is taken into account for by specific boundary conditions imposed at the interfaces where neighbouring sectors interact.

So an introduction to the use of cyclic symmetry when dealing with a finite element model is provided, as well as a look at the contact models used within harmonic balance method, and finally a strategy for solving the nonlinear forced response.

7.1 Problem Definition

If a bladed disc is cyclically symmetric its equations of motion can be written in the following form: [39]

$$\mathbf{K}\mathbf{q}_j + \mathbf{C}\dot{\mathbf{q}}_j + \mathbf{M}\ddot{\mathbf{q}}_j + \mathbf{f}_i(\mathbf{q}_j) + \mathbf{f}_l(\mathbf{q}_{j-1}, \mathbf{q}_j) + \mathbf{f}_r(\mathbf{q}_{j+1}, \mathbf{q}_j) = \mathbf{p}_j(t) \quad (7.1)$$

where $j = 1, \dots, N$ is the sector number; \mathbf{K} , \mathbf{C} and \mathbf{M} are respectively the stiffness, damping and mass matrix of the single sector; $\mathbf{f}_i(\mathbf{q}_j)$ are the internal forces; $\mathbf{f}_l(\mathbf{q}_{j-1}, \mathbf{q}_j)$ and $\mathbf{f}_r(\mathbf{q}_{j+1}, \mathbf{q}_j)$ are the interaction forces with the left and right adjacent sector; while $\mathbf{p}_j(t)$ are the external forces applied to the sector.

If the latter is an arbitrary **periodic excitation** applied to each sector and distributed similarly over the sector nodes, different only in a **fixed phase shift**,

δt , between adjacent sectors, then it can be written as

$$\mathbf{p}_j(t) = \mathbf{p}(t + (j - 1)\delta t) = \mathbf{p}(t_j) \quad (7.2)$$

Given the symmetry of the geometry, the excitation and the assembly properties then also a relationship for the displacements of each sector can be written as

$$\mathbf{q}_j(t) = \mathbf{q}(t + (j - 1)\delta t) = \mathbf{q}(t_j) \quad (7.3)$$

Thus by rewriting the equation of motion

$$\begin{aligned} \mathbf{K}\mathbf{q}(t_j) + \mathbf{C}\dot{\mathbf{q}}(t_j) + \mathbf{M}\ddot{\mathbf{q}}(t_j) + \mathbf{f}_i(\mathbf{q}(t_j)) + \\ + \mathbf{f}_l(\mathbf{q}(t_j - \delta t), \mathbf{q}(t_j)) + \mathbf{f}_r(\mathbf{q}(t_j + \delta t), \mathbf{q}(t_j)) = \mathbf{p}(t_j) \end{aligned} \quad (7.4)$$

one can see that these equations differ for different sectors by the phase of the time variable only: once the solution is found, $\mathbf{q}(t)$, for one sector then it satisfies the equations for all the other sectors. [39]

Finally it has to be noted how the interface forces f_l and f_r are also actually linked by a relationship involving the phase shift

$$\mathbf{f}_r = \mathbf{f}_l(t + \delta t) \quad (7.5)$$

In literature, [12, 13], the correct mathematical description of the eigenvalue problem is presented: however, it can be seen that the conclusions drawn from the above observations are valid and the problem is indeed reduced to a description of the single sector, albeit dependent on the nodal diameters.

When studying the steady-state response to a periodic excitation, the harmonic balance method can be used: as the solution is also periodic, it is approximated by a truncated Fourier series to the first N_H harmonics [39]

$$\mathbf{q}(t) \approx \tilde{\mathbf{q}}_0 + \sum_{j=1}^{N_H} \left(\tilde{\mathbf{q}}_j^{(c)} \cos(m_j \omega t) + \tilde{\mathbf{q}}_j^{(s)} \sin(m_j \omega t) \right) \quad (7.6)$$

where $\tilde{\mathbf{q}}_j^{(c)}$, $\tilde{\mathbf{q}}_j^{(s)}$ are the cosine and sine coefficients of the j -th harmonic; while m_j is the specific number of the j -th harmonic.

The same relationship can be written in matrix form

$$\mathbf{q}(t) \approx (\mathbf{H}^T \otimes \mathbf{I}) \tilde{\mathbf{q}} \quad (7.7)$$

where $\tilde{\mathbf{q}} = \left\{ \tilde{\mathbf{q}}_0 \quad \tilde{\mathbf{q}}_1^{(c)} \quad \tilde{\mathbf{q}}_1^{(s)} \quad \dots \quad \tilde{\mathbf{q}}_{N_H}^{(c)} \quad \tilde{\mathbf{q}}_{N_H}^{(s)} \right\}^T$ is the vector containing the harmonic coefficients, while $\mathbf{H} = \left\{ 1 \quad \cos(m_1 \tau) \quad \sin(m_1 \tau) \quad \dots \quad \cos(m_{N_H} \tau) \quad \sin(m_{N_H} \tau) \right\}^T$ is a vector of harmonic functions with $\tau = \omega t$ and its Kronecker product with the identity matrix \mathbf{I} yields

$$\mathbf{H}^T \otimes \mathbf{I} = \left[\mathbf{I} \quad \cos(m_1 \tau) \mathbf{I} \quad \sin(m_1 \tau) \mathbf{I} \quad \dots \quad \cos(m_{N_H} \tau) \mathbf{I} \quad \sin(m_{N_H} \tau) \mathbf{I} \right] \quad (7.8)$$

In addition, cyclic symmetry constraints must also be applied in this case: it is convenient to partition the degrees of freedom as $\tilde{\mathbf{q}} = \{\tilde{\mathbf{q}}_l \ \tilde{\mathbf{q}}_i \ \tilde{\mathbf{q}}_r\}^T$, respectively left interface, internal and right interface DOFs. The constraints links the displacements of DOFs at the interfaces and for the harmonic coefficients they result in imposing [39]

$$(\mathbf{H}^T(\tau) \otimes \mathbf{I})\tilde{\mathbf{q}}_r = (\mathbf{H}^T(\tau + \varphi) \otimes \mathbf{I})\tilde{\mathbf{q}}_l \quad (7.9)$$

where φ is the IBPA.

The relationship between $\mathbf{H}(\tau)$ and the same matrix but shifted of φ is

$$\mathbf{H}(\tau + \varphi) = \text{diag} \left[1 \ \mathbf{t}_1 \ \dots \ \mathbf{t}_{N_H} \right] \mathbf{H}(\tau) \quad (7.10)$$

where

$$\mathbf{t}_j = \begin{bmatrix} \cos(m_j\varphi) & -\sin(m_j\varphi) \\ \sin(m_j\varphi) & \cos(m_j\varphi) \end{bmatrix}$$

So, by applying the cyclic symmetry constraints the number of degrees of freedom is reduced to internal DOFs and the ones laying on one of the two interfaces. [39]

$$\begin{aligned} \begin{Bmatrix} \tilde{\mathbf{q}}_l^{(c)} \\ \tilde{\mathbf{q}}_i^{(c)} \\ \tilde{\mathbf{q}}_r^{(c)} \\ \tilde{\mathbf{q}}_l^{(s)} \\ \tilde{\mathbf{q}}_i^{(s)} \\ \tilde{\mathbf{q}}_r^{(s)} \end{Bmatrix}_j &= \begin{bmatrix} \mathbf{I} & \mathbf{0} & \mathbf{0} & \mathbf{0} \\ \mathbf{0} & \mathbf{I} & \mathbf{0} & \mathbf{0} \\ \cos(m_j\varphi)\mathbf{I} & \mathbf{0} & -\sin(m_j\varphi)\mathbf{I} & \mathbf{0} \\ \mathbf{0} & \mathbf{0} & \mathbf{I} & \mathbf{0} \\ \mathbf{0} & \mathbf{0} & \mathbf{0} & \mathbf{I} \\ \sin(m_j\varphi)\mathbf{I} & \mathbf{0} & \cos(m_j\varphi)\mathbf{I} & \mathbf{0} \end{bmatrix} \begin{Bmatrix} \tilde{\mathbf{q}}_l^{(c)} \\ \tilde{\mathbf{q}}_i^{(c)} \\ \tilde{\mathbf{q}}_l^{(s)} \\ \tilde{\mathbf{q}}_i^{(s)} \end{Bmatrix}_j \\ &= \mathbf{G}_j \begin{Bmatrix} \tilde{\mathbf{q}}_l^{(c)} \\ \tilde{\mathbf{q}}_i^{(c)} \\ \tilde{\mathbf{q}}_l^{(s)} \\ \tilde{\mathbf{q}}_i^{(s)} \end{Bmatrix}_j \end{aligned} \quad (7.11)$$

However, the full finite element method is often reduced in size to a limited number of master DOFs as the harmonic balance method leads to a sharp increase in the size of the problem.

The procedure used in the project is based on the hybrid technique shown in Section 5.2: thus only a set of DOFs where the nonlinear forces are applied is retained and the dynamic compliance is approximated through mode shapes and a static correction. Therefore the residue of the reduced model is

$$\tilde{\mathbf{r}} = \tilde{\mathbf{q}}_n - \left[\mathbf{A}_{nn}^0 + \tilde{\mathbf{A}}_{nn}(\omega) \right] (\mathbf{P}_n - \mathbf{F}(\tilde{\mathbf{q}}_n)) = \tilde{\mathbf{q}}_n - \mathbf{A}_n(\omega)(\mathbf{P}_n - \mathbf{F}(\tilde{\mathbf{q}}_n)) = \mathbf{0} \quad (7.12)$$

Thus, after applying the constraint, the residue becomes

$$\tilde{\mathbf{r}} = \mathbf{G}\tilde{\mathbf{q}}_{n,red} - \mathbf{G}^T \mathbf{A}_n(\omega)(\mathbf{P}_n - \mathbf{F}(\tilde{\mathbf{q}}_n)) = \mathbf{0} \quad (7.13)$$

where $\mathbf{G} = \text{diag} [\mathbf{G}_0 \ \mathbf{G}_1 \ \dots \ \mathbf{G}_{N_H}]$, $\tilde{\mathbf{q}}_{n,red}$ is the vector containing only internal and left nonlinear DOFs, while \mathbf{P} and $\mathbf{F}(\tilde{\mathbf{q}}_n)$ are respectively the external and nonlinear forces.

It should be noted that the local contact formulation is however determined by the relative displacements, defined in a local contact reference frame in order to have a simpler contact description. They are defined as

$$\begin{aligned} \mathbf{w}(\tau) &= (\mathbf{H}^T(\tau) \otimes \mathbf{I})\mathbf{B}^T\tilde{\mathbf{q}}_r - (\mathbf{H}^T(\tau) \otimes \mathbf{I})\mathbf{B}^T\tilde{\mathbf{q}}_l = \\ &= (\mathbf{H}^T(\tau + \varphi) \otimes \mathbf{I})\mathbf{B}^T\tilde{\mathbf{q}}_l - (\mathbf{H}^T(\tau) \otimes \mathbf{I})\mathbf{B}^T\tilde{\mathbf{q}}_l \\ \tilde{\mathbf{w}} &= (\text{diag} [1 \ t_1 \ \dots \ t_{N_H}] - \mathbf{I})\mathbf{B}^T\tilde{\mathbf{q}}_l \end{aligned} \quad (7.14)$$

where \mathbf{B} is the transformation matrix from the global to local system of coordinates. Due to the model used, the cyclic symmetry of relative displacements and Newton's third law, the nonlinear contact forces on the right side can therefore be directly computed from the contact forces on the left one in the cyclic coordinate system. [40]

$$\mathbf{f}_r(\tau) = -\mathbf{f}_l(\tau + \varphi) \quad (7.15)$$

Hence why, in Equation (7.13), the entire residue is constrained with the \mathbf{G} matrix.

In addition, the relationship between the nonlinear forces in the global coordinates and local ones is [1]

$$\mathbf{F} = \mathbf{B}\mathbf{f}(\mathbf{B}^T\tilde{\mathbf{q}}) \quad (7.16)$$

7.2 Contact Model

At this point the contact model used has to be explicit as it determines the formulation of the nonlinear forces. These laws link the kinematics of the gap between the points with the local dynamics, i.e. the nonlinear forces that arise. Both pressure and force based formulations are available, the two being linked by the integral over the area. [1]

Also, it is worth to note that the geometry discretization can greatly affect the results obtained: in fact, while a relatively coarse discretization is sufficient to determine global vibrational quantities, a much finer local discretization is required to accurately resolve the contact stress field. [1]

Figure 7.1 shows several formulations that can be used for both normal and tangential descriptions: the choice of a rigid model over a compliant one may vary depending on the specific problem. This question, in turn, is mainly of mathematical nature, as it influences the solution method for the contact problem. Moreover the ODEs can be stiff if the contact model is stiff compared to the underlying structure stiffness, leading to an ill-conditioned problem: in this case a rigid model is not suggested, instead a linear penalization method is used; thus, from mathematical point of view, the problem becomes fully equivalent to the elastic formulation. [1]

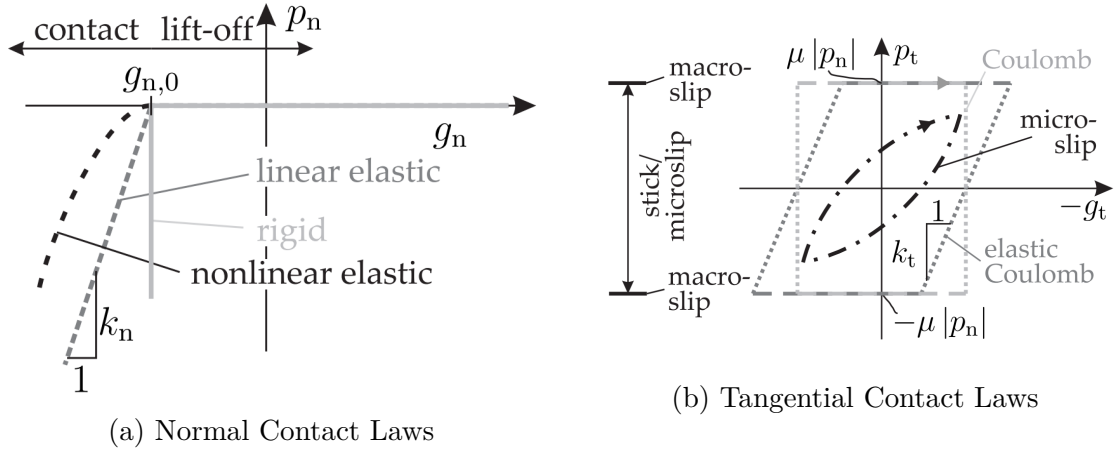


Figure 7.1: Friction Laws, [1]

However, it is important to remember that the choice of which law to use for the normal description and which one for the tangential motion cannot be unrelated, instead the two must be consistent.

So, if the *elastic Coulomb* model is used, the contact element can be schematised as in Figure 7.2. For sake of simplicity a 2D element is presented, but the approach can easily be extended to a 3D model. [see 40]

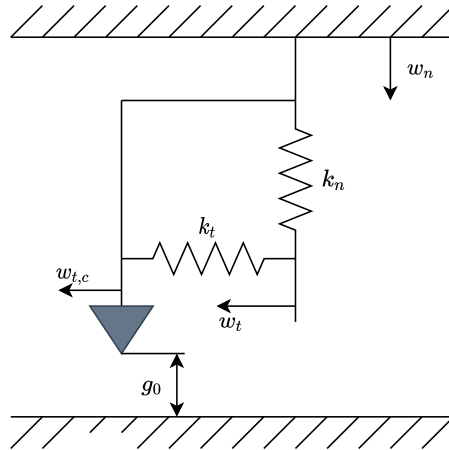


Figure 7.2: Contact Element

If a force based formulation is used, then the normal force is defined as

$$f_n = \begin{cases} 0 & g > 0 \text{ separation} \\ N_0 + k_n w_n(\tau) & g \leq 0 \text{ stick} \end{cases} \quad (7.17)$$

where g is the gap between the pair of contact nodes: an initial value $g_0 = -N_0/k_n$ can be prescribed by specifying a starting preload N_0 .

Meanwhile the tangential friction is defined as [41]

$$f_t = \begin{cases} 0 & \text{separation} \\ k_t(w_t - w_{t,c}) & \text{stick} \\ \mu F_n \operatorname{sgn}(w_{t,c}(\tau)) & \text{slip} \end{cases} \quad (7.18)$$

where $w_{t,c}$ is the relative displacement at the start of the stick phase and μ is the friction coefficient. A more in-depth description of the stick-slip transition and the criteria used to determine each state can be found in [42].

As it will be later explained during the AFT description, the nonlinear forces are determined in the time domain: thus the relative displacements are computed at N discrete points. So, once a stable description of the damper motion is captured, the $w_{t,c}$ at the l -th time point can be described as

$$w_{t,c}(l) = \begin{cases} w_t(l) & \text{separation} \\ w_{t,c}(l-1) & \text{stick} \\ w_t(l) - f_t(l)/k_t & \text{slip} \end{cases} \quad (7.19)$$

where

$$f_t(l) = \begin{cases} 0 & \text{separation} \\ f_t^p(l) & \text{stick} \\ \mu f_n \operatorname{sgn}(f_t^p(l)) & \text{slip} \end{cases} \quad (7.20)$$

is the tangential nonlinear force at the time instant l , with

$$f_t^p(l) = k_t(w_t(l) - w_{t,c}(l)) = k_t(w_t(l) - w_t(l-1)) + f_t(l-1)$$

7.3 Solution Technique

Cardona et al. [43] have proposed a general method to solve the nonlinear dynamic problem by alternating between time and frequency domain to take advantage of the ease with which nonlinear forces are evaluated in the time domain while capturing the periodic behaviour in the frequency domain. However, to use this method the following requirements have to be satisfied:

- Periodic loading;
- Solution assumed periodic.

In such cases, the solution \mathbf{q} can be sampled at N instants in the time domain

$$\mathbf{q}_l = \mathbf{q}(l\Delta t) \quad l = 0, \dots, N-1 \quad (7.21)$$

with $\Delta t = h = T/N$: $T = n_p \cdot T_f$ is the period of the analysis assumed to be n_p times the period of excitation T_f , allowing the search of sub-harmonics in the response.

Since the solution is periodic and sampled at N instants it can be expressed as a Fourier series

$$\mathbf{q}_l = \frac{1}{\sqrt{2N}} \left[\tilde{\mathbf{q}}_{0,0} + 2 \sum_{n=1}^{N/2-1} (C_{nl,0} \tilde{\mathbf{q}}_{n,0} + C_{nl,1} \tilde{\mathbf{q}}_{n,1}) + (-1)^k \tilde{\mathbf{q}}_{N/2,0} \right] \quad (7.22)$$

with $\tilde{\mathbf{q}}_{n,m}$ being the Fourier coefficients and $C_{nl,m}$ defined as

$$C_{nl,m} = \cos \left(\frac{2\pi n}{N} l - m \frac{\pi}{2} \right)$$

where m can be either 0 or 1, i.e. indicating the cosine and sine term respectively.

It should be noted that Equation (7.22) is equivalent to the inverse Fourier transform of $\tilde{\mathbf{q}}_{n,m}$, also denoted as

$$\mathbf{q}_l = \text{ift}_l^{n,m}(\tilde{\mathbf{q}}_{n,m}) \quad (7.23)$$

However, the actual number of harmonics N_H , needed to approximate the solution, is usually much smaller than N , therefore the Fourier expansion can be truncated to the N_H terms only

$$\begin{aligned} \mathbf{q}_l &= \sqrt{\frac{2}{N}} \left(\frac{1}{2} \tilde{\mathbf{q}}_{0,0} + \sum_{n=1}^{N_H} \sum_{m=0}^1 C_{nl,m} \tilde{\mathbf{q}}_{n,m} \right) \\ \dot{\mathbf{q}}_l &= \sqrt{\frac{2}{N}} \frac{2\pi}{T} \sum_{n=1}^{N_H} n (-C_{nl,0} \tilde{\mathbf{q}}_{n,0} + C_{nl,1} \tilde{\mathbf{q}}_{n,1}) \\ \ddot{\mathbf{q}}_l &= -\sqrt{\frac{2}{N}} \left(\frac{2\pi}{T} \right)^2 \sum_{n=1}^{N_H} n^2 (C_{nl,0} \tilde{\mathbf{q}}_{n,0} + C_{nl,1} \tilde{\mathbf{q}}_{n,1}) \end{aligned} \quad (7.24)$$

where $N_H < N/2 - 1$.

The local solution in time domain is obtained by imposing a null residue \mathbf{r}_l for every instant t_l

$$\mathbf{r}_l = \mathbf{M} \ddot{\mathbf{q}}_l + \mathbf{C} \dot{\mathbf{q}}_l + \mathbf{K} \mathbf{q}_l + \mathbf{F}(\mathbf{q}_l, \dot{\mathbf{q}}_l) - \mathbf{P}_l = \mathbf{0} \quad (7.25)$$

However an averaged form of dynamic equilibrium is often verified instead of the strong form of Equation (7.25) [43]

$$\tilde{\mathbf{r}}_{k,m} = \begin{cases} \frac{1}{2} \sqrt{\frac{2}{N}} \sum_{k=0}^{N-1} C_{kl,0} (\mathbf{M} \ddot{\mathbf{q}}_l + \mathbf{C} \dot{\mathbf{q}}_l + \mathbf{K} \mathbf{q}_l + \mathbf{F}(\mathbf{q}_l, \dot{\mathbf{q}}_l) - \mathbf{P}_l) & k = 0, m = 0 \\ \sqrt{\frac{2}{N}} \sum_{k=0}^{N-1} C_{kl,m} (\mathbf{M} \ddot{\mathbf{q}}_l + \mathbf{C} \dot{\mathbf{q}}_l + \mathbf{K} \mathbf{q}_l + \mathbf{F}(\mathbf{q}_l, \dot{\mathbf{q}}_l) - \mathbf{P}_l) & k = 1, 2, \dots, N_H \\ & m = 0, 1 \end{cases} \quad (7.26)$$

This equation differs only for the $\tilde{\mathbf{r}}_{0,0}$ coefficient of one half from the direct Fourier transform of \mathbf{r}_l , so it is convenient to refer to this relationship as

$$\tilde{\mathbf{r}}_{k,m} = \text{fft}_{k,m}^l(\mathbf{r}_l) = \text{fft}_{k,m}^l(\mathbf{r}(\mathbf{q}_l, \dot{\mathbf{q}}_l, \ddot{\mathbf{q}}_l(\tilde{\mathbf{q}}_{n,m}))) \quad (7.27)$$

In fact, when using the Newton-Raphson method to search the solution of the problem

$$\tilde{\mathbf{q}}_{nl}^{(p+1)} = \tilde{\mathbf{q}}_{nl}^{(p)} - \left[\frac{\partial \tilde{\mathbf{r}}(\tilde{\mathbf{q}}_{nl})}{\partial \tilde{\mathbf{q}}_{nl}} \right]^{-1} \tilde{\mathbf{r}}(\tilde{\mathbf{q}}_{nl}^{(p)}) \quad (7.28)$$

thus computing the Jacobian matrix of Equation (7.13)

$$\mathbf{J} = \frac{\partial \tilde{\mathbf{r}}}{\partial \tilde{\mathbf{q}}_{nl}} = \mathbf{I} + \mathbf{A}(\omega) \mathbf{J}_s \quad (7.29)$$

it becomes evident that only the tangent stiffness matrix \mathbf{J}_s has to be calculated

$$\mathbf{J}_s = \frac{\partial \tilde{\mathbf{F}}_{nl}}{\partial \tilde{\mathbf{q}}_{nl}} = \mathbf{B} \frac{\partial \tilde{\mathbf{f}}_{nl}}{\partial \tilde{\mathbf{w}}} \quad (7.30)$$

This means differentiating the nonlinear forces: the extension of the procedure to compute the tangent stiffness matrix outlined by Cardona et al. [43] has been extended to the case of nonlinear forces by Siewert et al. [41] and Afzal et al. [40]. Moreover, it is convenient to recall the derivative of the nonlinear forces with respect to a generic quantity x [1]

$$\frac{\partial \tilde{\mathbf{f}}_{nl}}{\partial x} = \text{fft} \left[\frac{\partial \mathbf{f}_{nl}}{\partial x} + \frac{\partial \mathbf{f}_{nl}}{\partial \mathbf{w}} \text{ift} \left[\frac{\partial \tilde{\mathbf{w}}}{\partial x} \right] + \frac{\partial \mathbf{f}_{nl}}{\partial \dot{\mathbf{w}}} \text{ift} \left[\frac{\partial \nabla \tilde{\mathbf{w}}}{\partial x} \right] \right] \quad (7.31)$$

In this particular case x is the relative displacement vector and the derivative results in

$$\frac{\partial \tilde{\mathbf{f}}_{nl}}{\partial x} = \text{fft} \left[\frac{\partial \mathbf{f}_{nl}}{\partial \mathbf{w}} \text{ift} \left[\frac{\partial \tilde{\mathbf{w}}}{\partial x} \right] \right] \quad (7.32)$$

The relationships between the time and frequency domain as well as the solution scheme can be summarized in a diagram such as the one of Figure 7.3.

The normal force is dependent only on the \tilde{w}_n displacement: thus the derivative of its k -th Fourier coefficient with respect to the cosine and sine h -th Fourier coefficient of the normal relative displacement are the only non zero derivatives

$$\begin{aligned} \frac{\partial \tilde{f}_n^{(k)}}{\partial \tilde{w}_{n,0}^{(h)}} &= \frac{1}{N} \sum_{l=0}^{N-1} \sum_{m=0}^1 \frac{\partial f_n(l)}{\partial w_n} C_{kl,m} \cos \left(\frac{2\pi h}{N} l \right) \\ \frac{\partial \tilde{f}_n^{(k)}}{\partial \tilde{w}_{n,1}^{(h)}} &= \frac{1}{N} \sum_{l=0}^{N-1} \sum_{m=0}^1 \frac{\partial f_n(l)}{\partial w_n} C_{kl,m} \sin \left(\frac{2\pi h}{N} l \right) \end{aligned} \quad (7.33)$$

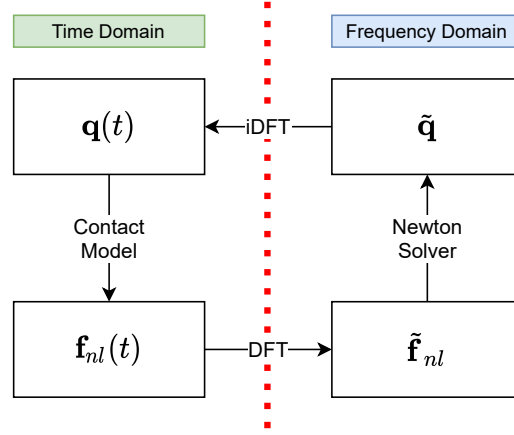


Figure 7.3: AFT Block Diagram

where the coefficient C is defined as

$$C_{kl,m} = \cos\left(\frac{2\pi k}{N}l - m\frac{\pi}{2}\right)$$

with $m = 0,1$ indicating either the cosine or the sine function.

Furthermore, Equation (7.33) also shows that the derivative can be computed as the FFT of the corresponding derivative formulated in the time domain multiplied by sine and cosine functions

$$\frac{\partial f_n(l)}{\partial \tilde{w}_{n,0}^{(h)}} = \begin{cases} 0 & \text{separation} \\ k_n \cos\left(\frac{2\pi h}{N}l\right) & \text{contact} \end{cases} \quad (7.34)$$

In a similar way the derivative of the tangential nonlinear forces can be computed: first with respect to the tangential relative displacements

$$\frac{\partial f_t(l)}{\partial \tilde{w}_{t,0}^{(h)}} = \begin{cases} 0 & \text{separation} \\ k_t \left(\cos\left(h\frac{2\pi}{N}l\right) - \cos\left(h\frac{2\pi}{N}(l-1)\right) \right) + \frac{\partial f_t(l-1)}{\partial \tilde{w}_{t,0}^{(h)}} & \text{stick} \\ 0 & \text{slip} \end{cases} \quad (7.35)$$

and also with respect to the normal relative displacements

$$\frac{\partial f_t(l)}{\partial \hat{w}_n} = \begin{cases} 0 & \text{separation} \\ \frac{\partial f_t(l-1)}{\partial \tilde{w}_{n,0}^{(h)}} & \text{stick} \\ \mu k_n \cos\left(h\frac{2\pi}{N}l\right) \text{sgn}(f_t^p) & \text{slip} \end{cases} \quad (7.36)$$

So the Jacobian matrix can be constructed as

$$\mathbf{J}_s = \begin{bmatrix} 1/2\tilde{\mathbf{K}}_{0,0} & \dots & \tilde{\mathbf{K}}_{h,0} & \tilde{\mathbf{K}}_{h,1} \\ \vdots & \ddots & \vdots & \vdots \\ \tilde{\mathbf{K}}_{k,0} & \tilde{\mathbf{K}}_{k+h,0} + \tilde{\mathbf{K}}_{k-h,0} & \tilde{\mathbf{K}}_{k+h,1} - \tilde{\mathbf{K}}_{k-h,1} \\ \tilde{\mathbf{K}}_{k,0} & \dots & \tilde{\mathbf{K}}_{k-h,1} + \tilde{\mathbf{K}}_{k+h,0} & \tilde{\mathbf{K}}_{k-h,0} - \tilde{\mathbf{K}}_{k+h,0} \end{bmatrix} \quad (7.37)$$

$$\mathbf{J}_s = \begin{bmatrix} \frac{\partial \tilde{f}_{n,0}^0}{\partial \tilde{w}_{n,0}^0} & \frac{\partial \tilde{f}_{n,0}^0}{\partial \tilde{w}_{n,1}^0} & \frac{\partial \tilde{f}_{n,0}^0}{\partial \tilde{w}_{t,0}^0} & \dots & \frac{\partial \tilde{f}_{n,0}^0}{\partial \tilde{w}_{t,0}^{NH}} & \frac{\partial \tilde{f}_{n,0}^0}{\partial \tilde{w}_{t,1}^{NH}} \\ \frac{\partial \tilde{f}_{n,1}^0}{\partial \tilde{w}_{n,0}^0} & \frac{\partial \tilde{f}_{n,1}^0}{\partial \tilde{w}_{n,1}^0} & \frac{\partial \tilde{f}_{n,1}^0}{\partial \tilde{w}_{t,0}^0} & \dots & \frac{\partial \tilde{f}_{n,1}^0}{\partial \tilde{w}_{t,0}^{NH}} & \frac{\partial \tilde{f}_{n,1}^0}{\partial \tilde{w}_{t,1}^{NH}} \\ \vdots & \vdots & \vdots & \ddots & \vdots & \vdots \\ \frac{\partial \tilde{f}_{n,0}^{NH}}{\partial \tilde{w}_{n,0}^0} & \frac{\partial \tilde{f}_{n,0}^{NH}}{\partial \tilde{w}_{n,1}^0} & \frac{\partial \tilde{f}_{n,0}^{NH}}{\partial \tilde{w}_{t,0}^0} & \dots & \frac{\partial \tilde{f}_{n,0}^{NH}}{\partial \tilde{w}_{t,0}^{NH}} & \frac{\partial \tilde{f}_{n,0}^{NH}}{\partial \tilde{w}_{t,1}^{NH}} \\ \frac{\partial \tilde{f}_{n,1}^{NH}}{\partial \tilde{w}_{n,0}^0} & \frac{\partial \tilde{f}_{n,1}^{NH}}{\partial \tilde{w}_{n,1}^0} & \frac{\partial \tilde{f}_{n,1}^{NH}}{\partial \tilde{w}_{t,0}^0} & \dots & \frac{\partial \tilde{f}_{n,1}^{NH}}{\partial \tilde{w}_{t,0}^{NH}} & \frac{\partial \tilde{f}_{n,1}^{NH}}{\partial \tilde{w}_{t,1}^{NH}} \\ \frac{\partial \tilde{f}_{n,1}^{NH}}{\partial \tilde{w}_{n,0}^0} & \frac{\partial \tilde{f}_{n,1}^{NH}}{\partial \tilde{w}_{n,1}^0} & \frac{\partial \tilde{f}_{n,1}^{NH}}{\partial \tilde{w}_{t,0}^0} & \dots & \frac{\partial \tilde{f}_{n,1}^{NH}}{\partial \tilde{w}_{t,0}^{NH}} & \frac{\partial \tilde{f}_{n,1}^{NH}}{\partial \tilde{w}_{t,1}^{NH}} \end{bmatrix} \quad (7.38)$$

7.3.1 Continuation Algorithm

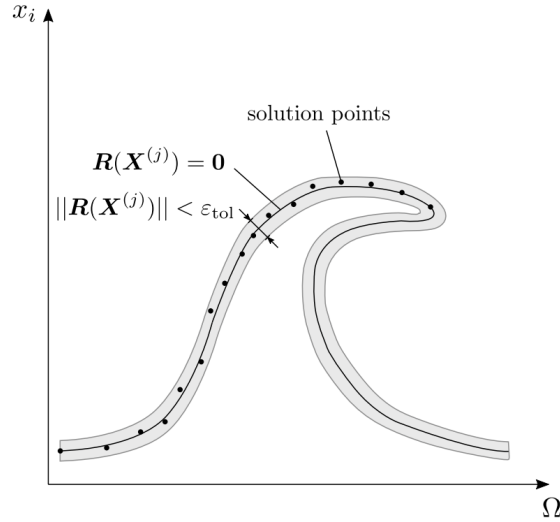


Figure 7.4: Solution Branch, [44]

Usually it is necessary to compute the response over frequency range, i.e. calculating the solution while varying the Ω parameter as in Figure 7.4. One idea might be choosing a sequence of frequency points $\Omega_1 < \Omega_2 < \dots$ at which the local solution is computed. Here it is important to recall that this local solution method

requires a good initial guess. Thus, a possible strategy could be taking the solution for one frequency point as initial guess for the next: however, in cases where the solution has turning points with respect to the free parameter, the solver might fail to converge or require too many iterations to reach a solution. [45]

In fact, the Newton-Raphson iteration, defined in (7.28), fails to converge around the turning point since the Jacobian matrix is close to singular. Therefore, a predictor-corrector continuation method is used in order to avoid the convergence problem: thus the system of equations is augmented with an additional constraint equation. [40]

In the following steps the “pseudo-arc length” method, see Figure 4.3, will be presented: albeit not the only possibility, this is the method later used in the numerical analysis in FORSE.

Predictor Step

Let $M_{(i)}$ be a point satisfying $\mathbf{r}(\mathbf{q}_{(i)}, \Omega_{(i)}) = \mathbf{0}$: the goal is to compute $M_{(i+1)}$, a point that satisfies $\mathbf{r}(\mathbf{q}_{(i+1)}, \Omega_{(i+1)}) = \mathbf{0}$; where $\mathbf{q}_{(i+1)} = \mathbf{q}_{(i)} + \Delta\mathbf{q}_{(i)}$ and $\Omega_{(i+1)} = \Omega_{(i)} + \Delta\Omega_{(i)}$. [31]

During the prediction step an initial guess for the solution at the next value of Ω is made: in particular the guess will lie in a direction tangent to the solution branch.

The solution at the next point can be approximated as [31]

$$\underbrace{\mathbf{r}(\mathbf{q}_{(i+1)}, \Omega_{(i+1)})}_{=\mathbf{0}} \approx \underbrace{\mathbf{r}(\mathbf{q}_{(i)}, \Omega_{(i)})}_{=\mathbf{0}} + \Delta\mathbf{q}_{(i)} \left. \frac{\partial \mathbf{r}}{\partial \mathbf{q}} \right|_{M_{(i)}} + \Delta\Omega_{(i)} \left. \frac{\partial \mathbf{r}}{\partial \Omega} \right|_{M_{(i)}} \quad (7.39)$$

while the norm of the tangent vector $\mathbf{e}_{(i)} = \{\Delta\mathbf{q}_{(i)} \quad \Delta\Omega_{(i)}\}^T$ is computed as

$$\|\mathbf{e}_{(i)}\|^2 = \Delta\mathbf{q}_{(i)}^T \Delta\mathbf{q}_{(i)} + \Delta\Omega_{(i)}^2 \quad (7.40)$$

Now if the norm is set at unity and $a_{(i)} = \Delta\Omega_{(i)}$ with $\Delta\mathbf{q}_{(i)} = a_{(i)}\Delta\hat{\mathbf{q}}_{(i)}$, then it is possible to determine the frequency variation

$$a_{(i)} = \pm \frac{1}{\sqrt{\Delta\hat{\mathbf{q}}_{(i)}^T \Delta\hat{\mathbf{q}}_{(i)} + 1}} \quad (7.41)$$

The sign is chosen so that the scalar product of two consecutive tangent vectors yields a positive value.

By substituting the newly defined relationships and imposing a null residue, Equation (7.39) becomes

$$\cancel{a_{(i)}}\Delta\hat{\mathbf{q}}_{(i)} \left. \frac{\partial \mathbf{r}}{\partial \mathbf{q}} \right|_{M_{(i)}} + \cancel{a_{(i)}} \left. \frac{\partial \mathbf{r}}{\partial \Omega} \right|_{M_{(i)}} = \mathbf{0} \quad \Rightarrow \quad \Delta\hat{\mathbf{q}}_{(i)} \left. \frac{\partial \mathbf{r}}{\partial \mathbf{q}} \right|_{M_{(i)}} = - \left. \frac{\partial \mathbf{r}}{\partial \Omega} \right|_{M_{(i)}} \quad (7.42)$$

Thus it is possible to compute $\Delta \hat{\mathbf{q}}_{(i)}$ first, then $a_{(i)}$ and finally $\mathbf{e}_{(i)}$.

Once the tangent vector is computed, the prediction is made [31]

$$\mathbf{q}_{(i+1)}^{(0)} = \mathbf{q}_{(i)} + \Delta s_{(i)} \cdot \mathbf{e}_{(i)} \quad (7.43)$$

where $\mathbf{q}_{(i+1)}^{(0)}$ is the initial guess for the local solution at next Ω , while $\Delta s_{(i)}$ is the step size.

Corrector Step

As it is only an initial guess, the prediction often does not satisfy the equilibrium: therefore an iteration is performed until the residue is not zero. The generic k -th iteration is equal to

$$\underbrace{\mathbf{r}(\mathbf{q}_{(i+1)}^{(k)}, \Omega_{(i+1)}^{(k)})}_{\mathbf{r}^{(k)}} = \mathbf{q}_{(i+1)}^{(k)} - \mathbf{A}_n(\Omega_{(i+1)}^{(k)})(\mathbf{P} - \mathbf{F}(\mathbf{q}_{(i+1)}^{(k)})) \quad (7.44)$$

Thus, if a Newton scheme is used and since each iteration is forced to be orthogonal to the tangent vector \mathbf{e} , the system that has to be solved is [31]

$$\begin{bmatrix} \frac{\partial \mathbf{r}^{(k)}}{\partial \mathbf{q}} & \frac{\partial \mathbf{r}^{(k)}}{\partial \Omega} \\ \Delta \hat{\mathbf{q}}_{(i)}^T & \Delta \Omega_{(i)} \end{bmatrix} \begin{Bmatrix} \Delta \hat{\mathbf{q}}^{(k+1)} \\ \Delta \Omega^{(k+1)} \end{Bmatrix} = \begin{Bmatrix} -\mathbf{r}^{(k)} \\ \mathbf{0} \end{Bmatrix} \quad (7.45)$$

where \mathbf{q} and Ω are updated after each iteration.

In this chapter, it was shown how to compute the forced response to a periodic excitation of a tuned bladed disc starting from the finite element model of a single sector.

First, it was seen which boundary conditions are to be imposed due to cyclic symmetry. Subsequently the large model was reduced to only a few degrees of freedom for reasons of computational efficiency: in fact, the harmonic balance method, used to perform the nonlinear analysis, determines an increase in DOFs equal to twice the number of the selected harmonics.

Furthermore the contact element formulation has been explained as well as the AFT scheme used to compute the local solution with the Newton-Raphson method. Finally one predictor-corrector solution technique has been presented as this is an optimal method when computing a solution with turning points as the Newton one fails to converge in these cases.

This chapter therefore concludes the discussion of the theoretical aspects behind the simulation of the bladed discs forced response: in the next one the results obtained from a test case provided by SAFRAN will be presented and discussed.

Chapter 8

Numerical Analysis of a Bladed Disc

In this chapter, a *numerical analysis* of a bladed disc, consisting of **24 sectors**, is carried out following the HCF verification guidelines: starting with the creation of a 3D mesh of the fundamental sector up to the forced response, passing through modal analysis and the model order reduction.

In addition, multiple sensitivity analyses of the forced response were carried out to observe how different parameters affect the response level.

For the static and modal analysis as well as the MOR, the free FEM software CalculiX [25] was initially used, and the results were then validated both with SC03, a proprietary software of Rolls-Royce, and with ANSYS. For the forced response, a comparison of the results was made between the software developed by Imperial College of London, FORSE, and the one developed by the Politecnico di Torino. Finally, MATLAB and Python were used for general post-processing.

8.1 Model Properties

The fundamental sector, provided by SAFRAN, has been meshed in SALOME with **quadratic tetra elements**, as shown in Figure 8.2. An important feature of the mesh created is to have the side faces of the disc and shroud **symmetrical**: in fact this is a necessary condition to apply cyclic symmetry to the sector. This is due to the fact that, in the cyclic repetition of the sector, the right and left faces are constrained in a similar way to contact and, therefore, the distribution of the nodes on the two must be the same.

As far as the material is concerned, it was decided to use standard titanium, see Table 8.2, modelling only the elastic behaviour, i.e. assuming the absence of plastic phenomena.

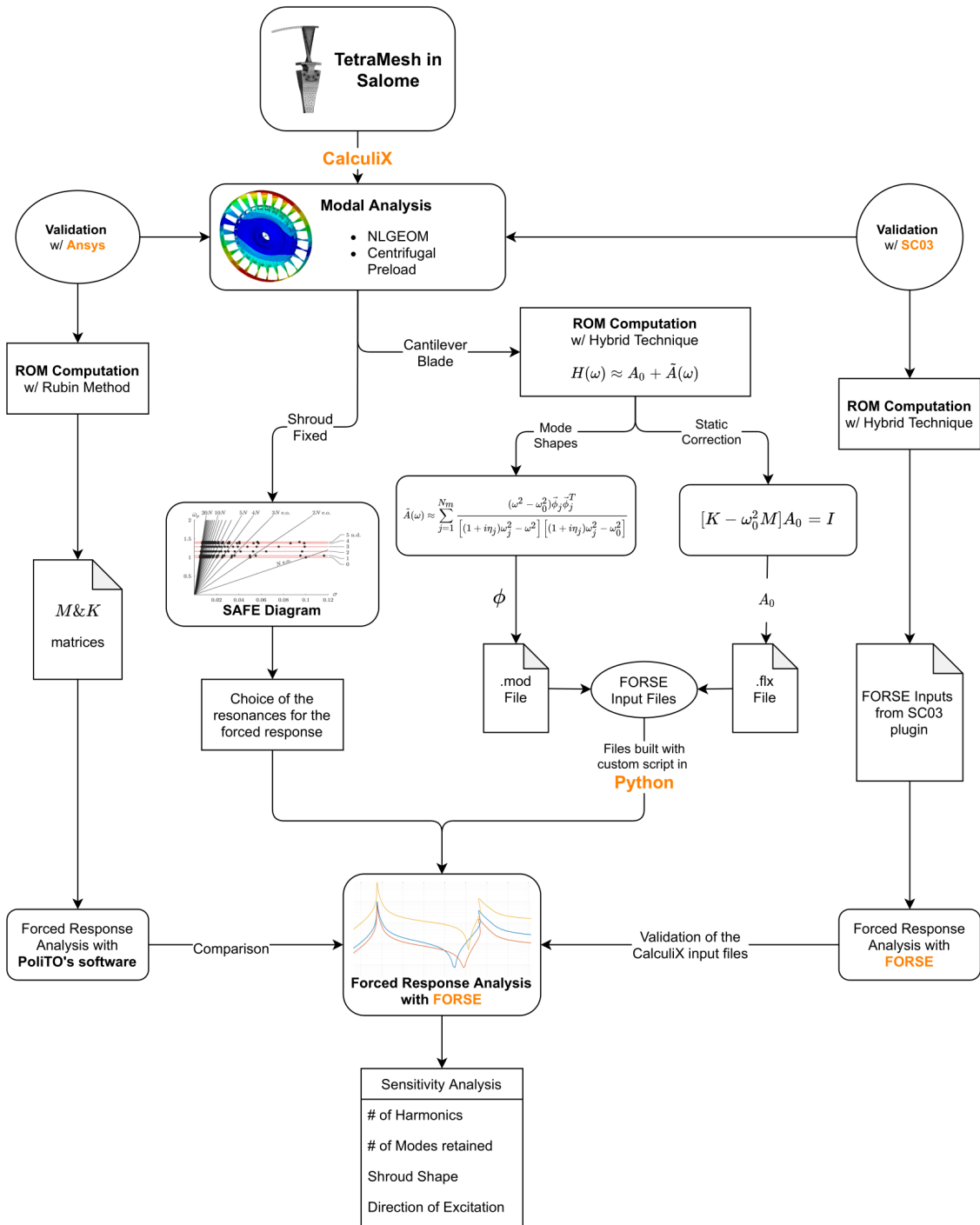
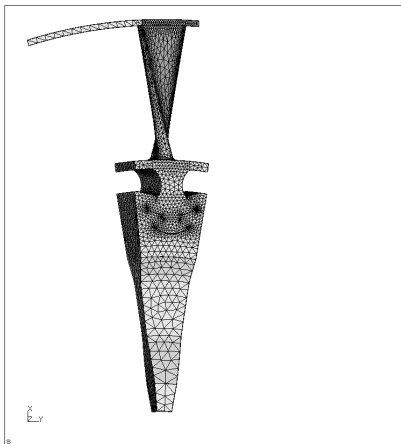
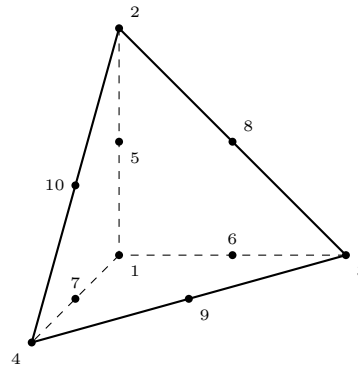


Figure 8.1: Analysis Outline

Moreover, initially all analyses were carried out enabling the **geometric nonlinearities**: a verification of its effect is then studied later on.



(a) Meshed Sector



(b) C3D10, Quadratic Tetra Element

Figure 8.2: FE Model

Element Type	N° of Elements	N° of Nodes	DOFs
C3D10	74470	118725	356 175

Table 8.1: Mesh Properties

8.1.1 Boundary Conditions

First and foremost, the inner ring of the disc is fixed in such a way as to replicate a *reference system integral* with the disc. Moreover, the cyclic symmetry hypothesis has also been used: a first case, see Figure 8.3b, where the boundary conditions have been **applied only to the disc** leaving free the shroud, i.e. obtaining a cantilever blade configuration, will be used to generate the reduced model. While a second case, Figure 8.3c, where **the boundary conditions include the shroud**, is analysed to produce the Diagrams useful for the identification of the resonances. With cyclic symmetry, one of the side surfaces is considered as the master and the other as the slave leading to neglect the degrees of freedom of the latter: the choice is purely arbitrary and does not affect the final outcome.

8.2 Static Loading

Subsequently a centrifugal load is applied to the model at different rotational speeds, $\Omega = 0 \rightarrow 10000$ rpm in order to be able to describe its behaviour in function of the latter. The reasons behind this static analysis are two: first of all it allows to estimate the mean stresses, necessary to construct the Goodman-Haigh diagram, acting on the assembly but it is also an expedient, as explained by Genta [23], used

	Young Modulus	Poisson's Ratio	Density
	[MPa]	[–]	[kg/mm ³]
Titanium	$1.16 \cdot 10^5$	0.34	$4.507 \cdot 10^{-9}$

Table 8.2: Standard Titanium Properties

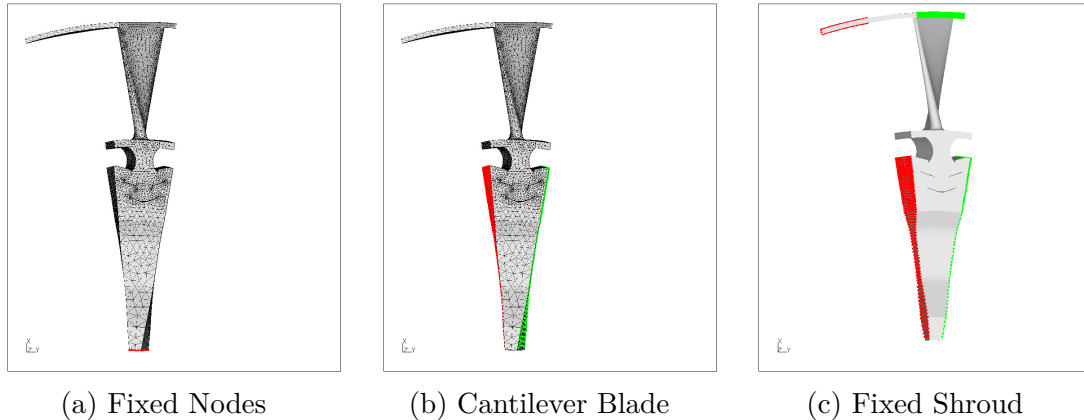


Figure 8.3: Boundary Conditions

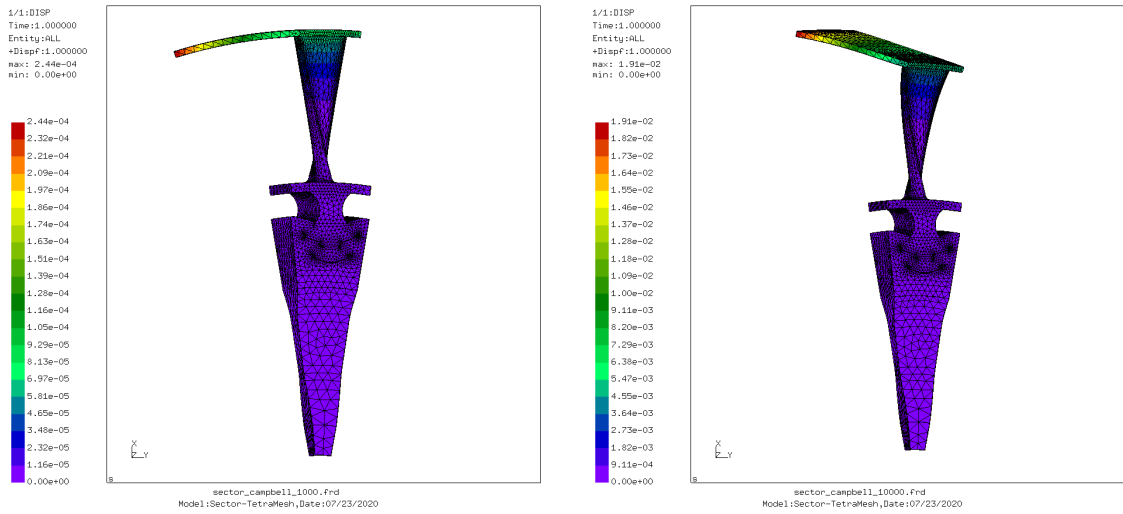
to take into account the centrifugal stiffening term of the stiffness matrix in the modal analysis as it is absent in the formulation of general purpose FEM software. In fact the results of this static analyses then represent the **initial condition** of the modal analyses which will lead to computing the **prestressed modes**.

Of the two configuration, it is clear that the second one is stiffer and rightfully so as it is more constrained. Furthermore, the cyclic symmetry hypothesis not only affects the amplitude of the displacements but also how their distribution: for the cantilever configuration the maximum is at the tip of the shroud, while for the fixed case it is right in the middle.

8.3 Modal Analysis

Then it was the turn of the modal analysis: each mode family is made up of 12 unique frequencies, equal to the maximum nodal diameter. Moreover, having performed them for each centrifugal load, it has been possible to observe the variation across the operating range.

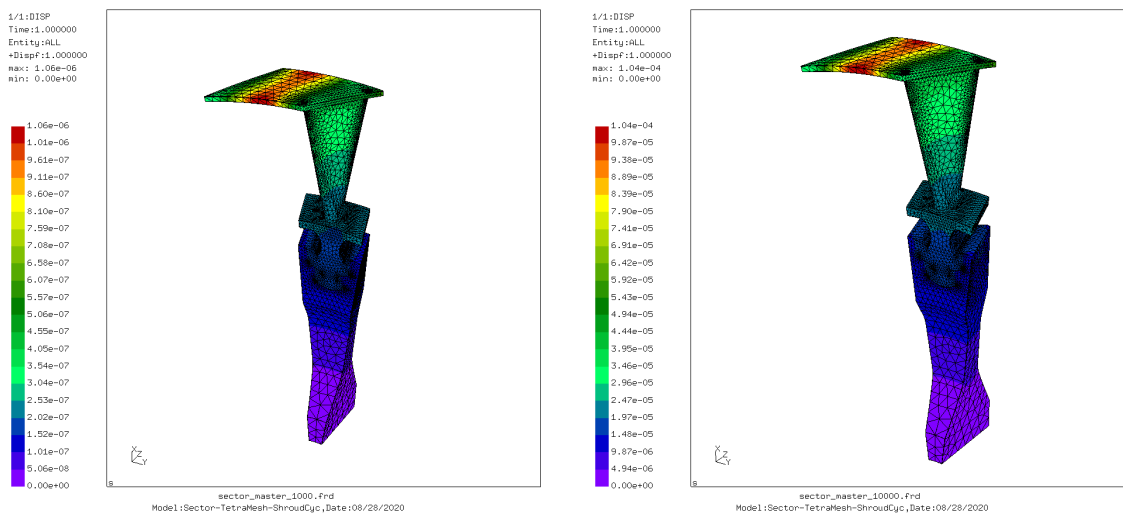
First, compare the plot in Figure ref of the frequency vs. nodal diameters obtained in the middle of the speed range at $\Omega = 5000$ rpm: again it is evident how the cantilever blade case is softer. Also it is possible to highlight the presence of the **frequency veering** phenomenon in the fixed shroud configuration.



(a) $\Omega = 1000$ rpm

(b) $\Omega = 10000$ rpm

Figure 8.4: Static Displacements of the Cantilver Blade



(a) $\Omega = 1000$ rpm

(b) $\Omega = 10000$ rpm

Figure 8.5: Static Displacements for Fixed Shroud

Besides determining different natural frequencies, the type of boundary conditions also greatly influences the mode shape itself: in Figure 8.7, showing the zero nodal diameter shape of the 1st mode family, it is possible to see that while the cantilever configuration shows a bending (1F) of the blade, the other shows a flapwise (FW) mode shape.

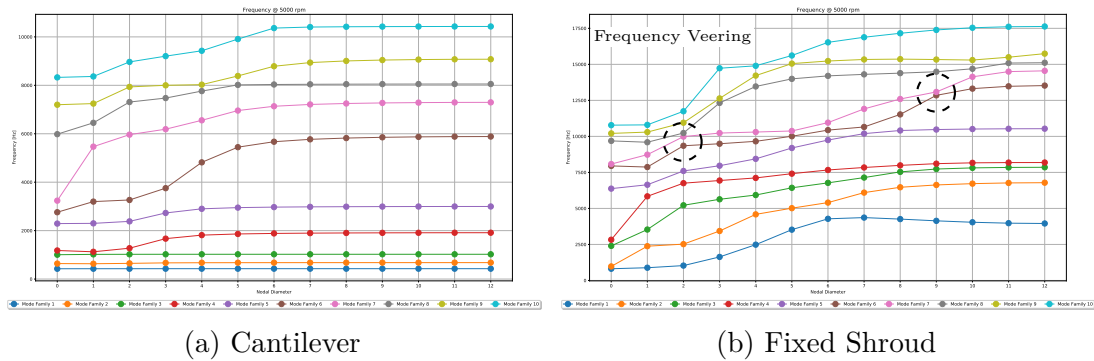


Figure 8.6: Frequency vs. ND @ $\Omega = 5000$ rpm

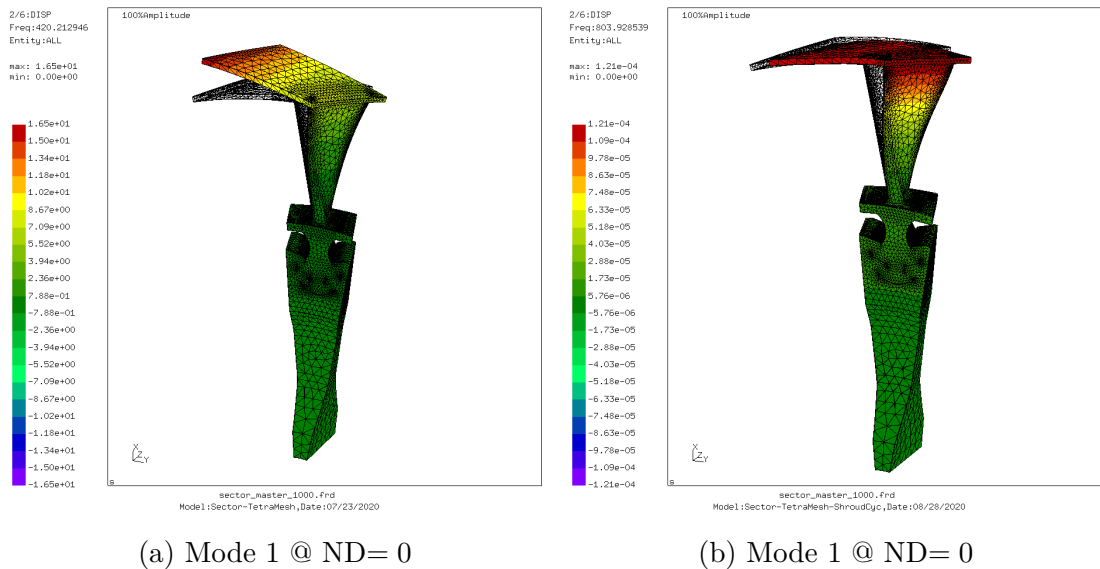


Figure 8.7: Mode Shape Comparison

8.3.1 SAFE Diagrams

The next step is to understand which mode shapes lead to resonances in the operating range: the tool used here is the SAFE diagram as it highlights only the true resonances compared to the much more crowded Campbell diagram. Furthermore only the fixed shroud case is here analysed as it is considered more representative of the real behaviour, where the contact between the adjacent shrouds lead to a stiffer structure than a cantilever representation.

As usually only the lower modes are considered dangerous [10, 3], only the *first ten modes*, twenty if considering the double multiplicity, for each nodal diameter have been requested during the modal analysis.

Of these, only the first five are shown from Figure 8.8 to 8.12: where, on the

left, it is possible to see the SAFE diagram in which the various **engine order excitation** are represented with dashed lines, while the black dots indicate the true resonances, i.e. the intersections between the EO and the correct nodal diameters as per Table 2.1. Instead, on the right, the corresponding deformed shape for nodal diameter 0 are pictured.

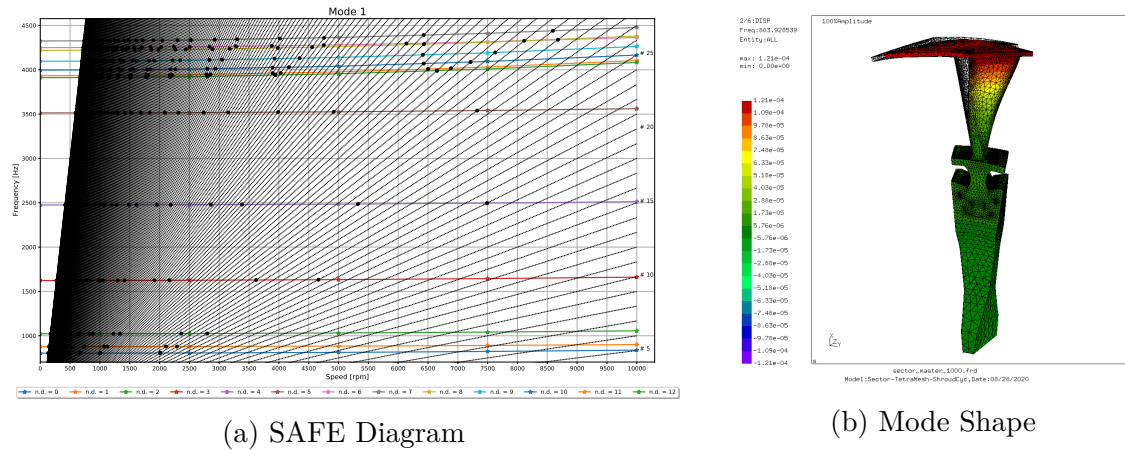


Figure 8.8: Mode #1 (FW)

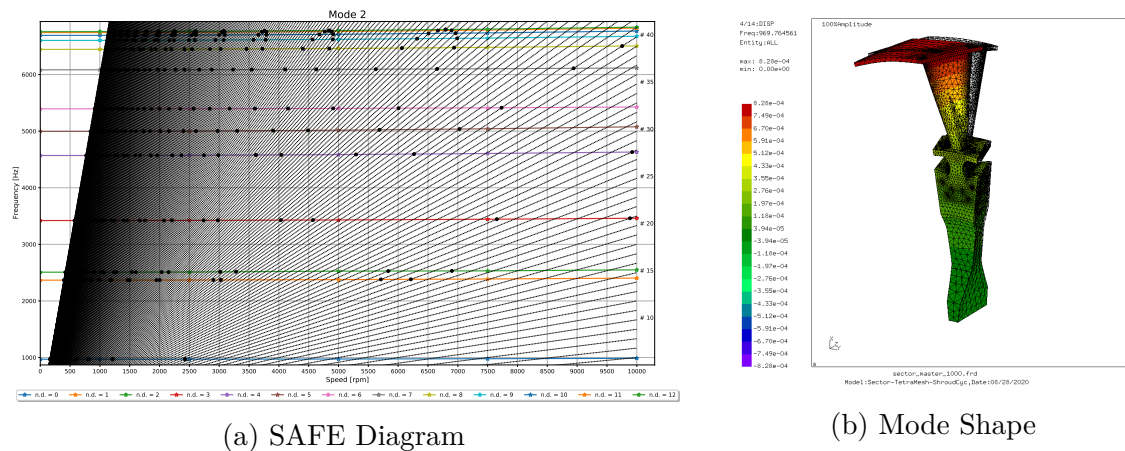


Figure 8.9: Mode #2 (1E)

8.3.2 Analysis Validation

In order to validate the results from CalculiX, a cross comparison of the first ten unique natural frequencies calculated in the modal analysis was made. The comparison involved two FEM software: Ansys and SC03, an in-house software of Rolls-Royce. In order to have a proper comparison of the results, the same mesh,

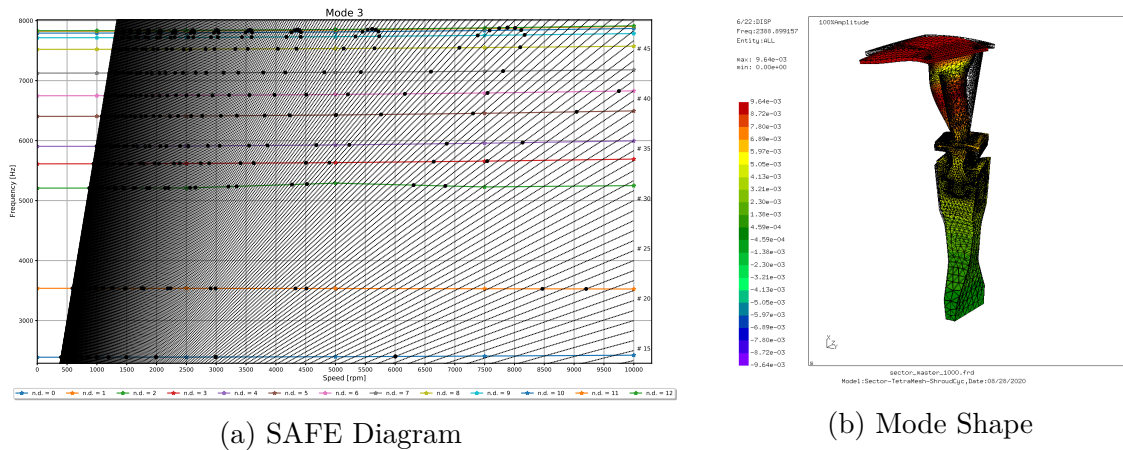


Figure 8.10: Mode #3 (“Mixed”)

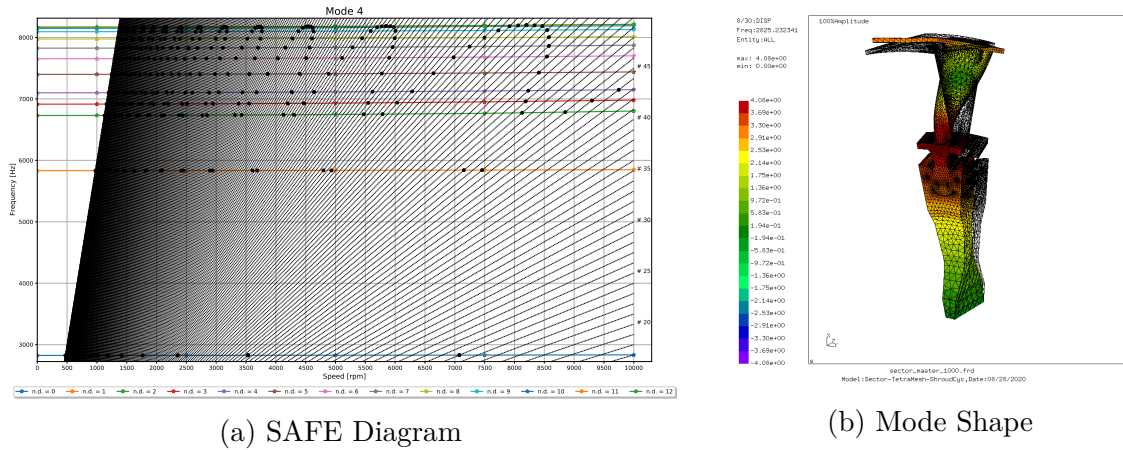


Figure 8.11: Mode #4 (“Mixed”)

the same material, the same boundary conditions and the same set-up were used, i.e. a first static analysis with centrifugal loading and geometric nonlinearities enabled followed by a modal analysis of the prestressed modes. Finally, a new study carried out in CalculiX, identical to the first one except for having disabled the geometric nonlinear formulation, was also compared.

Figure 8.13 shows the maximum difference, in percentage terms, observed with respect to the reference value obtained by CalculiX *fixed shroud* analysis when comparing the *first ten natural frequencies* for each nodal diameter. The maximum variation occurs at the second nodal diameter at speed $\Omega = 5000$ rpm: however, the peak corresponds to a mere 1.4%, demonstrating the validity of the results.

It should also be noted that the use of a formulation with or without geometric nonlinearities has *almost no effect* on the natural frequencies of the *fixed shroud*

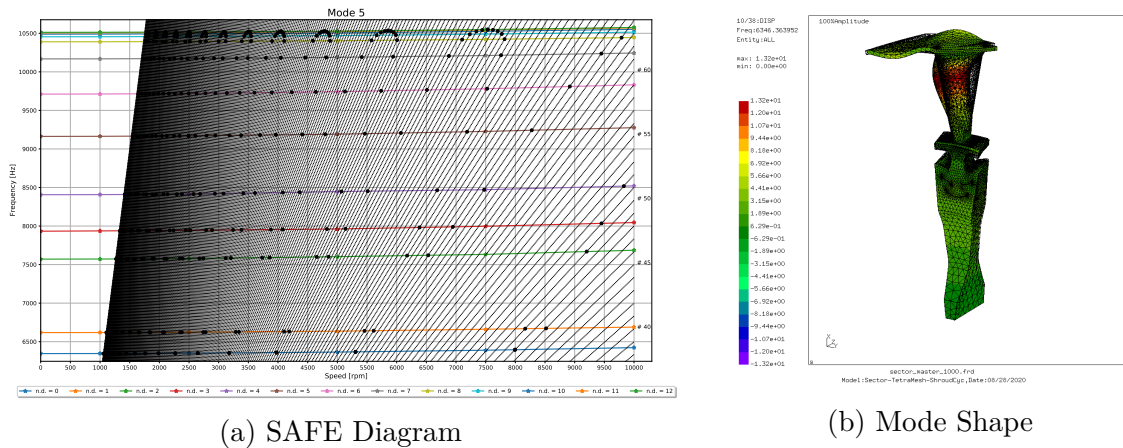


Figure 8.12: Mode #5 (1F)

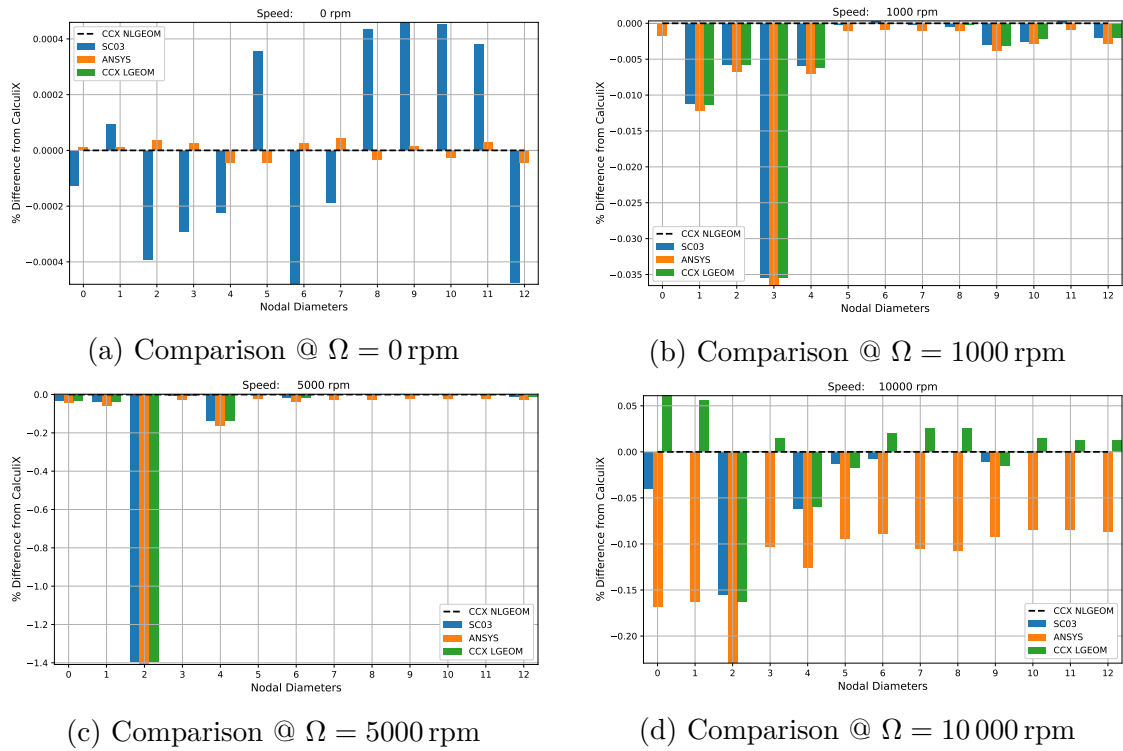
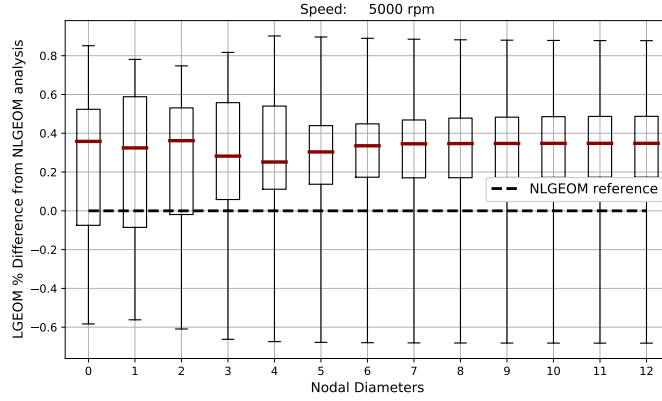


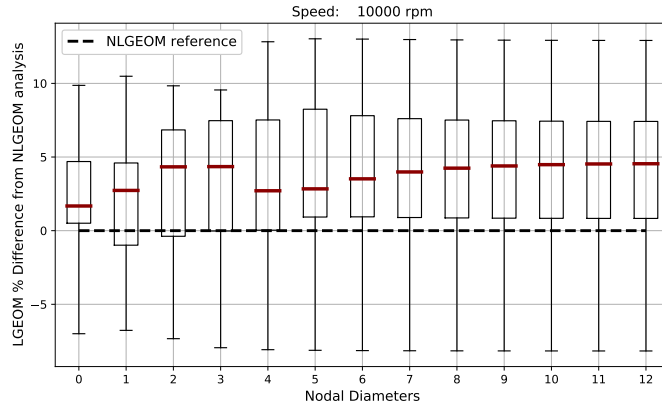
Figure 8.13: Fixed Shroud Frequencies Comparison

and indeed the range of variation is quite similar to that of results from Ansys and SC03.

It would be fair to ask whether it is necessary to use the NLGEOM parameter in simulations: Figure 8.13 would seem to suggest not, but if the cantilever configuration is analysed, the situation change. In fact Figure 8.14 shows that for the cantilever



(a) Comparison @ $\Omega = 5000$ rpm



(b) Comparison @ $\Omega = 10000$ rpm

Figure 8.14: Cantilever Frequencies Comparison

configuration, once a speed of $\Omega = 5000$ rpm is passed, the difference between turning NLGEOM on and having it off is not negligible at all.

Therefore, given that the reduced model is built from the cantilever configuration and that the MOR requires the computation of about a hundred mode shapes, the geometric nonlinearities ave to be considered.

8.4 Reduced Model

To create the reduced model, the hybrid method, discussed in Section 5.2, was used, given the fact that it is already implemented in FORSE and the ease with which the data can be obtained from CalculiX. In fact it requires only the *mode shapes of the nonlinear nodes*, coming from the cantilever modal analysis, while for the *static correction* is computed with the *Green Functions card* provided by CalculiX.

However, the first choice to make is which nodes should be kept and how many modes should be retained. The choice fell on 27 nodes on each side of the shroud and one in the centre of the blade where the force will be applied and the response measured.

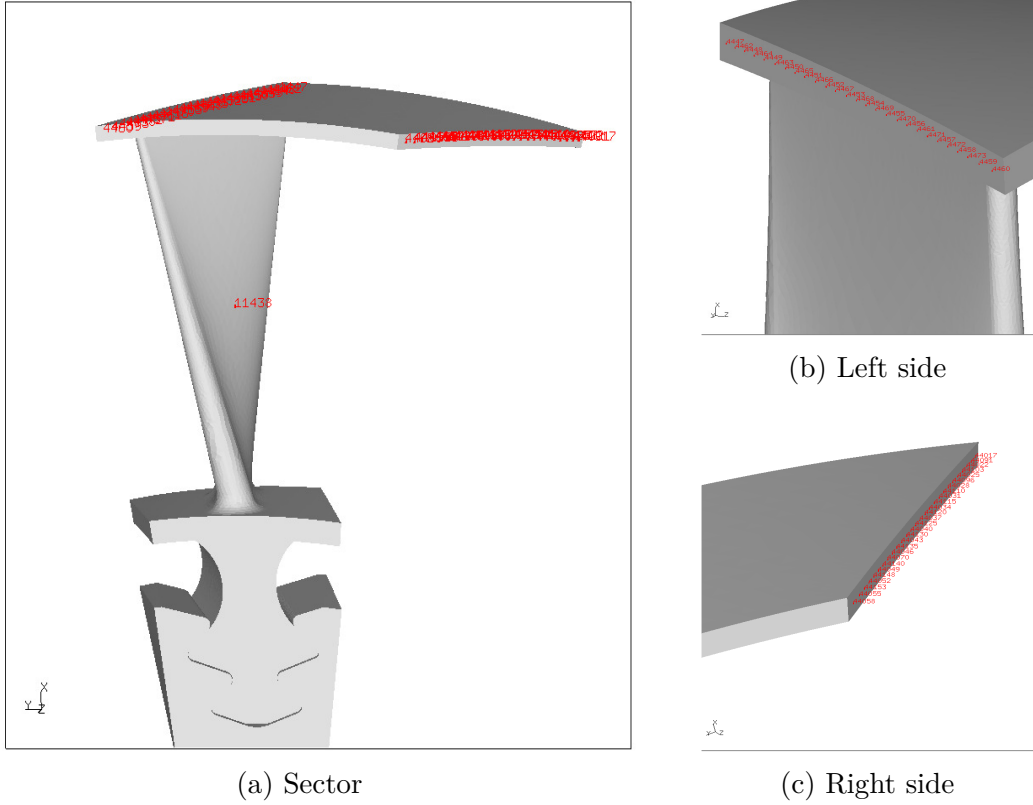


Figure 8.15: Nonlinear Nodes

The mode shapes of the nonlinear node set have been retrieved from the modal analysis with the command `*Node Print`, while to obtain the static correction matrix the `*Green` card have been used. This card allows to compute the Green Functions \mathbf{X}_j as follows

$$[\mathbf{K} - \omega_0 \mathbf{M}] \cdot \mathbf{X}_j = \mathbf{E}_j \quad (8.1)$$

where \mathbf{E}_j a unit force at degree of freedom j , which corresponds to a specific coordinate direction in a specific node. This calculation is then iterated for every nonlinear node, but always in the same direction requested in the `*Green` card. It is clear then that this coincides with Equation (5.28) if the damping factor is neglected. Also, this procedure can take into account the nonlinear behaviour if defined in the previous `*Static` step.

Furthermore, Appendix A.2 contains the input files with the routine used to generate the CalculiX outputs.

Selection	Value
N° of nonlinear nodes	55
N° of DOFs per node	3
N° of Modes Retained	100

Table 8.3: Reduced Model Properties

Once the results were obtained, they were post-processed with Python so as to correctly produce input files in the format required by FORSE. However, it is important to note that this procedure has been later validated in two steps by comparing:

1. results obtained with FORSE using the reduced model built from CalculiX result and the one obtained with SC03 routines;
2. mode shapes used to generate the input file from which the FRF matrix is estimated

Starting with the one to one comparison of the results, shown in Figure 8.16, of a nonlinear forced response, it is possible to notice that the two curves seem to coincide perfectly showing no differences.

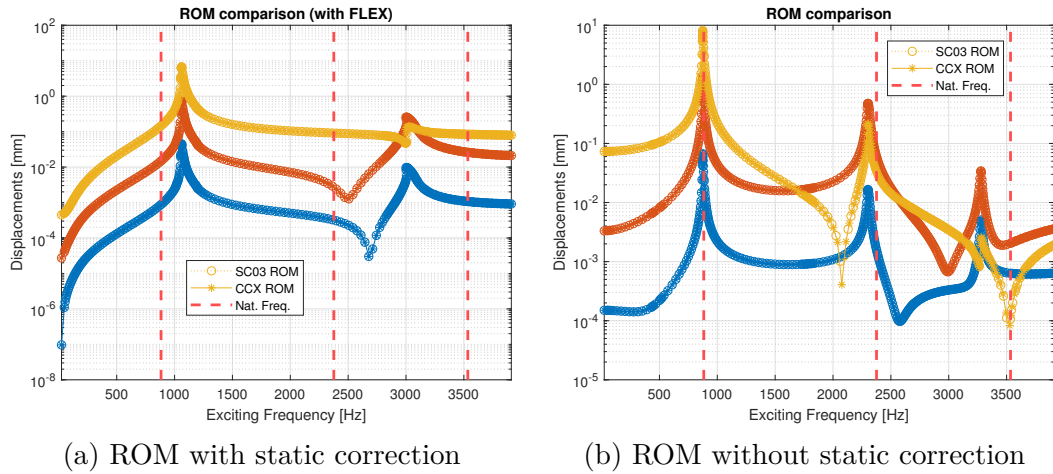


Figure 8.16: Comparison of the MOR (o for SC03, * for CalculiX)

As anticipated, in addition to comparing the response obtained with the two reduced models, also the mode shapes, used to compute the approximated frequency response function, were also compared: to compare the mode shapes, obtained with *CalculiX* and *SC03*, of the nonlinear node set the *Modal Assurance Criterion* is used

$$MAC(i, j) = \frac{|\boldsymbol{\psi}_{i,k}^T \boldsymbol{\phi}_{j,k}|^2}{(\boldsymbol{\psi}_{i,k}^T \boldsymbol{\psi}_{i,k})(\boldsymbol{\phi}_{j,k}^T \boldsymbol{\phi}_{j,k})} \quad (8.2)$$

where subscripts (i, j) indicate the i -th and j -th complex mode shape vectors along the k -th component of the global coordinate system, while $\boldsymbol{\psi}$ and $\boldsymbol{\phi}$ are used to reference the *SC03* and *CalculiX* modes respectively.

So the final result is a matrix whose size depends on the number of vectors compared: in this case a 1300×1300 matrix is obtained since for each nodal diameter 100 mode shapes have been retained. In particular the mode shapes have been ordered based on their nodal diameter: thus the first 100 corresponds to $ND = 0$, the next 100 to $ND = 1$ and so on.

The MAC takes value between 0 (representing a poor correspondence) and 1 (indicating a perfect match): usually values larger than 0.9 indicate a good enough correspondence, i.e. the mode shapes represent the same motion different only by a scalar or by a small quantity, whereas small values indicate poor resemblance of the two shapes. Moreover, it should be noted that even if the mode shapes are complex the value returned is real. [46]

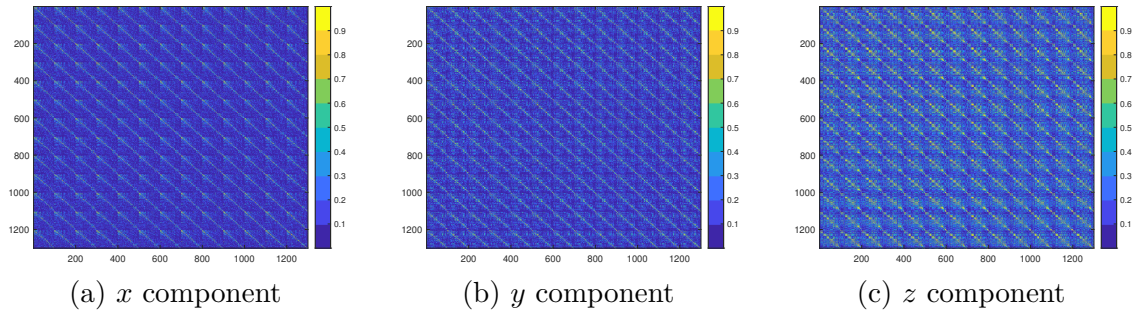
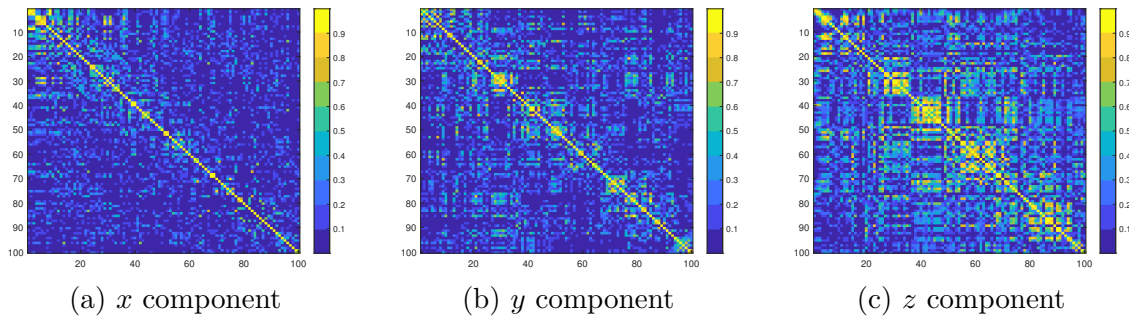
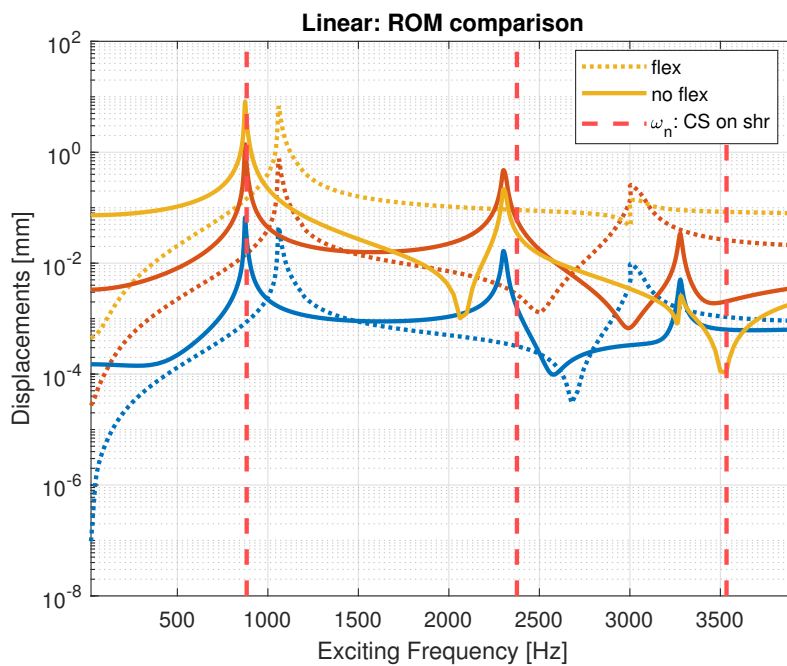


Figure 8.17: MAC: complex mode shapes

Figure 8.17 maps the MAC: a good match can be seen in the main diagonal, $MAC(i, i)$, in all three cases as the values are greater than 0.9. It is also interesting to note that a good correspondence can be seen on other diagonals: a pattern can be recognized as these diagonals are found by subsequent shifts of 100 places, like the number of the modes per nodal diameter, starting from the the main one.

A final verification observing where the peaks of a linear response for $EO = 23$, obtained by imposing a very high level of preload $N_0 = 10^9$ N, of the reduced order model lie compared to the natural frequencies computed with the modal analysis.

As shown in Figure 8.19, the behaviour of the reduced model with the static correction deviates greatly from what might be expected by comparing the position of the response peaks with the natural frequencies obtained from modal analysis. In addition, a response peak seems to be missing, whereas if the model without static contribution is considered, then, although there is a deviation in terms of frequency,


 Figure 8.18: MAC: comparison of $ND = 0$ mode shapes only

 Figure 8.19: Linear Response for $EO = 23$: analysis of static correction

its behaviour is much closer to what one would expect.

So a new modal analysis has been performed, but this time the cyclic symmetry boundary conditions have been applied only to the disc and to the nonlinear nodes of the reduced model lying on the shroud instead of the whole shroud surface. By looking at Figure 8.20, now the peaks are much closer in terms of frequency to the natural ones, however the ROM with the static contribution still misses a peak.

What can be observed is that the number of nodes chosen on the shroud affects the position of the peaks as it gives back a softer reduced model. Moreover the model without static correction seems a stiffer than the full model constrained only on the disc and nonlinear node set: this is somewhat expected as the static correction is meant to introduce flexibility, i.e. local compliance on the shroud nodes.

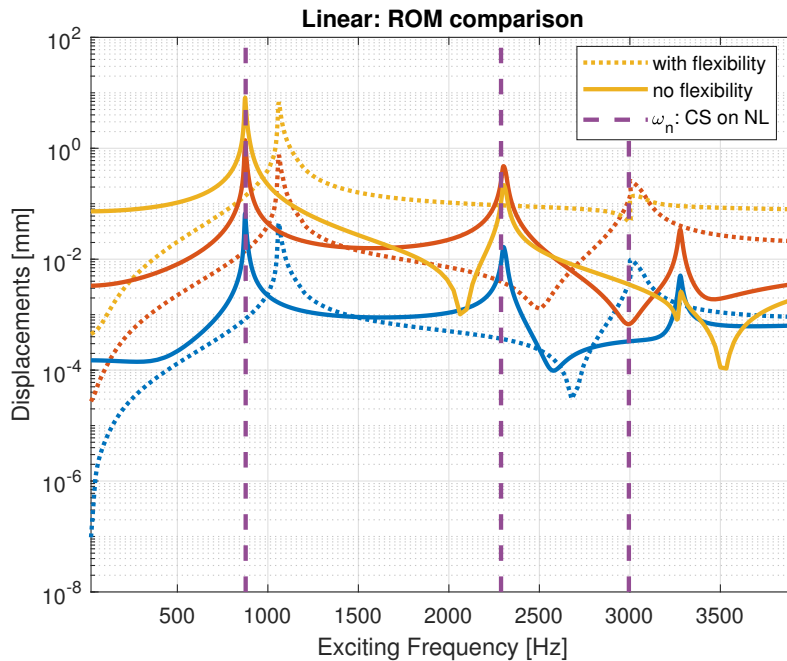


Figure 8.20: Linear Response for $EO = 23$: ω_n from modal analysis with CS only on disc and nonlinear node set only

As to the reduced model with the static correction a thorough investigation has to be conducted in order to understand whether there is a bug in the code or if an unexpected phenomenon appeared.

8.5 Forced Response

Having created the reduced model, now it is time to complete the model by defining the contact elements on the shroud sides.

To model a 3D friction contact a combination of two 2D contact elements, applied one perpendicular to the other, can be used. This approximation, as it treats the tangential forces independently, is conveniently used here because it allows to exploit the advantages of the 2D contact elements, such as computational efficiency and robustness of calculations, without compromising the accuracy.

A sort of hybrid contact element available in FORSE has been used: this element applies two 2D elements along the tangential directions, while excluding duplication of the normal force defined by these elements. Table 8.4 shows the properties assigned to the contact element: the chosen values for the stiffness and the friction have been mainly taken from what is suggested in literature. [see 47, 18, 48, 49]

As for the excitation, the force acts on the node at the blade centre along a direction that is parallel to the shroud side surface. Moreover the response has been

Property	Value
N° of contact elements	27
k_n [N/mm]	1×10^4
k_t [N/mm]	1×10^4
Area [mm ²]	2.398 976
Friction coefficient μ	0.4
Modal Damping Factor ζ	0.003

Table 8.4: FORSE Setup

measured at the same node.

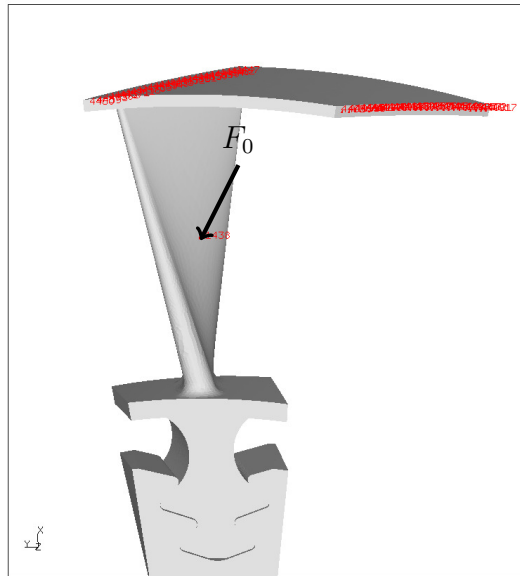


Figure 8.21: Force \parallel to z

8.5.1 EO Selection

As this particular shroud geometry lead to an impact type of problem, it lead to convergence issues: therefore to find an out of plane mode shape, thus maximising the excitation of the tangential sliding, a further CalculiX analysis in which the normal DOFs of the shroud sides where fixed while leaving the tangential DOFs free.

Then, by ordering the mode shapes based on their out of plane *modal participation factors* and looking at the SAFE diagrams, few engine orders were selected. Table 8.5 shows the engine orders that led to a nonlinear forced response and the excited

respective nodal diameter. Of these, only the first will be analysed in details in the

EO	ND
23	-1
45	-3
52	4

Table 8.5: EO vs. ND

following sections.

8.5.2 Engine Order 52

In order to capture the nonlinear forced response to the 52nd EO, the harmonic balance method has been used: the sub-harmonics components have been neglected as their contribution was negligible compared to the *super-harmonics* one.

It should be noted that the problem here analysed is **decoupled** as the harmonic 0 is not taken into account, thus only the problem is captured by the forced response while the static effect is neglected. This choice was made after encountering difficulties with convergence when studying the coupled problem: as expressed by Pesaresi et al. [50] while in the early stages this approach is acceptable, later on it is recommended to study the coupled problem as the harmonic “zero” term plays a key role in determining the dynamic response accurately, since the system response may show a great sensitivity to a change of the mean vibrating position.

For the reference case, the blade has been excited by 100 N, with a preload of 100 N assigned to the contact elements, i.e. assuming an interference between adjacent shrouds. It should be noted that the response amplitude of the DOF X_i

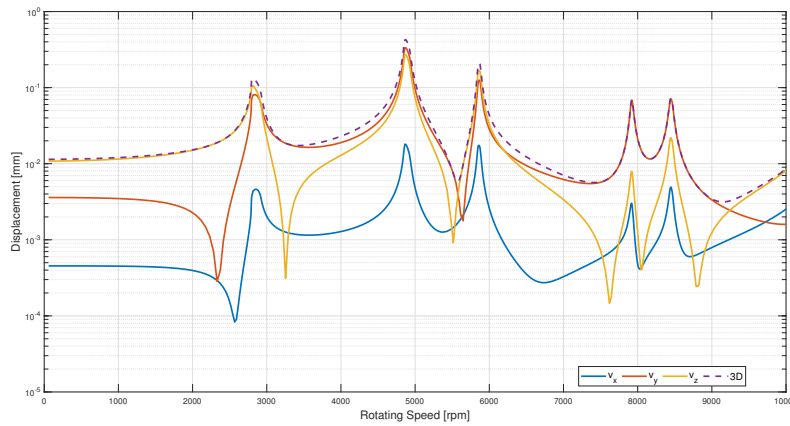


Figure 8.22: Nonlinear Forced Response ($EO = 52$, $N_0 = 100$ N, $F_0 = 100$ N, $H = 7$)

has been approximated as a summation of the harmonic cosine and sine coefficient

like

$$X_i = x_0 + \sum_{i=1}^H \sqrt{x_{c,i}^2 + x_{s,i}^2} \quad (8.3)$$

The response over the operating range, pictured in Figure 8.22, shows five peaks corresponding to the excitation of mode #1 to #5: with the biggest amplitude registered for mode #3. By looking at the simulation output at the first peak, it is possible to highlight a softening effect, i.e. the curve is leaning toward the left, due to the nonlinear behaviour, with a contribution coming mainly from the super-harmonics EO 104 & 156: even at the second peak a similar behaviour can be noted while for the rest of the response the system acts linearly.

However, to better observe the nonlinear behaviour of the system, the preload was reduced to 10 N. Figure 8.23 shows a much more pronounced nonlinearity

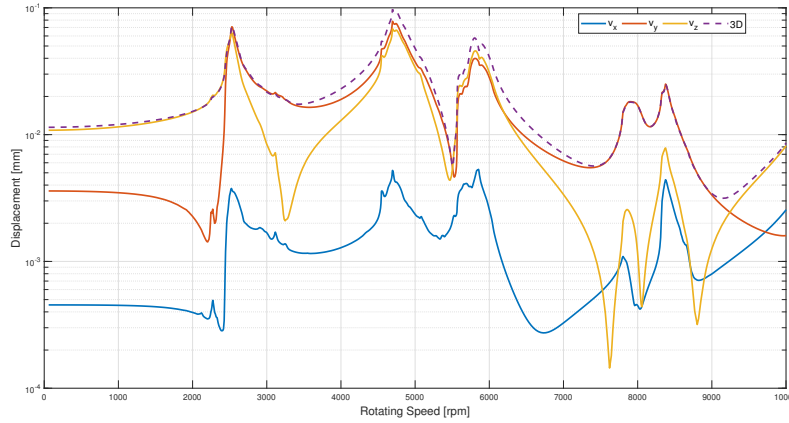


Figure 8.23: Nonlinear Forced Response ($EO = 52$, $N_0 = 10$ N, $F_0 = 100$ N, $H = 7$)

resulting from the contribution of super-harmonics: in addition to curves that are very different from the previous ones, the first peak is recorded at a lower speed. However, it must also be said that the response levels are lower because of the greater presence of nonlinearity: in fact, the friction due to the greater relative displacement between the shrouds of two adjacent sectors causes an increase in damping.

Clear evidence of how the contribution of super-harmonics is considerably stronger in the latter configuration with smaller preload can be seen in the Figure 8.24, where the steady state responses at the first peak of the two configurations are plotted.

As already explained the computed response with the harmonic balance method is periodic: moreover, it is quite evident the contribution of multiple harmonics for the system with smaller level of preload.

Before going on to carry out a sensitivity analysis of the system to the change of parameters in the simulation, it is worth checking that the number of harmonics used is sufficient as well as the number of mode shapes retained.

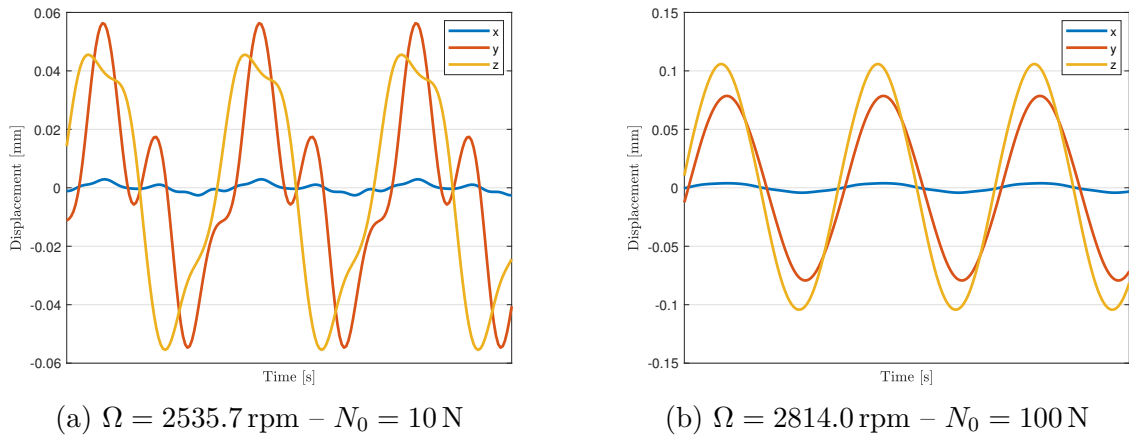

 Figure 8.24: Steady-state Response at 1st peak

Figure 8.25 shows almost no variation when looking at $N_0 = 100 \text{ N}$ study: $H = 1$ is enough to capture the dynamic behaviour of such system as the curves overlap perfectly. On the other hand, when dealing with a smaller preload as $N_0 = 10 \text{ N}$, the number of harmonics needed increase to $H = 5$: in fact if $H = 1$ then the predicted response will miss the important nonlinear contribution from the super-harmonics.

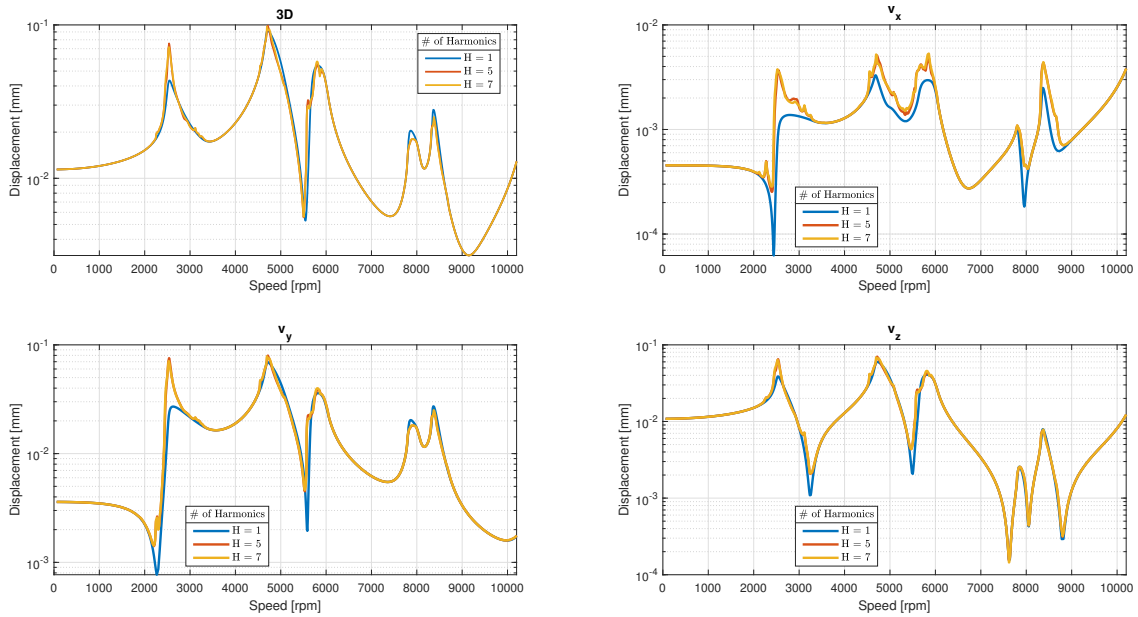
A final test has been done to check if the number of modes retained was enough to describe the system behaviour. Looking at Figure 8.26, it can be seen that both level of preloads, while it is clear that the curves are converging towards the 100 modes one, need all the modes retained to properly capture the system behaviour as even the difference between 75 modes used and 100 is not negligible. Albeit the level of the response decreases, it can be observed a softening of the system, i.e. the peaks moves left, as the number of modes used increases.

Moving on to sensitivity analyses: a very important one for the designer is to observe how the level of preload changes the response. A lower preload will increase the nonlinearity of the system as the surfaces slide a lot more and they are not stick any more. This is not necessarily a negative effect as increased work done by friction results in a more damped system. However it is fundamental to find the optimum preload, i.e. a balance in the middle of a high N_0 resulting in stick contact and $N_0 = 0 \text{ N}$ equivalent to open shroud.

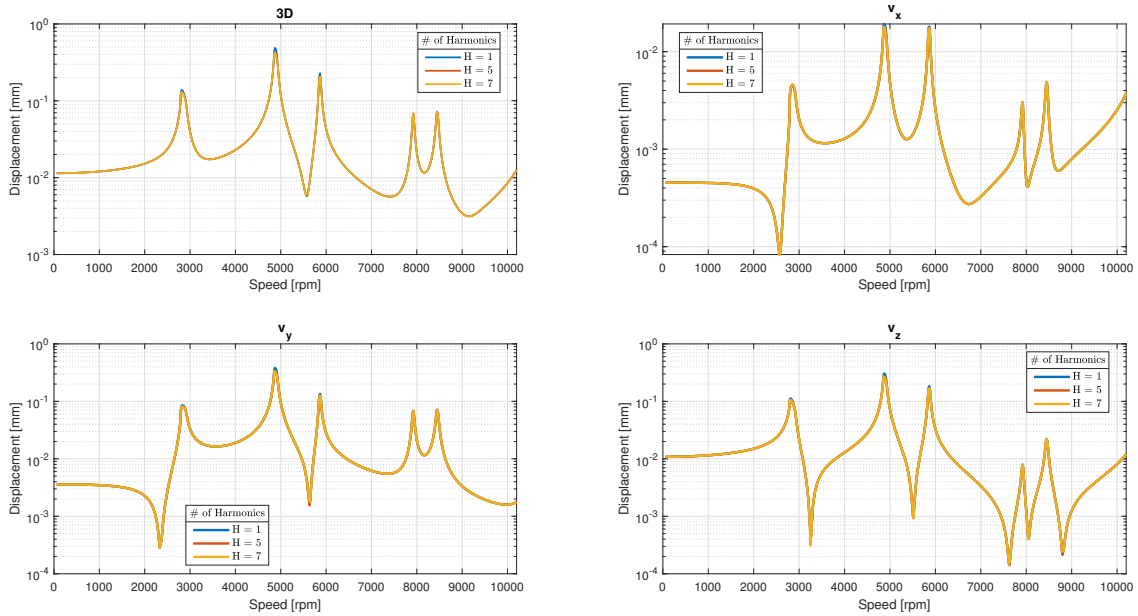
Figure 8.27 shows that by increasing the preload the assembly gets stiffer: the peak frequencies moves to the right but the maximum displacement increases as well, from the figure it is evident that for $N_0 = 10 \text{ N}$, while the system behaviour is much more nonlinear, the level of the response is minimized.

Subsequent sensitivity studies focus on the characteristics of the excitation: first the amplitude F_0 is varied, then the direction in which it acts.

In Figure 8.28 a comparison of the **receptance**, rather than the absolute displacements, obtained by different forcing level is shown: $F_0 = 10 \text{ N}$ return a similar



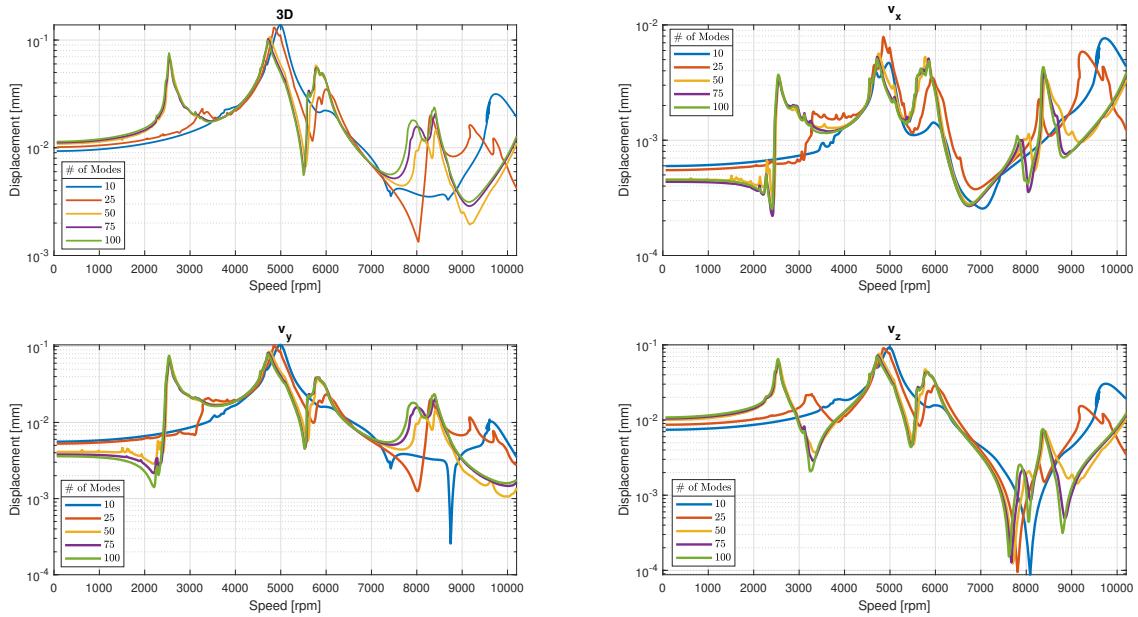
(a) $N_0 = 10\text{ N}$



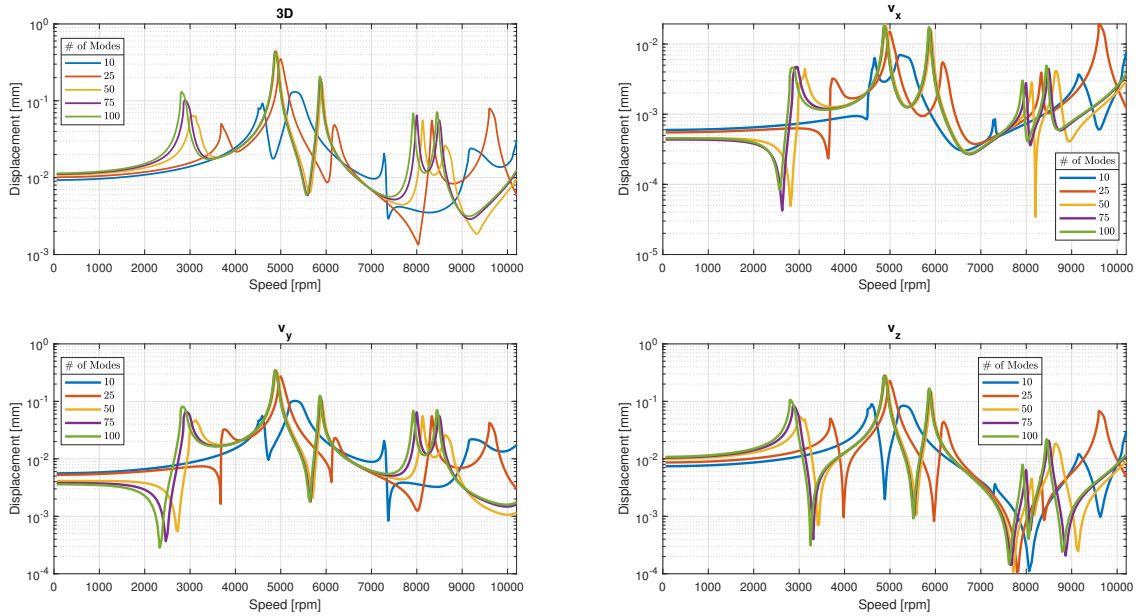
(b) $N_0 = 100\text{ N}$

Figure 8.25: Choice of the Harmonics

curve to $F_0 = 100\text{ N}$, while for higher level a softening effect is experienced, i.e. the peaks move to the left. In particular $F_0 = 1000\text{ N}$ shows a more pronounced nonlinearity across the first three peaks and, similarly to what was experience in Figure 8.27 for $N_0 = 10\text{ N}$, the level of the receptance decreases as the nonlinearity



(a) $N_0 = 10\text{ N}$



(b) $N_0 = 100\text{ N}$

Figure 8.26: Modes Retained

introduces a damping effect on the system.

Two new directions of the excitation have been studied: in one the force is parallel to the global y axis, in the other is parallel to z . The results show that the direction of the force does not have a negligible effect in the response level: a big difference

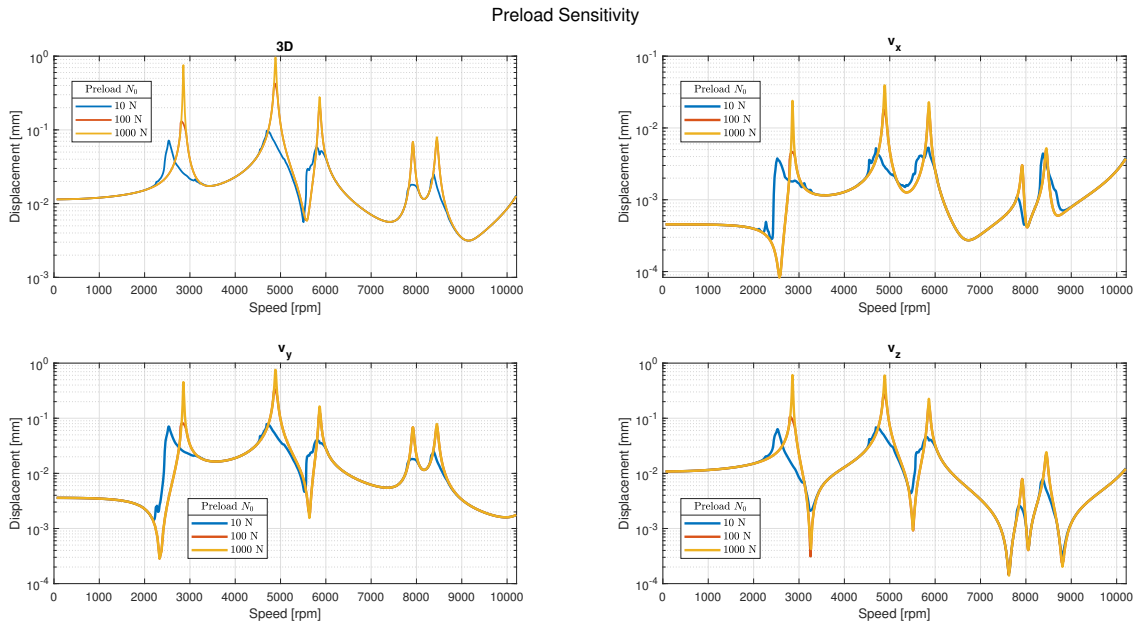


Figure 8.27: Preload Analysis

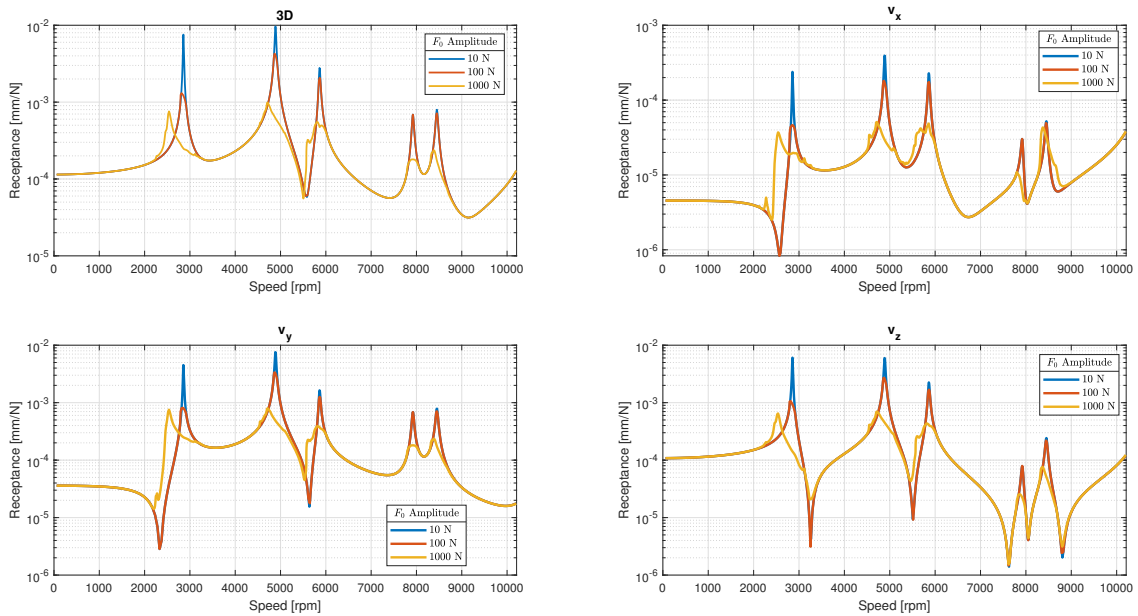


Figure 8.28: Excitation Level ($N_0 = 100$ N)

of one order of magnitude is registered at the second peak between the force in the shroud direction and the other two cases.

In addition, the behaviour of the system when physical parameters are changed, such as contact stiffness and damping, was observed.

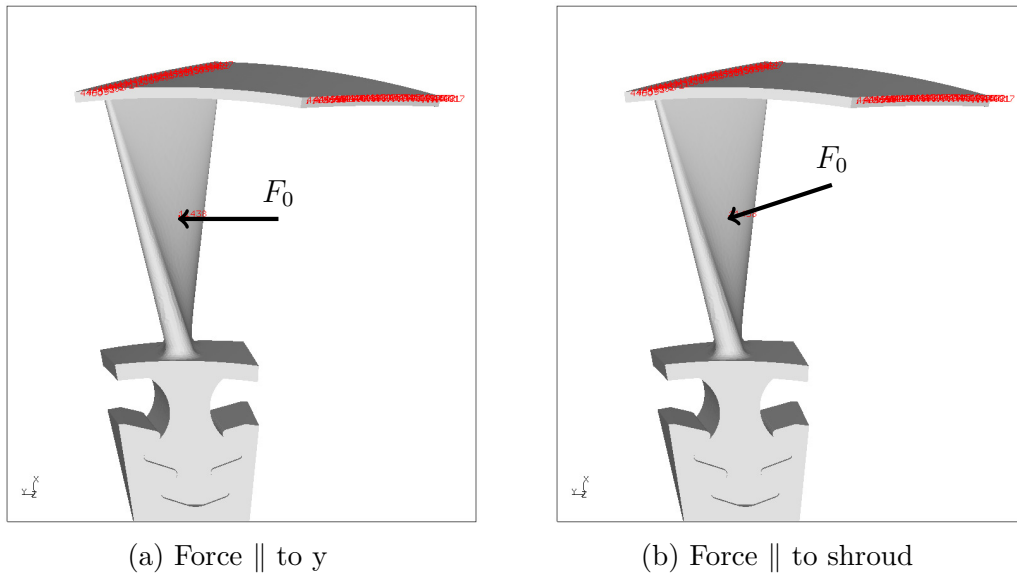


Figure 8.29: F_0 alternative directions

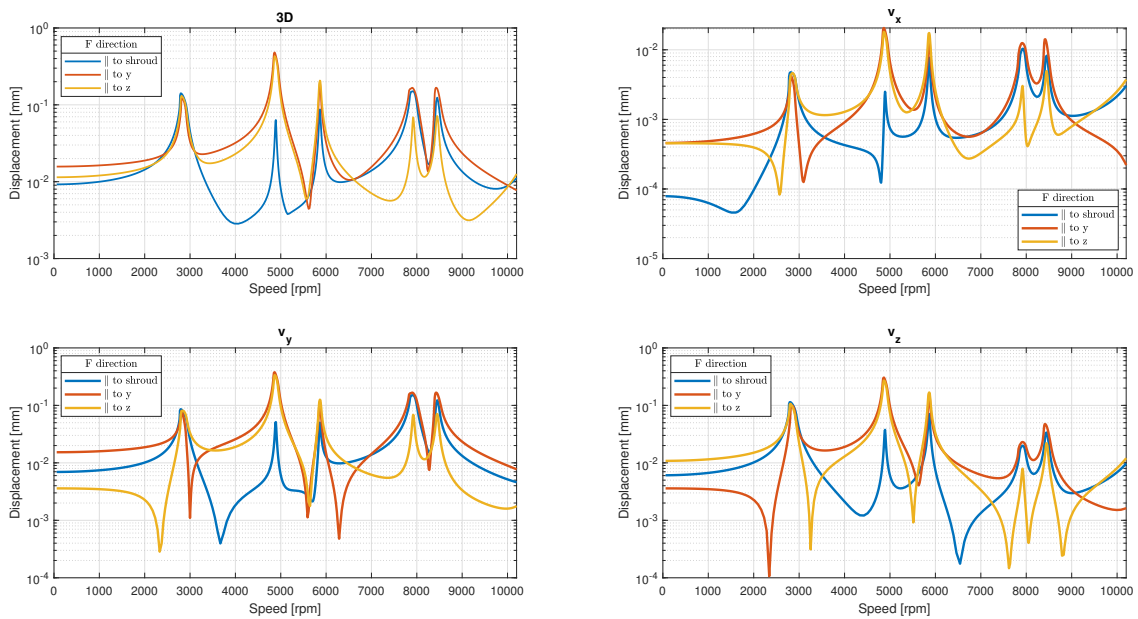


Figure 8.30: Excitation Direction ($N_0 = 100$ N)

First the stiffness parameters k_n and k_t were changed, albeit the equality $k_n = k_t$ has been retained: predictably, as stiffness increases, Figure 8.31 shows a shift of the peaks to the right as well as a lowering of the response level due to the stiffening of the assembly. However, there is also a greater nonlinearity of response due to the increased coupling between adjacent sectors.

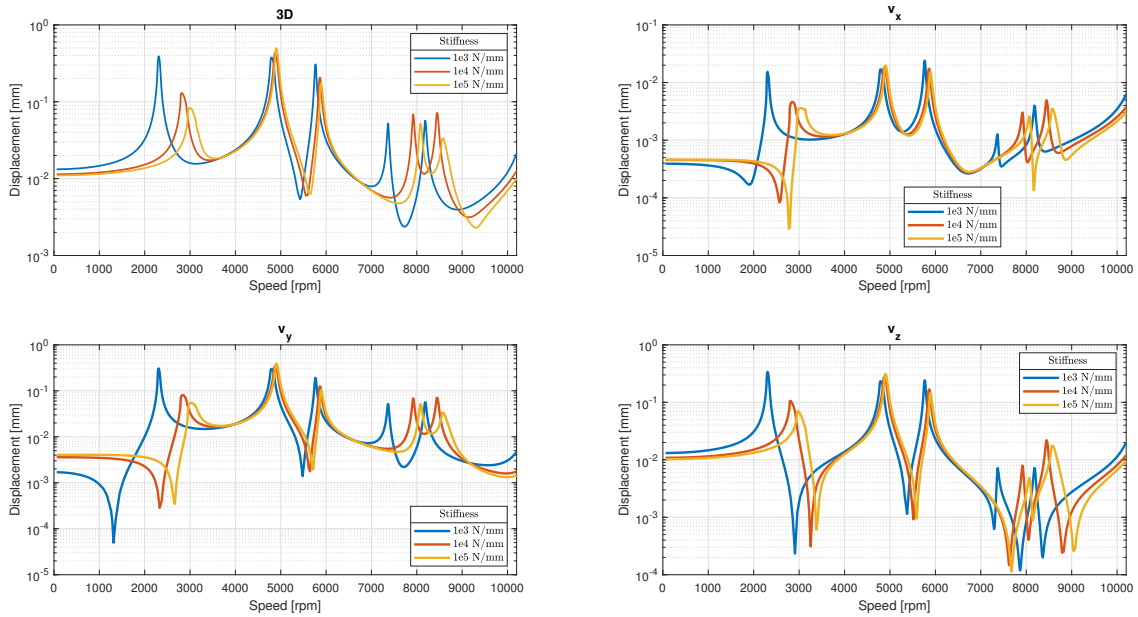


Figure 8.31: k_n and k_t Effect on the Response ($N_0 = 100$ N)

On the other hand, if one acts on the damping factor, as shown in the Figure 8.32, it can be observed that not only can a more damped system produce a considerable reduction in the level of response, with the fourth and fifth peaks almost disappearing, but also its nonlinear behaviour is profoundly altered.

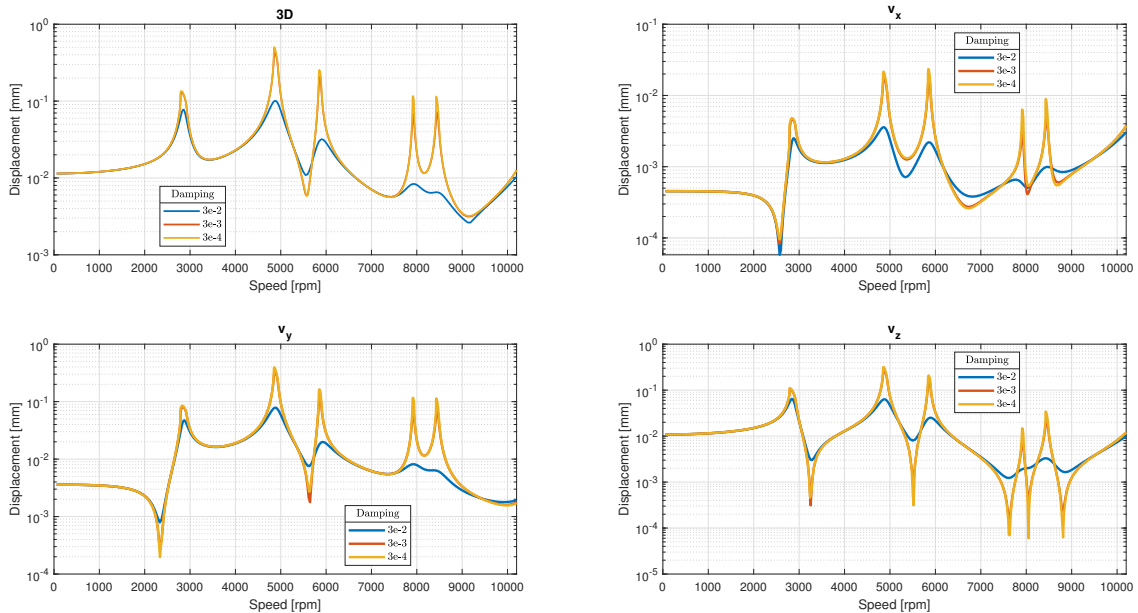


Figure 8.32: Damping Effect on the Response ($N_0 = 100$ N)

8.5.3 Comparison with NOVA

In addition to the forced response analysis with Imperial College in-house code FORSE, these were also carried out with NOVA, the code developed at Politecnico di Torino.

For the comparison two different preload levels ($N_0 = 10 \text{ N}$, $N_0 = 100 \text{ N}$) for three different engine orders ($EO = 23$, $EO = 45$, $EO = 52$) were selected.

However, before going into the details of the correlation between the two codes, it should be noted that there are some significant differences between the two models:

- the reduced order model was built in Ansys for NOVA using the **Craig-Bampton** technique instead of the hybrid method
- the reduced model used in FORSE *misses a local compliance contribution* since the static correction was neglected as its implementation led to a bug
- the local coordinate system defined for the nonlinear contact element is different as the two codes define the contact surface differently. However this should not affect the overall response but only the local contact forces.

Therefore, when studying the correlation between the two responses, the first two points in particular should be kept in mind as they have a non-negligible effect on the final response.

Figure 8.33 to 8.35 shows the forced responses obtained with FORSE (solid line) and NOVA (dotted line): the response is measured at the node in the centre of the blade where the force is also applied. The three curves represent the three degrees of freedom in the global system: blue for displacement along x , orange for displacement along y and yellow for displacement along z .

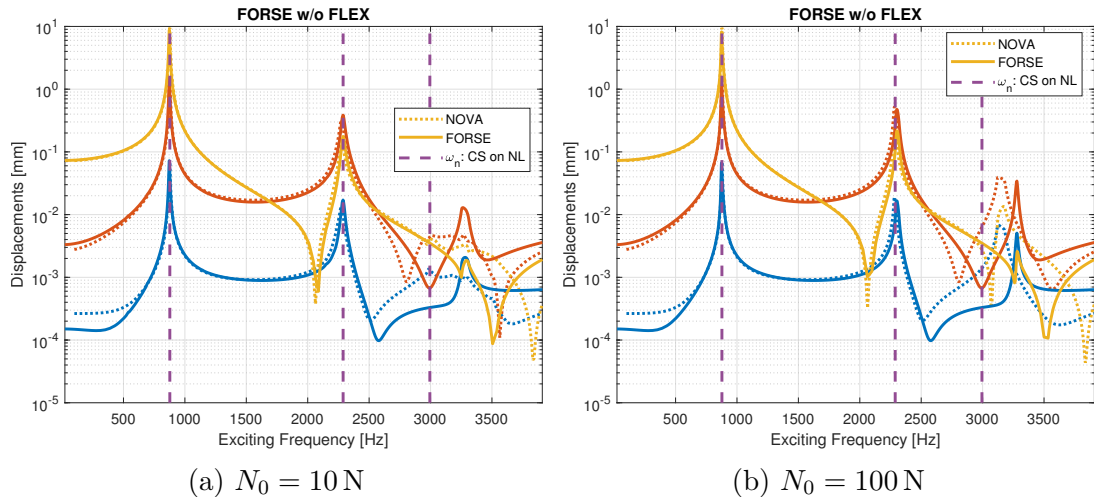


Figure 8.33: Comparison of Response ($EO = 23$)

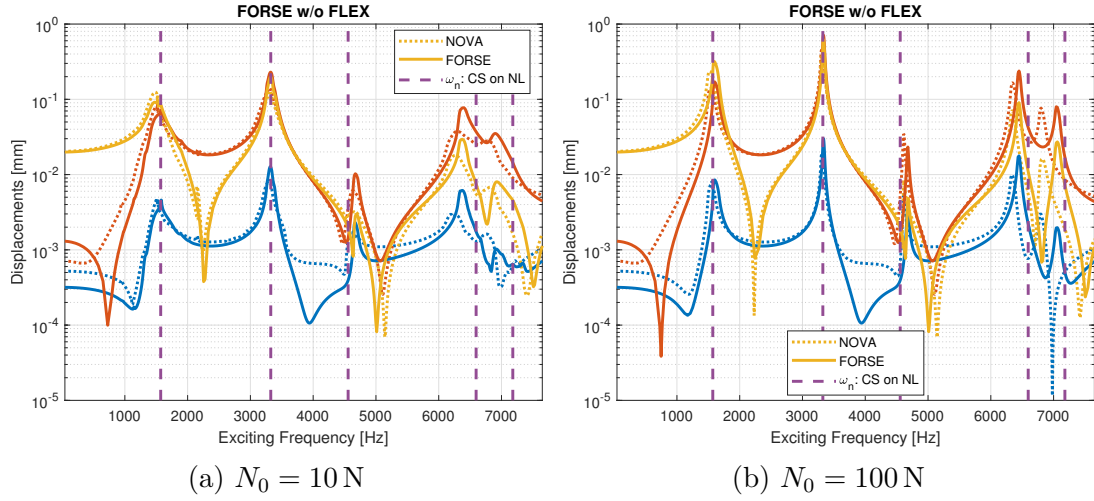


Figure 8.34: Comparison of Response ($EO = 45$)

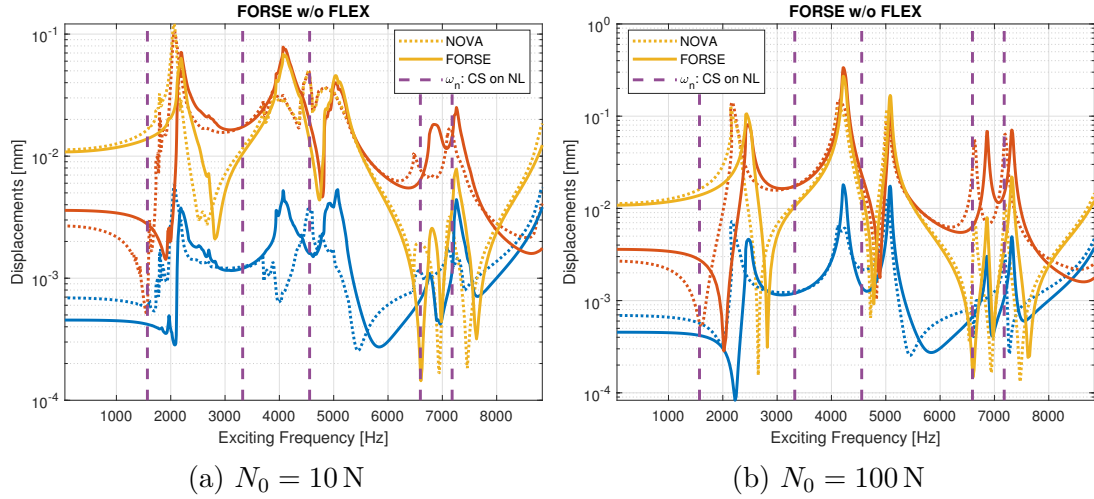


Figure 8.35: Comparison of Response ($EO = 52$)

Although not a one-to-one comparison, the correlation seem to give satisfactory results: at lower frequencies $EO = 23$ and 45 gives back both similar curves and peak location. However, at higher frequencies, in both cases it can be observed that the FORSE model acts more rigidly and the peak moves to the right compared to NOVA. A possible explanation could be that for higher modes the compliance contribution of the static correction has a greater effect; thus, as it is missing in FORSE, it leads to stiffer system.

In general it seems that the correlation is mode-dependent: in fact for $EO = 52$ one can notice especially for the x displacement a bad correlation when $N_0 = 10 \text{ N}$: the nonlinearity of the stiffer reduced model of FORSE seems less pronounced and it

is notable how the peaks lie at higher frequency compared to NOVA.

8.6 A Different Shroud Geometry

Ultimately, the effect of a change in shroud geometry was observed: its most protruding end was cut off and rotated to fit on the opposite side. Thus obtaining a more balanced partition of the fundamental sector, but without affecting the overall geometry of the assembly.

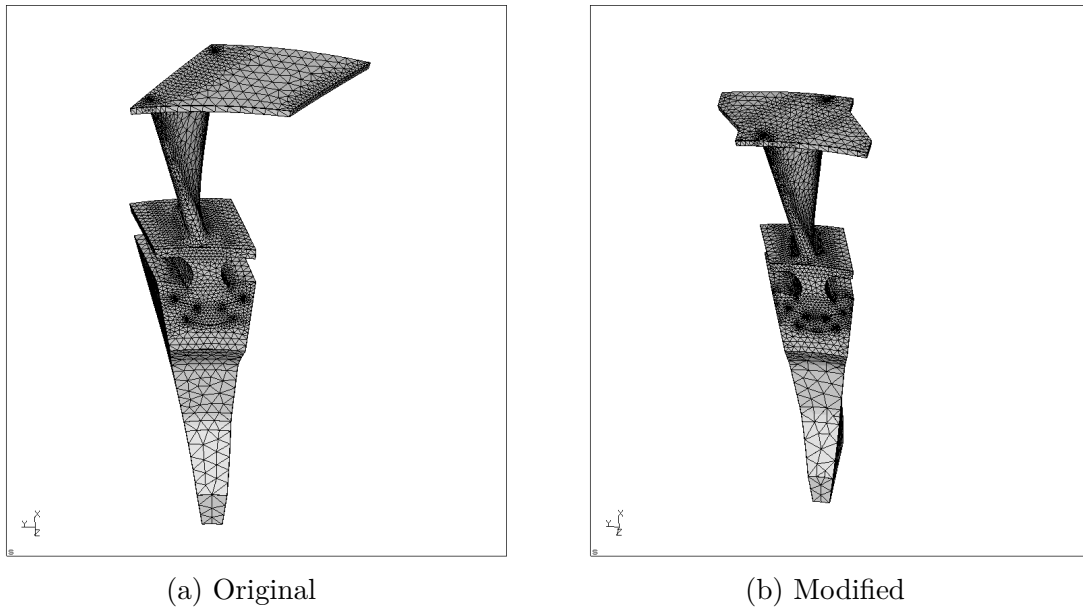


Figure 8.36: Geometry Comparison

The new geometry has then been meshed with the aim of generating a mesh of similar size to the previous one.

	Original	Modified
N° of Elements	74 470	69 860
N° of Nodes	118 725	112 824
N° of DOFs	356 175	338 472

Table 8.6: Mesh Comparison

For the finite element model, the same boundary conditions were imposed, i.e. two different configurations, cantilever and fixed, are used, and the same static and modal analyses were carried out.

Thus, the objective here is not only to compare the two forced responses but also the various intermediate stages of the verification process.

8.6.1 Modal Analysis

First, the results of the modal analysis, i.e. the natural frequencies of the system, were compared. In Figure 8.37 the comparison between the natural frequencies of the cantilever configuration are shown: the modified geometry is generally stiffer, the median of the increase is about 10%. The explanation can be found in the better weight distribution, as the shroud is not as unbalanced to one of the sides, leading to a stiffer assembly.

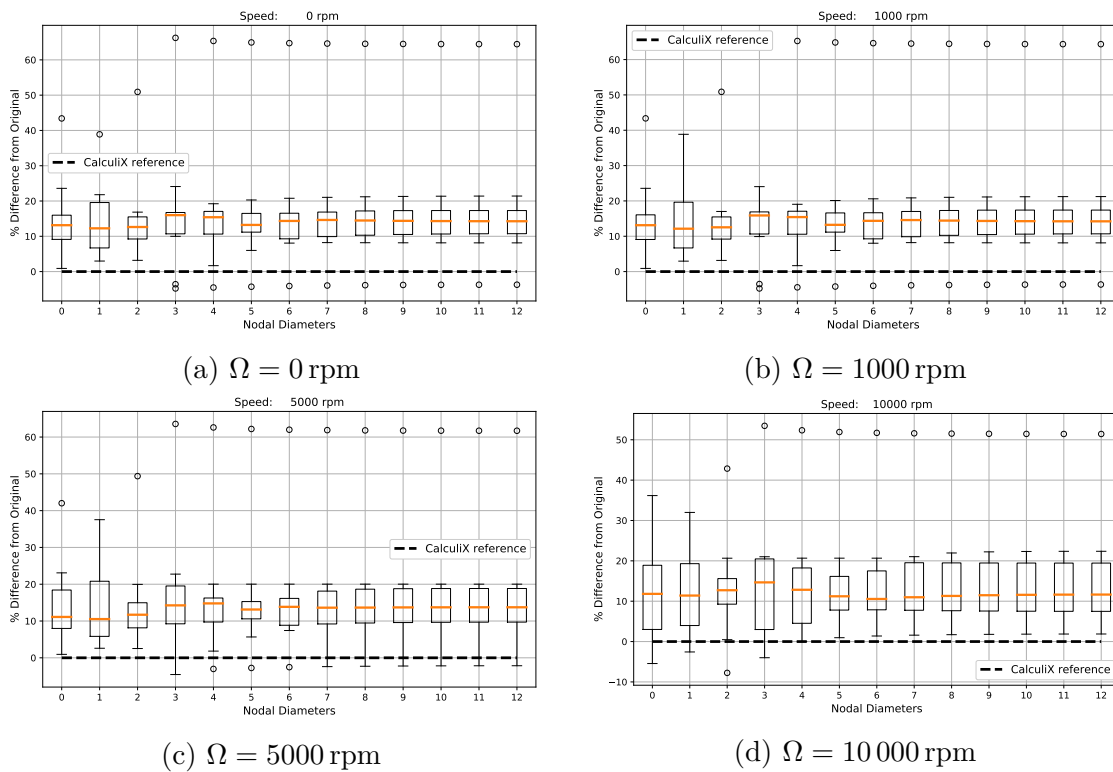


Figure 8.37: Cantilever Configuration: Natural Frequencies Comparison

However, when plotting the natural frequencies vs. nodal diameters, the mode family curves behaviour is quite similar between the two, albeit the modified geometry lead to higher values.

In contrast, the fixed configuration modal analysis returns a negligible difference in terms of natural frequencies, Figure 8.39 shows that the maximum registered difference is about 1.4%. The reason for this small variation lies in the boundary conditions, which in this case also interconnect the shroud and not only the disc, so as the overall assembly is the same no significant difference is found.

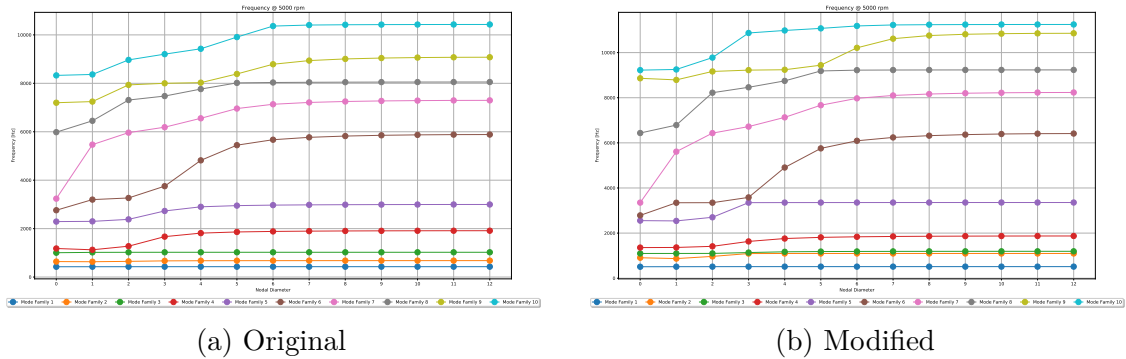


Figure 8.38: Cantilever Configuration: Natural Frequencies vs. ND

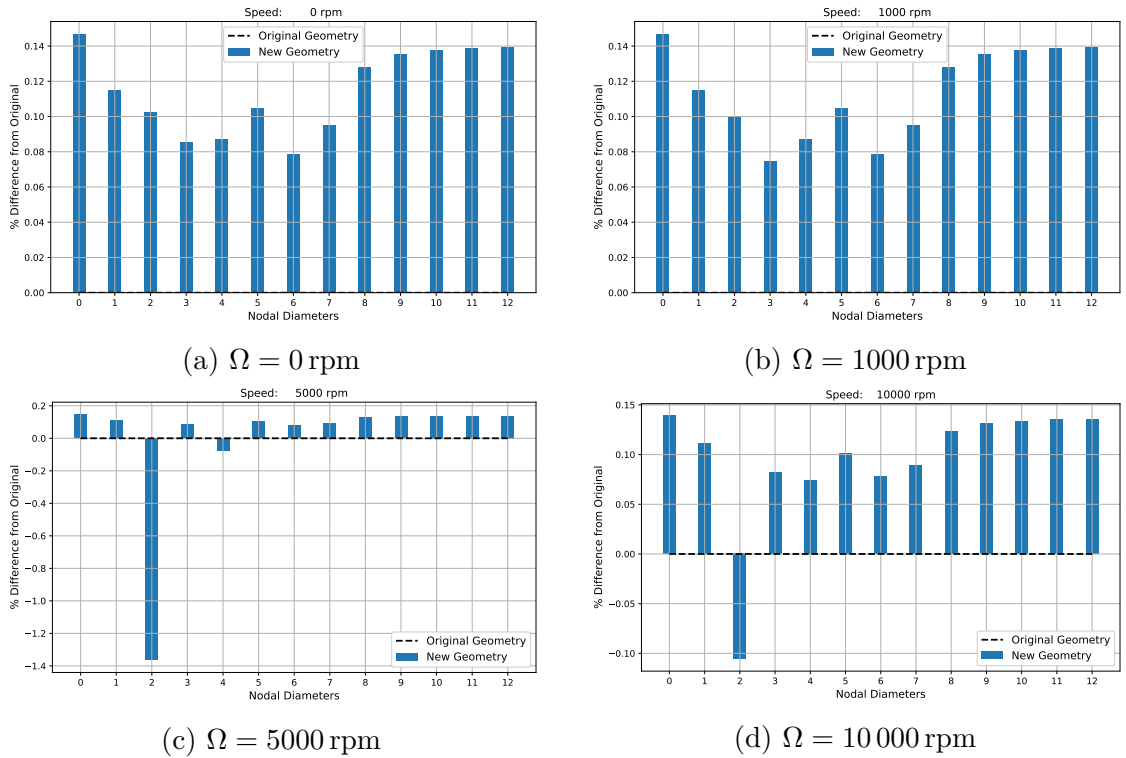


Figure 8.39: Fixed Configuration: Natural Frequencies Comparison

8.6.2 Forced Response

The first important step, leading to the forced response, is model order reduction: here, too, efforts have been made to minimise the differences between the two, see Table 8.7 for a breakdown of the differences.

However, given the “Z shape” of the new shroud, two models, see Figure 8.40 have been created: one containing only the contact elements, same ones used previously,

	Original	Modified
Technique	Hybrid	Hybrid
N° of NL nodes	55	77
N° of NL elements	27	32
N° of DOFs per node	3	3
N° of Modes retained	100	100

Table 8.7: MOR Comparison

and another one having gap element instead at the extremities.

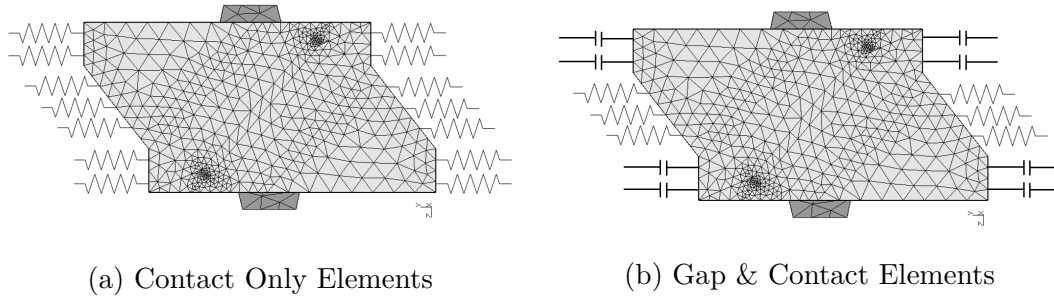


Figure 8.40: Modified shroud modelling

The gap element is designed to constrain displacement in the normal direction between two nodes: a linear force is produced when the prescribed gap between the two opens (in case of interference) or closes (in case of clearance).

For the forced-response setup, the same reference values of Table 8.4 were used except for the area, while the gap element properties are shown in Table 8.8.

Engine Order 52

Response to the 52nd engine order excitation, with $F_0 = 100$ N, is shown in Figure 8.42: it is evident that the mixed contact-gap configuration is more prone to nonlinear behaviour and that there are more peaks due to a greater contribution from the super-harmonics. However, similar to the reference case, it can be seen that for both, a lower preload not only introduces greater nonlinearities but also reduces the level of response.

Before comparing them to the reference geometry, a sensitivity study on the effects of the prescribed clearance was carried out. Figure 8.43 shows how moving from clearance to interference results in a stiffening of the system which gradually assumes a more linear behaviour. In terms of response, while the first peak seems to be highly dependent on the gap, for the others the sensitivity to gap variation is

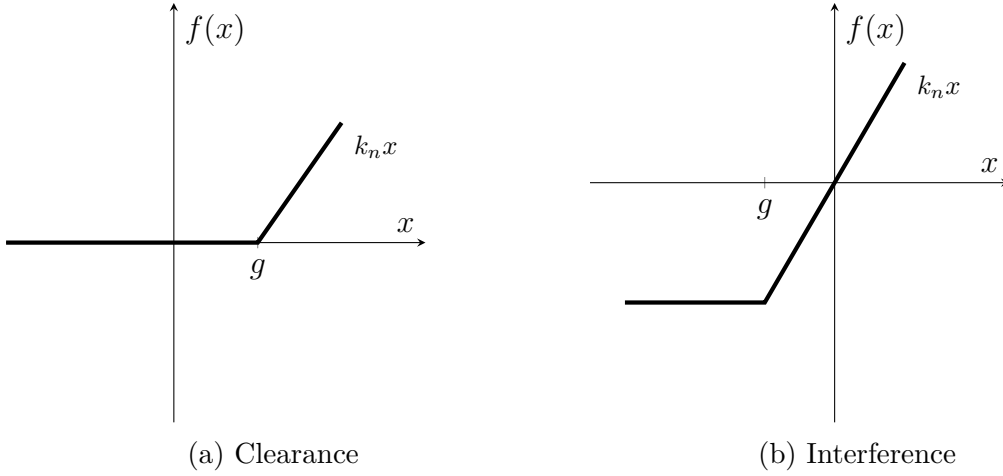


Figure 8.41: Gap Element Normal Force

Property		Element	
		Contact	Gap
k_n	[N/mm]	1×10^4	1×10^4
k_t	[N/mm]	1×10^4	-
Area	[mm ²]	2.227 58	1.408 84
μ	[-]	0.4	-
g	[mm]	-	1×10^{-3}

Table 8.8: FORSE Setup

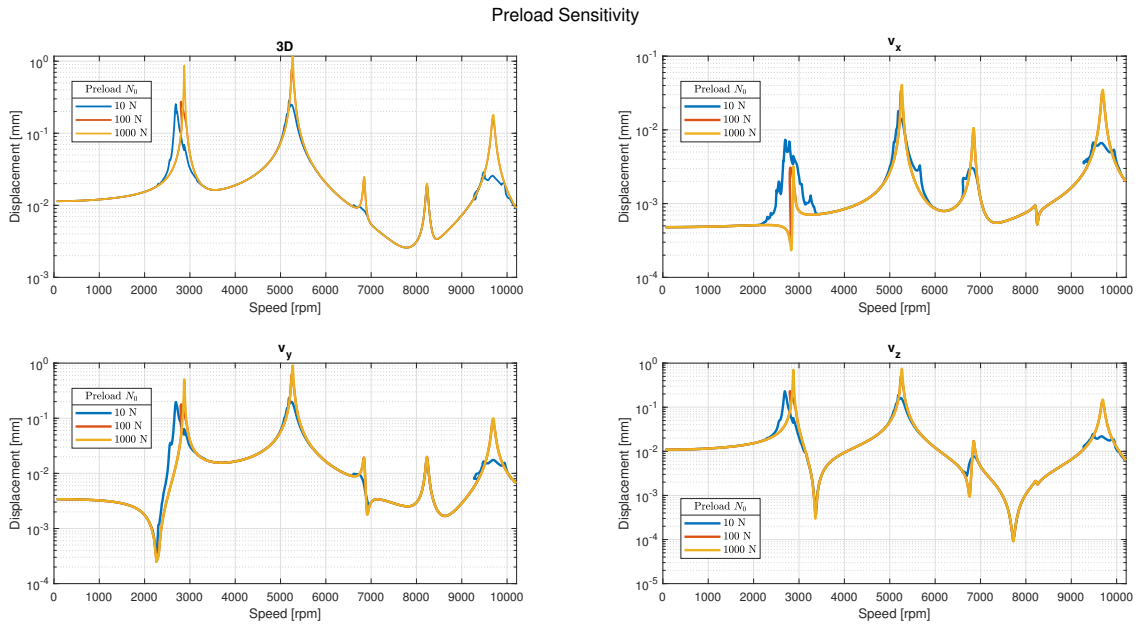
greatly reduced.

Moreover, it can be seen that by imposing an increasing interference, the response obtained approaches that of the configuration with only contact elements.

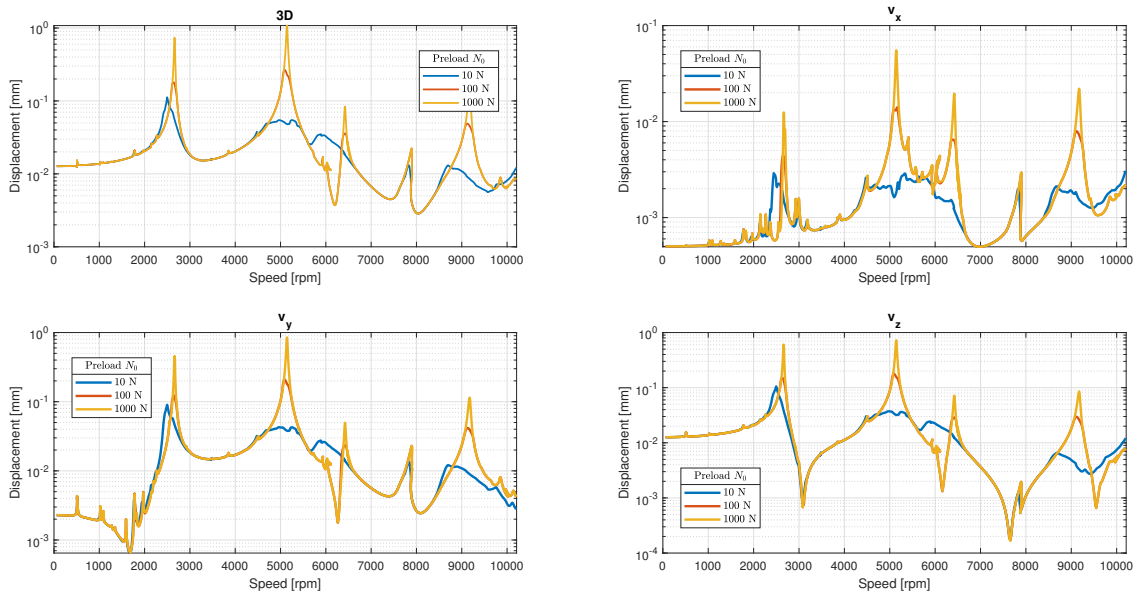
Finally, the comparison between the original and the modified shroud geometry, both configurations, is shown in Figure 8.44.

By first analysing the differences between the original geometry and the new one with only contact elements, it can be established that the latter results in a more rigid system and also in higher response levels. However, it is difficult to establish a rigorous pattern: the stiffening seems to vary according to the excited mode, for example for $N_0 = 100$ N the first peak is at the same frequency while for the third there is a difference of almost 1000 Hz and then for the fourth the deviation becomes smaller again. Finally, it should also be noted that the two geometries also produce different nonlinearity effects.

As for the reasons for this difference, in addition to the geometry it must be said that the arrangement of the master nodes used in the construction of the ROM has



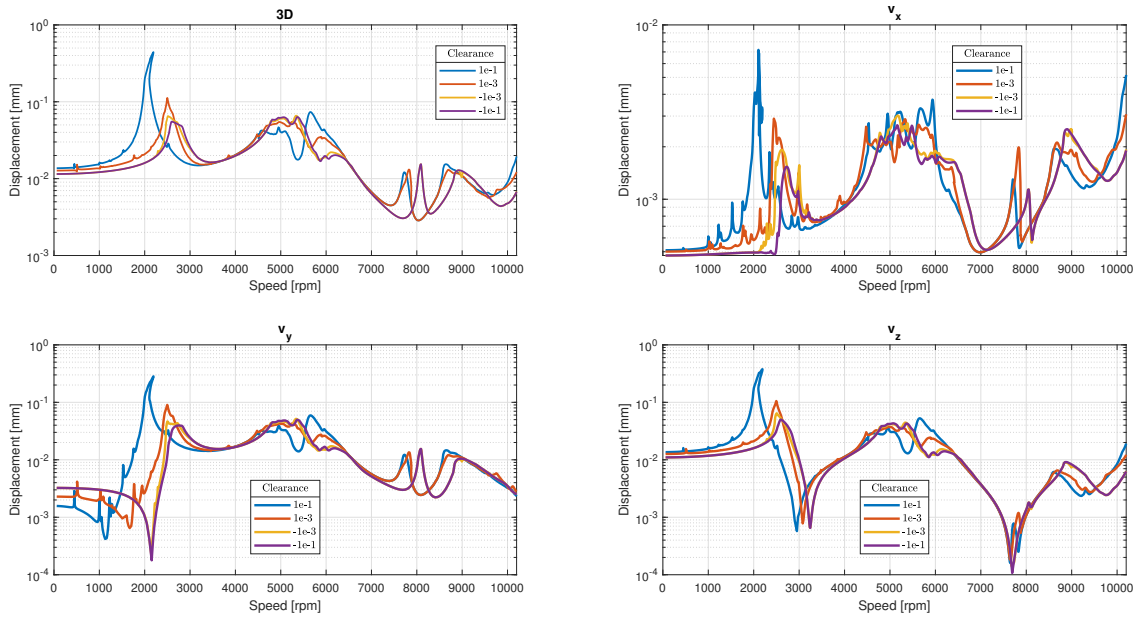
(a) Contact Only
Preload Sensitivity



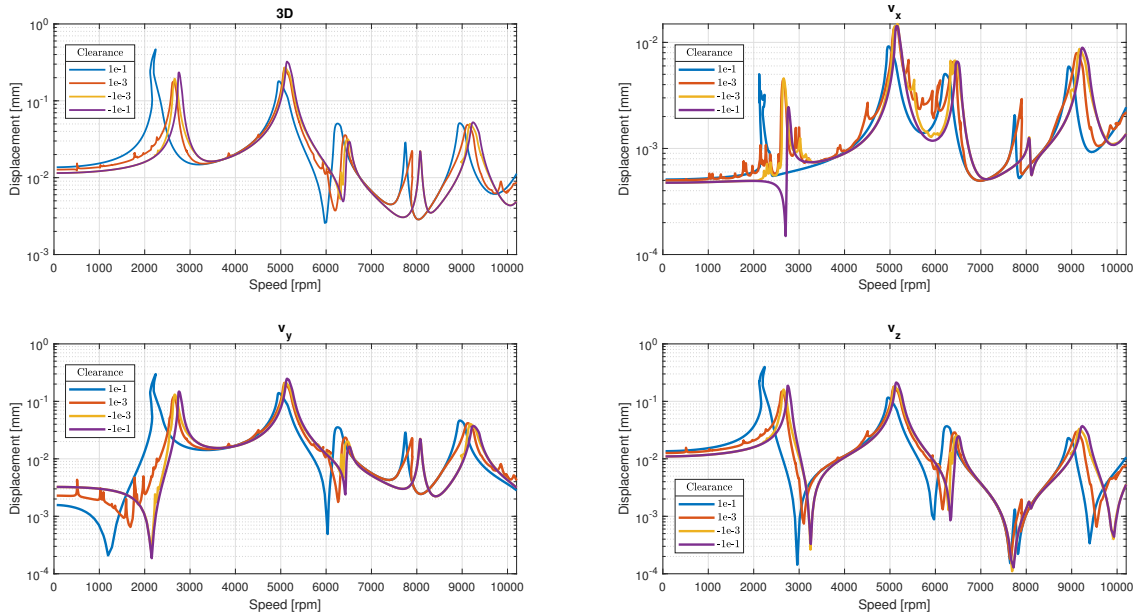
(b) Gap & Contact

Figure 8.42: Modified Shroud Forced Response for different preload levels

changed: they are no longer on a horizontal line in the middle of the shroud surface but scattered throughout it. Moreover, the number of nodes and therefore also of nonlinear elements used is different. It should also be mentioned that the strong differences found in modal analysis with open shroud may have a significant impact



(a) $N_0 = 10 \text{ N}$

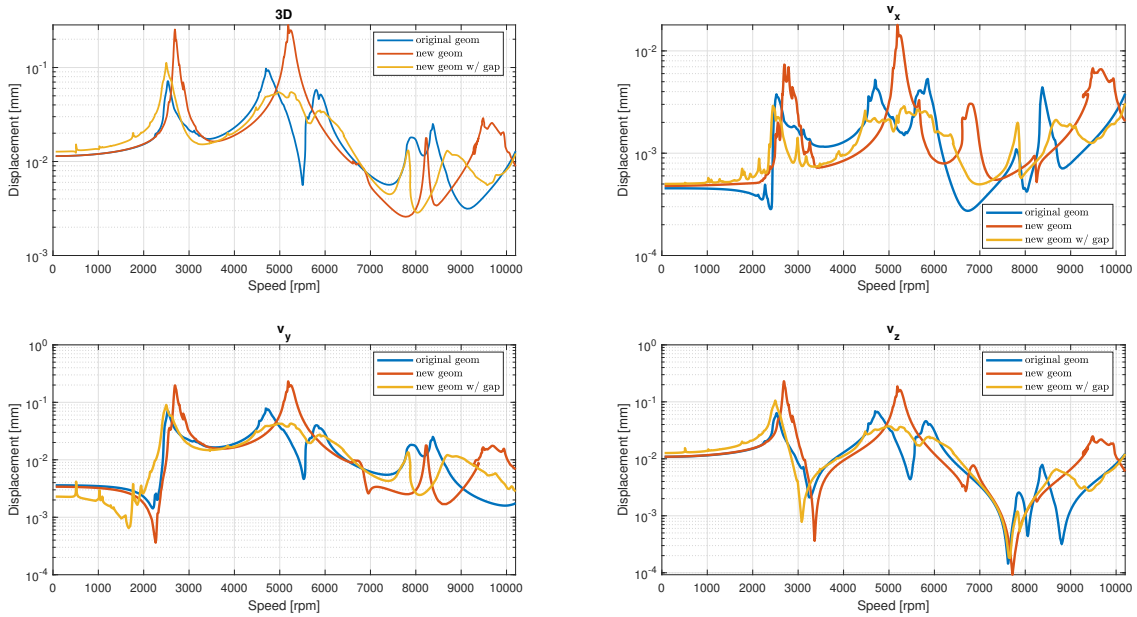


(b) $N_0 = 100 \text{ N}$

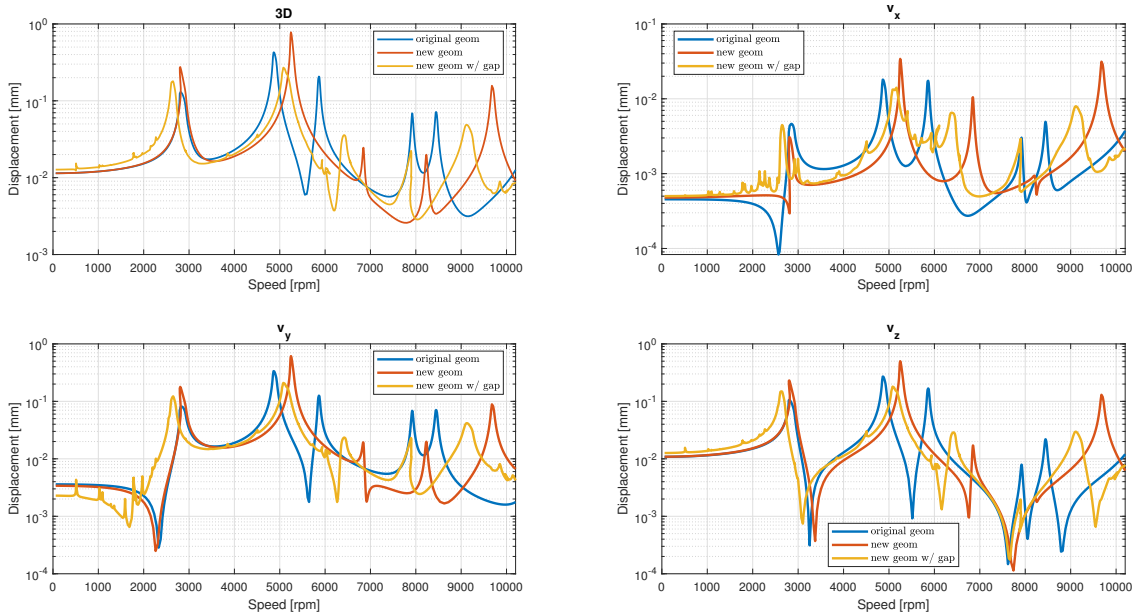
Figure 8.43: Clearance Effect on the Response

when building the reduced model, especially when the static correction is omitted.

Finally, what is the impact of the gap elements has to be analysed: the response obtained presents much more marked nonlinearities than the previous ones and in general the peaks seem to be in the middle between the response with the new



(a) $N_0 = 10\text{ N}$



(b) $N_0 = 100\text{ N}$

Figure 8.44: Forced Response Comparison of the different shroud discretizations

geometry and the original one, although once again it is difficult to draw general conclusions.

Chapter 9

Conclusion

In this last chapter, an attempt will be made to summarise what the project was and what means are available to the designer to carry out the analysis of a turbomachinery.

First of all, the efficiency with which it is possible to study the behaviour of an entire bladed disc should be emphasised: the assumptions of cyclic symmetry have made it possible to reduce the analysis time considerably, for example the creation of the reduced order model with Ansys using 6 cores took around 4 hours. For the forced response, harmonic balance method allows results to be obtained in just a few minutes if the number of harmonics required is not too high.

From this point of view, the tools under development not only allow checks to be carried out after the design has been completed, but also become a tool for the design itself in order to better optimise the final product: especially in the early stages where an extremely accurate result is not as important as it will be later on when doing the final validation of the prototype.

However, there are also limitations such as being able to use it to study only periodic vibrations, also there may be numerical difficulties for example in the simulation of an impact problem or the study of the coupled static-dynamic problem. Therefore these tools can not entirely replace physical tests, which instead are necessary for the validation of the tool itself. For the virtual simulation of the entire engine, however, we need to make progress: for example, the parallelisation of calculations on several nodes and not just on several cores, which Dr. SALLES' research team is working on.

The project has certainly demonstrated the potential of the tools available: it would certainly be more interesting to draw a parallel with experimental validations as a final check on the validity of the methods used.

It must be said that the bug on the reduced hybrid model in FORSE must be corrected, and it must also be said that in addition to the simulations carried out, the software also allows other simulations, as well as the use of a large library of elements. It would be interesting to investigate better how much the set of master

nodes affects the ROM and therefore the results, as well as to study more deeply the effect of the shroud geometry.

As far as the correlation with NOVA is concerned, it was not possible to make a one-to-one comparison and therefore the results can only be partially interpreted: however, they seem to be encouraging, further validating the goodness of the methodologies used.

Appendix A

CalculiX Input Files

A.1 Modal Analysis

```
*INCLUDE, INPUT=mesh.inp
**
*Material, NAME=Titanium
*Density
4.507E-09
*Elastic
1.16E+05, 0.34
**
*Solid section, Elset=Sector, Material=Titanium
**
*Surface, NAME=surf_left, TYPE=NODE
left
*Surface, NAME=surf_right, TYPE=NODE
right
*TIE,CYCLIC SYMMETRY,POSITION TOLERANCE=1.,NAME=tie_CS
surf_left, surf_right
*CYCLIC SYMMETRY MODEL, N=24, NGRAPH=1, TIE=tie_CS
0,0,0,0,0,1
**
*BOUNDARY
bot, 1, 3
**
** Static Loading
**
*Step, Nlgeom, Inc=100
*Static
1, 1, 1E-05, 1E+30
*Dload
Sector, CENTRIF, 274155.7, 0, 0, 0, 0, 0, 1
```

```

*Node file
U
*End step
**
** Modal Analysis
**
*Step,Perturbation
*Frequency
20
*SELECT CYCLIC SYMMETRY MODES, NMIN=0, NMAX=12
*Node file
U
*End step

```

A.2 Reduced Order Model

A.2.1 Modeshapes

```

*INCLUDE, INPUT=mesh_free.inp
**
*Material, NAME=Titanium
*Density
4.507E-09
*Elastic
1.16E+05, 0.34
**
*Solid section, Elset=Sector, Material=Titanium
**
*Surface, NAME=surf_left, TYPE=NODE
left
*Surface, NAME=surf_right, TYPE=NODE
right
*TIE,CYCLIC SYMMETRY,POSITION TOLERANCE=1.,NAME=tie_CS
surf_left, surf_right
*CYCLIC SYMMETRY MODEL, N=24, NGRAPH=1, TIE=tie_CS
0,0,0,0,0,1
**
*BOUNDARY
bot, 1, 3
**
** Static Loading
**
*Step, Nlgeom, Inc=100
*Static
1, 1, 1E-05, 1E+30

```

```

*Dload
Sector, CENTRIF, 274155.7, 0, 0, 0, 0, 0, 1
*End step
**
** Modal Analysis
**
*Step,Perturbation
*Frequency
200
*SELECT CYCLIC SYMMETRY MODES, NMIN=0, NMAX=12
*Node Print, NSET=NL
U
*End step

```

A.2.2 Static Correction

```

*INCLUDE, INPUT=mesh_free.inp
**
*Material, NAME=Titanium
*Density
4.507E-09
*Elastic
1.16E+05, 0.34
**
*Solid section, Elset=Sector, Material=Titanium
**
*Surface, NAME=surf_left, TYPE=NODE
left
*Surface, NAME=surf_right, TYPE=NODE
right
*TIE,CYCLIC SYMMETRY,POSITION TOLERANCE=1.,NAME=tie_CS
surf_left, surf_right
*CYCLIC SYMMETRY MODEL, N=24, NGRAPH=1, TIE=tie_CS
0,0,0,0,0,1
**
*BOUNDARY
bot, 1, 3
**
*Step, Nlgeom, Inc=100
*Static
1, 1, 1E-05, 1E+30
*Dload
Sector, CENTRIF, 274155.7, 0, 0, 0, 0, 0, 1
*End step

```

```
*Step,Perturbation
*Green
*CLOAD, OMEGA0 = 0
NL, 1, 1
*Node file
U
*Node print, Nset = NL
U
*End step
```

```
*Step,Perturbation
*Green
*CLOAD, OMEGA0 = 0
NL, 2, 1
*Node file
U
*Node print, Nset = NL
U
*End step
```

```
*Step,Perturbation
*Green
*CLOAD, OMEGA0 = 0
NL, 3, 1
*Node file
U
*Node print, Nset = NL
U
*End step
```

Appendix B

Ansys Input Files

B.1 Modal Analysis

```
finish
/CLEAR

! Parameters
E   = 1.16e5   ! [MPa]
Nu  = 0.34    ! [-]
rho = 4.507e-9 ! [ton/mm^3]
speed = 5e3*2*3.14/60 ! [rad/s]

/PREP7
! Assign Titanium Properties to mat #1
MP,ex,1,E
MP,nuxy,1,Nu
MP,dens,1,rho
MAT,1
! Mesh
/INPUT,'tetra','msh'
! Global BC
/INPUT,'bot_123','bou'
nlgeom,ON
cyclic, , , , 'FIXED'
! Centrifugal Loading
/SOLU
antype,0
OMEGA,0,0,speed,
rescontrol,define,last,last
solve
finish
! Modal Analysis
```

```

/SOLU
ANTYPE,0,RESTART,,,PERTURB
PERTURB,MODAL
solve,elform
MODOPT,SUBSP,20
MXPAND,20,,,YES
solve

```

B.2 Reduced Order Model

```

finish
/CLEAR
/FILNAME,CBCMS,2

! Parameters
E   = 1.16e5    ! [MPa]
Nu  = 0.34
rho = 4.507e-9 ! [ton/mm^3]
speed = 5e3*2*3.14/60 ! [rad/s]
Nsector = 24

/PREP7
! Assign Titanium Properties to mat #1
MP,ex,1,E
MP,nuxy,1,Nu
MP,dens,1,rho
mat,1

! Mesh
/INPUT,'tetra','msh'

allsel
csys,1

! define right shroud local coordinate system
cs,11,cart,52,870,51
! define left shroud local coordinate system
cs,12,cart,4,348,3

! rotate nodal coordinate of right shroud contact nodes
cmsel,s,nl
nselect,r,node,,44000,45000
csys,11
nrotat,all

```

```

! rotate nodal coordinate of left shroud contact nodes
csys,1
allsel
cmsel,s,nl
nset,r,node,,4400,4500
csys,12
nrotat,all
csys,1
allsel
finish

/PREP7

! Cyclic Symmetry Definition
/INPUT,'high_surface','nam'
/INPUT,'low_surface','nam'
cmgrp,cyclic,cyclic_m01l,cyclic_m01h
cyclic,Nsector,360/Nsector,1,cyclic,1,,
allsel,all

! Prestress w/ NLGEOM
NLGEOM,ON
/SOLU
ANTYPE,0
! Global BC
/INPUT,BoundaryCondition,'bou'
OMEGA,0,0,speed,
RESCONTROL,DEFINE,LAST,LAST
solve
finish

! Generation of SuperElements
/SOLU
ANTYPE,0,RESTART,,,PERTURB
PERTURB,SUBSTR
allsel,all
SOLVE,ELFORM
SEOPT,CB_matrices,2,1
CMSEL,s,NL,node
M,all,all
ALLSEL,ALL
CMSOPT,FIX,200,,,,,,,,,SUBS
solve
save
finish

```

```
! Print Matricess for each HI
*do,i,0,Nsector/2
  /aux2
  file,CB_matricesHI%i%,sub
  hbmatt,CB_stiffHI%i%,txt,,ascii,stiff,no,yes
  hbmatt,CB_massHI%i%,txt,,ascii,mass,no,yes
*enddo
finish
```

Bibliography

- [1] Malte Krack, Loic Salles, and Fabrice Thouverez. “Vibration Prediction of Bladed Disks Coupled by Friction Joints”. In: *Archives of Computational Methods in Engineering* 24.3 (2017), pp. 589–636. DOI: [10.1007/s11831-016-9183-2](https://doi.org/10.1007/s11831-016-9183-2). URL: <https://hal.archives-ouvertes.fr/hal-01825517>.
- [2] Stefano Zucca. *Teaching Slide for Rotor Dynamics*. Politecnico di Torino.
- [3] A. V. Srinivasan. “Flutter and Resonant Vibration Characteristics of Engine Blades”. In: *Journal of Engineering for Gas Turbines and Power* 119.4 (Oct. 1997), pp. 742–775. ISSN: 0742-4795. DOI: [10.1115/1.2817053](https://doi.org/10.1115/1.2817053). URL: <https://doi.org/10.1115/1.2817053>.
- [4] Alessandro Sommariva and Stefano Zucca. “A Comparison between Two Reduction Strategies for Shrouded Bladed Disks”. In: *Applied Sciences* 8.10 (2018), p. 1736.
- [5] Johann Gross et al. “Effect of creep on the nonlinear vibration characteristics of blades with interlocked shrouds”. In: *International Journal of Non-Linear Mechanics* 99 (2018), pp. 240–246. URL: <http://www.sciencedirect.com/science/article/pii/S0020746217303694>.
- [6] D. Ewins. “The effects of detuning upon the forced vibrations of bladed disks”. In: *Journal of Sound and Vibration* 9 (1969), pp. 65–79.
- [7] Giuseppe Battiato et al. “Reduced Order Modeling for Multistage Bladed Disks With Friction Contacts at the Flange Joint”. In: *Journal of Engineering for Gas Turbines and Power* 140.5 (Jan. 2018). DOI: [10.1115/1.4038348](https://doi.org/10.1115/1.4038348).
- [8] B. A. Cowles. “High cycle fatigue in aircraft gas turbines—an industry perspective”. In: *International Journal of Fracture* 80 (1996), pp. 147–163.
- [9] J. Szwedowicz. *High Cycle Fatigue*. Notes on Structural Design of Aircraft Engines. NATO OTAN. 2012. DOI: [10.14339/RTO-EN-AVT-207](https://doi.org/10.14339/RTO-EN-AVT-207).
- [10] E. Seinturier. “Forced Response Computation for Bladed Disks Industrial Practices and Advanced Methods”. In: 2007.

- [11] D.L. Thomas. “Dynamics of rotationally periodic structures”. In: *International Journal for Numerical Methods in Engineering* 14.1 (1979), pp. 81–102. DOI: [10.1002/nme.1620140107](https://doi.org/10.1002/nme.1620140107). URL: <https://hal.archives-ouvertes.fr/hal-01574169>.
- [12] Ronnie Bladh. “Efficient predictions of the vibratory response of mistuned bladed disks by reduced order modeling”. Theses. University of Michigan, July 2001. URL: <https://tel.archives-ouvertes.fr/tel-00358168>.
- [13] Brian J. Olson et al. “Circulant Matrices and Their Application to Vibration Analysis”. In: *Applied Mechanics Reviews* 66.4 (June 2014). 040803. ISSN: 0003-6900. DOI: [10.1115/1.4027722](https://doi.org/10.1115/1.4027722). URL: <https://doi.org/10.1115/1.4027722>.
- [14] S. Sreenivasamurthy and V. Ramamurti. “A parametric study of vibration of rotating pre-twisted and tapered low aspect ratio cantilever plates”. In: *Journal of Sound and Vibration* 76.3 (1981), pp. 311–328. ISSN: 0022-460X. DOI: [https://doi.org/10.1016/0022-460X\(81\)90515-0](https://doi.org/10.1016/0022-460X(81)90515-0). URL: <http://www.sciencedirect.com/science/article/pii/0022460X81905150>.
- [15] Nadja Wirth and Andre Oeckerath. “Analysis of flow-induced vibrations in turbomachinery by mapping of complex fluid pressures”. In: *The International Journal of Multiphysics* 9 (June 2015), pp. 195–208. DOI: [10.1260/1750-9548.9.2.195](https://doi.org/10.1260/1750-9548.9.2.195).
- [16] Marari P. Singh et al. “Safe Diagram - A Design And Reliability Tool For Turbine Blading”. In: 1988. URL: <http://hdl.handle.net/1969.1/163593>.
- [17] M. Singh. “History of Evolution, Progress and Application of Safe Diagram for Tuned and Mistuned Systems”. In: 2013.
- [18] C. Schwingshackl, Evgeny Petrov, and D. Ewins. “Effects of Contact Interface Parameters on Vibration of Turbine Bladed Disks With Underplatform Dampers”. In: *Journal of Engineering for Gas Turbines and Power* 134 (Mar. 2012), p. 032507. DOI: [10.1115/1.4004721](https://doi.org/10.1115/1.4004721).
- [19] Yekai Sun et al. “Nonlinear Vibrational Analysis for Integrally Bladed Disk Using Frictional Ring Damper”. In: *Journal of Physics: Conference Series* 1106 (2018), p. 012026. DOI: [10.1088/1742-6596/1106/1/012026](https://doi.org/10.1088/1742-6596/1106/1/012026). URL: <https://doi.org/10.1088/1742-6596/1106/1/012026>.
- [20] Mainak Mitra and Bogdan I. Epureanu. “Dynamic Modeling and Projection-Based Reduction Methods for Bladed Disks With Nonlinear Frictional and Intermittent Contact Interfaces”. In: *Applied Mechanics Reviews* 71.5 (Sept. 2019). 050803. ISSN: 0003-6900. DOI: [10.1115/1.4043083](https://doi.org/10.1115/1.4043083). URL: <https://doi.org/10.1115/1.4043083>.

-
- [21] Manuela Sander, Thomas Müller, and Carsten Stäcker. “Very high cycle fatigue behavior under constant and variable amplitude loading”. In: *Procedia Structural Integrity* 2 (Dec. 2016), pp. 34–41. DOI: [10.1016/j.prostr.2016.06.005](https://doi.org/10.1016/j.prostr.2016.06.005).
- [22] J.N. Reddy. *An Introduction to Nonlinear Finite Element Analysis*. OUP Oxford, 2004. ISBN: 9780198525295. URL: <https://books.google.it/books?id=gV2EN71IjwgC>.
- [23] G. Genta. *Dynamics of Rotating Systems*. Mechanical Engineering Series. Springer New York, 2007. ISBN: 9780387286877. URL: <https://books.google.it/books?id=ho31SIba5M0C>.
- [24] Antonio Gugliotta. *Elementi finiti*. Otto Editori, 2002.
- [25] Guido Dhondt and Klaus Wittig. *CalculiX Distribution*. URL: http://www.dhondt.de/ccx_2.17.pdf.
- [26] Cornelius Lanczos. *An iteration method for the solution of the eigenvalue problem of linear differential and integral operators*. United States Governm. Press Office Los Angeles, CA, 1950.
- [27] KJ Bathe. “Solution Methods for Large Generalized Eigenvalue Problems in Structural Engineering, Report UC SESM 71-20”. In: *Civil Engineering Department, UC Berkeley* (1971).
- [28] M. Krack. *Introduction to Harmonic Balance and application to nonlinear vibrations*. URL: <https://www.ila.uni-stuttgart.de/nlvib>.
- [29] Aurélien Grolet and Fabrice Thouverez. “On a new harmonic selection technique for harmonic balance method”. In: *Mechanical Systems and Signal Processing* 30 (2012), pp. 43–60. DOI: <https://doi.org/10.1016/j.ymsp.2012.01.024>.
- [30] Tianyuan Liu, Di Zhang, and Yonghui Xie. “A Nonlinear vibration analysis of forced response for a bladed-disk with dry friction dampers”. In: *Journal of Low Frequency Noise, Vibration and Active Control* 38 (Mar. 2019), p. 146134841983475. DOI: [10.1177/1461348419834759](https://doi.org/10.1177/1461348419834759).
- [31] Loïc Peletan et al. “Quasi-periodic harmonic balance method for rubbing self-induced vibrations in rotor-stator dynamics”. In: *Nonlinear Dynamics* 78 (July 2014), pp. 2501–2515. DOI: [10.1007/s11071-014-1606-8](https://doi.org/10.1007/s11071-014-1606-8).
- [32] E. P. Petrov. “A High-Accuracy Model Reduction for Analysis of Nonlinear Vibrations in Structures With Contact Interfaces”. In: *Journal of Engineering for Gas Turbines and Power* 133.10 (May 2011). ISSN: 0742-4795. DOI: [10.1115/1.4002810](https://doi.org/10.1115/1.4002810). URL: <https://doi.org/10.1115/1.4002810>.
- [33] Peter Avitabile. *Model Reduction Techniques*. University of Massachusetts Lowell. URL: http://faculty.uml.edu/pavitabile/22.515/model_reduction_061904.pdf.

- [34] Tom Irvine. *Craig-Bampton Method for a two Component System*. May 2003. URL: http://www.vibrationdata.com/tutorials2/CB_two_component.pdf.
- [35] J. T. Young. “Primer on the Craig-Bampton method”. In: (Oct. 2000).
- [36] Ronnie Bladh, Matthew Castanier, and Christophe Pierre. “Component-Mode-Based Reduced Order Modeling Techniques for Mistuned Bladed Disks—Part I: Theoretical Models”. In: *Journal of Engineering for Gas Turbines and Power-transactions of The Asme - J ENG GAS TURB POWER-T ASME* 123 (Jan. 2001). DOI: [10.1115/1.1338947](https://doi.org/10.1115/1.1338947).
- [37] Mehrdad Pourkiaee and Stefano Zucca. “A Reduced Order Model for Nonlinear Dynamics of Mistuned Bladed Disks With Shroud Friction Contacts”. In: *Journal of Engineering for Gas Turbines and Power* 141 (Oct. 2018). DOI: [10.1115/1.4041653](https://doi.org/10.1115/1.4041653).
- [38] Alok Sinha. *Vibration of Nearly Periodic Structures and Mistuned Bladed Rotors*. Cambridge University Press, 2017. DOI: [10.1017/9781316986806](https://doi.org/10.1017/9781316986806).
- [39] Evgeny Petrov. “A Method for Use of Cyclic Symmetry Properties in Analysis of Nonlinear Multiharmonic Vibrations of Bladed Disks”. In: *Journal of Turbomachinery* 126 (Jan. 2004), pp. 175–183. DOI: [10.1115/1.1644558](https://doi.org/10.1115/1.1644558).
- [40] Md Afzal, I. Lopez Arteaga, and L. Kari. “An analytical calculation of the Jacobian matrix for 3D friction contact model applied to turbine blade shroud contact”. In: *Computers & Structures* 177 (Aug. 2016), pp. 204–217. DOI: [10.1016/j.compstruc.2016.08.014](https://doi.org/10.1016/j.compstruc.2016.08.014).
- [41] C. Siewert et al. “Multiharmonic Forced Response Analysis of a Turbine Blading Coupled by Nonlinear Contact Forces”. In: *Journal of Engineering for Gas Turbines and Power-transactions of The Asme* 132 (2010).
- [42] Evgeny Petrov. “Analytical formulation of friction interface elements for analysis of nonlinear multi-harmonic vibrations of bladed disks”. In: *Journal of Turbomachinery* 125 (Feb. 2003), pp. 364–371.
- [43] A Cardona, A Lerusse, and M Geradin. “Fast Fourier nonlinear vibration analysis”. In: *Computational Mechanics* 22.2 (1998), pp. 128–142.
- [44] Lukas Woiwode et al. “Comparison of two algorithms for Harmonic Balance and path continuation”. In: *Mechanical Systems and Signal Processing* 136 (2020), p. 106503.
- [45] Malte Krack and Johann Gross. “Harmonic Balance for Nonlinear Vibration Problems”. In: ().
- [46] M. Pástor, Michal Binda, and Tomáš Harčarik. “Modal Assurance Criterion”. In: *Procedia Engineering* 48 (Dec. 2012), pp. 543–548. DOI: [10.1016/j.proeng.2012.09.551](https://doi.org/10.1016/j.proeng.2012.09.551).

- [47] Teresa Maria Berruti et al. “Friction Damping of Interlocked Vane Segments: Experimental Results”. In: *Journal of Engineering for Gas Turbines and Power-transactions of The Asme - J ENG GAS TURB POWER-T ASME* 124 (Oct. 2002). DOI: [10.1115/1.1494097](https://doi.org/10.1115/1.1494097).
- [48] CW Schwingshackl, EP Petrov, and DJ Ewins. “Measured and estimated friction interface parameters in a nonlinear dynamic analysis”. In: *Mechanical Systems and Signal Processing* 28 (2012), pp. 574–584.
- [49] Md Afzal, Ines Lopez Arteaga, and Leif Kari. “Numerical analysis of multiple friction contacts in bladed disks”. In: *International Journal of Mechanical Sciences* 137 (Mar. 2018). DOI: [10.1016/j.ijmecsci.2018.01.016](https://doi.org/10.1016/j.ijmecsci.2018.01.016).
- [50] Luca Pesaresi et al. “Modelling the nonlinear behaviour of an underplatform damper test rig for turbine applications”. In: *Mechanical Systems and Signal Processing* 85 (2017), pp. 662–679. DOI: [10.1016/j.ymsp.2016.09.007](https://doi.org/10.1016/j.ymsp.2016.09.007). URL: <https://hal.archives-ouvertes.fr/hal-01545328>.
- [51] Josef Voldrich et al. “Use of Cyclic Symmetry Properties in Vibration Analysis of Bladed Disks with Friction Contacts between Blades”. In: *Procedia Engineering* 96 (Dec. 2014). DOI: [10.1016/j.proeng.2014.12.122](https://doi.org/10.1016/j.proeng.2014.12.122).
- [52] G. Jacquet-Richardet, G. G. Ferraris, and P. Rieutord. “Frequencies and Modes of Rotating Flexible Bladed Disc-Shaft Assemblies: a Global Cyclic Symmetry Approach”. In: *Journal of Sound and Vibration* 191.5 (1996), pp. 901–915. ISSN: 0022-460X. DOI: <https://doi.org/10.1006/jsvi.1996.0162>. URL: <http://www.sciencedirect.com/science/article/pii/S0022460X96901625>.
- [53] W. Sestro. *Dynamical Contact Problems with Friction: Models, Methods, Experiments and Applications*. Lecture Notes in Applied and Computational Mechanics. Springer Berlin Heidelberg, 2013. ISBN: 9783540468714. URL: <https://books.google.it/books?id=m3LqCAAQBAJ>.
- [54] Colas Joannin, Fabrice Thouverez, and Benjamin Chouvion. “Reduced-order modelling using nonlinear modes and triple nonlinear modal synthesis”. In: *Computers & Structures* 203 (May 2018). DOI: [10.1016/j.compstruc.2018.05.005](https://doi.org/10.1016/j.compstruc.2018.05.005).
- [55] F Mashayekhi, AS Nobari, and S Zucca. “Hybrid reduction of mistuned bladed disks for nonlinear forced response analysis with dry friction”. In: *International Journal of Non-Linear Mechanics* 116 (2019), pp. 73–84.
- [56] Chiara Gastaldi, Alfredo Fantetti, and Teresa M Berruti. “Forced response prediction of turbine blades with flexible dampers: The impact of engineering modelling choices”. In: *Applied Sciences* 8.1 (2018), p. 34.

BIBLIOGRAPHY

- [57] *Non-Linear Dynamics of Steam Turbine Blades With Shroud: Numerical Analysis and Experiments*. Vol. Volume 6: Oil and Gas Applications; Concentrating Solar Power Plants; Steam Turbines; Wind Energy. Turbo Expo: Power for Land, Sea, and Air. June 2012, pp. 665–674. DOI: [10.1115/GT2012-69692](https://doi.org/10.1115/GT2012-69692). URL: <https://doi.org/10.1115/GT2012-69692>.
- [58] B. D. Yang, J. J. Chen, and C. H. Menq. “Prediction of Resonant Response of Shrouded Blades With Three-Dimensional Shroud Constraint”. In: *Journal of Engineering for Gas Turbines and Power* 121.3 (July 1999), pp. 523–529. ISSN: 0742-4795. DOI: [10.1115/1.2818504](https://doi.org/10.1115/1.2818504). URL: <https://doi.org/10.1115/1.2818504>.